Fabrication and Buckling of Thin Spherical Shells Containing Precise Geometric Imperfections

by

Anna Lee

B.S., Seoul National University (2011)
M.S., Seoul National University (2013)

Submitted to the Department of Mechanical Engineering
in partial fulfillment of the requirements for the degree of

Doctor of Philosophy in Mechanical Engineering

at the

MASSACHUSETTS INSTITUTE OF TECHNOLOGY

February 2018

Author .....
Department of Mechanical Engineering
December 18, 2017

Certified by .....
Pedro M. Reis
Visiting Associate Professor of Civil and Environmental Engineering (MIT) and Professor of Mechanical Engineering (École Polytechnique Fédérale de Lausanne, Switzerland)
Thesis Supervisor

Accepted by .....
Rohan Abeyaratne
Quentin Berg Professor of Mechanics
Chairman, Department Committee on Graduate Theses

Fabrication and Buckling of Thin Spherical Shells Containing Precise Geometric Imperfections

by

Anna Lee

Submitted to the Department of Mechanical Engineering
on December 18, 2017, in partial fulfillment of the
requirements for the degree of
Doctor of Philosophy in Mechanical Engineering

Abstract

We revisit the classic problem of buckling of thin spherical shells under uniform pressure and explore the effect that geometric imperfections can have on their buckling behavior. Since the 1960s, numerous theoretical and computational studies have addressed the imperfection sensitivity of buckling of thin elastic shells. However, there is a lack of precise experiments to corroborate these predictions, especially for spherical shells, which is the central topic of this thesis.

First, we develop a novel fabrication technique to produce thin hemispherical elastic shells by the coating of spherical molds with a polymer solution. Upon curing the thin liquid film yields the elastic structure of nearly constant thickness. We experimentally investigate the drainage dynamics, the final thickness, and its uniformity. Our results are directly compared with theoretical and numerical analyses. Secondly, we study the buckling of spherical shells that contain a precisely engineered geometric imperfection. Our shell fabrication technique allows us to introduce a single dimple-like defect with controllable geometric properties. We systematically vary the amplitude and width of the defect, and then we present a quantitative relationship between the critical buckling pressure and the defect geometry. Our results can be predicted by both the finite element method and numerical simulations of a reduced shell theory model. Finally, we fabricate hemispherical bilayer shells containing a defect. To do so, we coat two different polymer solutions, layer by layer, onto the hemispherical molds containing a defect. We find that the bilayer shell can self-repair or self-aggravate the geometric imperfections due to residual swelling. Hence, the critical buckling pressure can be increased or decreased over time depending on the order of coating of each polymer layer. The fabrication technique and experimental results presented in this thesis open exciting new avenues in the study of the buckling of spherical shells, and we hope that it will instigate a resurgence of interest in this classic but important field of mechanics.

Thesis Supervisor: Pedro M. Reis
Title: Visiting Associate Professor of Civil and Environmental Engineering (MIT) and Professor of Mechanical Engineering (École Polytechnique Fédérale de Lausanne, Switzerland)

Acknowledgments

Firstly, I would like to express my gratitude to my advisor Pedro for the continuous support of my Ph.D. study, for his valuable advises, motivations, encouragements, and immense knowledge. I could not have imagined having a better advisor for my Ph.D. study.

Besides my advisor, I would like to thank the rest of my thesis committee: Prof. Rohan Abeyaratne (MIT), Prof. David Parks (MIT), and Prof. John W. Hutchinson (Harvard University), for their insightful comments and for all their help getting me to complete this work.

I am also grateful to everyone whom I collaborated and EGS.Lab members. In particular, big thanks to Joel, Francisco, and Pierre-Thomas. Working with you was such a pleasure. I also thank Gioele Balestra and François Gallaire both in EPFL and Douglas Holmes in Boston University. Thanks, Matteo and Dong whom I will keep collaborating with, at FLEXLAB in EPFL, where I will move.

I would like to thank my Korean friends in MIT and Harvard University for their counsel, humor and friendship through the years. There are too many people to list by name here, but I appreciate you all!

Finally and most importantly, I would like to thank my family, especially to my parents for supporting me spiritually throughout my Ph.D. study and all my life, and to my husband Jonghyun for his unwavering support and love.

Thank you very much, everyone!

This work was supported by the National Science Foundation (CAREER CMMI-1351449) and Kwanjeong Educational Foundation.

Prior publications

Some of the findings presented in this thesis were published in these journal articles: (Lee et al., 2016a,b; López Jiménez et al., 2017)

Contents

1 Introduction **13**

1.1 Spherical shells and their applications 14

1.2 Buckling of spherical shells 17

1.3 Experimental investigations on the imperfection sensitivity of shell buckling 20

1.4 Experimental to fabrication of spherical shells 23

1.5 Liquid film coating to produce thin structures 25

1.6 Outline of the thesis 28

2 Fabrication of thin spherical shells **31**

2.1 Motivation and literature review 32

2.2 Fabrication method and the resulting thickness of thin shells 34

2.2.1 Experiments to fabricate shells with a variety of materials and geometrical properties 34

2.2.2 Physical ingredients that determine the thickness of the fabricated shells 36

2.3 Time-varying viscosity of polymer solutions 37

2.4 Free surface velocity profiles 39

2.5 Theoretical model with time-varying viscosity 43

2.5.1 Lubrication equation for a liquid film draining on a spherical surface 43

2.5.2 Including the effects of curing into the flow solution 44

2.6 Profiles of the liquid film and final shell thickness 46

2.6.1 Nonlinear drainage flow solution 46
2.6.2 Shear thinning effects 48
2.6.3 Estimation of the shear rate 51
2.7 Other factors that affect the shell thickness and its uniformity 53
2.7.1 Surface tension effects 53
2.7.2 Instabilities of the fluid interface 53
2.8 Robustness and insensitivity of the final shell thickness to the initial conditions 55
2.9 Tuning the final thickness 58
2.10 Summary and outlook 61

3 Defect-controlled buckling of pressurized spherical elastic shells 63
3.1 Motivation and literature review 64
3.2 Fabrication and experimental measurement of the buckling load of imperfect shells 65
3.2.1 Fabrication method to produce precisely imperfect thin elastic shells 65
3.2.2 Shape of the 'dimple-like' defect 68
3.2.3 Measuring the critical buckling pressure of the shells 70
3.2.4 Experimental procedure and range of parameters 71
3.3 Finite Element Simulations to characterize the imperfect shells 71
3.3.1 FEM results for the profile of the deformed molds 72
3.3.2 FEM results for the imperfection sensitivity 73
3.4 Comparison between experiments and FEM 74
3.5 Formulation of the shell theory 77
3.6 Axisymmetric deformations of clamped hemispheres containing axisymmetric imperfections: a set of nonlinear ODEs 81
3.7 Comparison between ODE and FEM results 83
3.8 Parametric exploration of the knockdown factor as a function of the imperfection geometry 86

3.8.1 Characterization of the imperfect shell by a single geometric parameter . . . 86
3.8.2 Buckling plateau for large amplitude defects . . . 89
3.9 Summary and outlook . . . 91

4 Buckling of hemispherical bilayer shells with residual swelling 93
4.1 Motivation and literature review . . . 94
4.2 Characterization of VPS bilayer structures . . . 99
4.3 Experimental methods . . . 105
4.3.1 Fabrication of hemispherical bilayer shells . . . 106
4.3.2 Measuring the critical buckling pressure of the bilayer shells . . . 109
4.4 Time dependence of the knockdown factor of the bilayer shells . . . 110
4.5 Characterization of the geometry of bilayer shells due to residual swelling 115
4.6 Spatial variation of the shell thickness . . . 116
4.7 FEM results for buckling of bilayer shells . . . 119
4.7.1 Normalization with effective thickness and modulus . . . 119
4.7.2 FEM results with experimentally measured shape of shells . . . 121
4.8 Summary and outlook . . . 124

5 Conclusions 125
5.1 Summary of findings . . . 125
5.2 Outlook and possible directions for future work . . . 128

Chapter 1

Introduction

Thin spherical shells are ubiquitous in both engineering (*e.g.*, microcapsules, domes, and storage tanks) and nature (*e.g.*, nuts and eggs). The majority of shells have a role to protect the inner material from externally imposed loads. However, most shells tend to buckle at much lower pressure loads than what is predicted by classic theory, due to their highly sensitive nature to imperfections. There have been extensive theoretical and computational studies on the imperfection sensitivity of buckling. Still, there is a striking lack of experimental research to corroborate these predictions, especially for spherical shells. In the past, classical buckling tests have been performed with spherical shells that were fabricated through a variety of techniques, including metal spinning, plastic vacuum drawing, aluminum machining, and electro-forming. These shells tended to be plagued by uncontrollable imperfections which result in scattered and unpredictable buckling pressures. In this thesis, to address this issue, we first introduce a novel mechanism based on liquid film coating to fabricate thin spherical shells of nearly uniform thickness. We then utilize this technique to investigate the role of geometric imperfections on the buckling strength of the shell.

In Sec. 1.1, we provide examples of spherical shells. Then, in Sec. 1.2, we review the literature on the buckling of spherical shells. We provide an overview of some experimental studies on the buckling of shells with imperfections in Sec. 1.3 and on the fabrication of spherical shells in Sec. 1.4. We describe the liquid film coating to produce thin structures in Sec. 1.5 and finally, the outline of the thesis in Sec. 1.6.

1.1 Spherical shells and their applications

Shells are structures bounded by two curved surfaces where the distance between the two surfaces, which is the shell thickness, h, is small in comparison with all other dimensions of the structure (*e.g.*, the radius, R, for spherical shells) (Ventsel & Krauthammer, 2001). Spherical shells appear across a wide range of length-scales in both engineering and nature; R ranges from the micrometer to several hundred meters.

For instance, at micrometer scale, microcapsules are shells that surround microparticles, bubbles, or liquid drops (Datta et al., 2014). These microcapsules can be used for storage, transport or/and controlled release of inner materials (Ibarz et al., 2001). Such microscopic shells find applications for example in agricultural chemicals (Tsuji, 2001), food additives (Augustin & Hemar, 2009), pharmaceuticals (Ibarz et al., 2001), cosmetic components (Karnik et al., 2008), and restorative agents for self-healing materials (Brown et al., 2004). In many of these practical settings, accurate prediction of mechanical properties and robust fabrication are required for the purpose of use.

At the centimeter scale, slender shells abound in our daily life, for example: contact lenses, sport balls, helmets, and food products (*e.g.*, chocolate bonbons). Spherical shells are also found in many biological forms, mostly for protective purposes such as in eyewalls (Myers et al., 2010), skulls (Hu et al., 2012), eggs (Stoddard et al., 2017), nutshells and pollen grains (Katifori et al., 2010). As a specific example, the eyewall, which consists of the collagen-rich sclera and the cornea, acts as a protective shell for the inner structures of the eye (Myers et al., 2010). The mechanical response of sclera to an increase in intraocular pressure has been found to be related with glaucoma, which causes blindness (Burgoyne et al., 2005; Myers et al., 2010) Understanding the response of the eyewall to external pressure is also important, given that ocular injuries from blast have recently increased in the war field (Bhardwaj et al., 2014). Bhardwaj et al. (2014) developed a computational model of blast loading on the human eye to elucidate the injury mechanism associated with the blast wave and investigated the stresses and deformations inside the globe under dynamic loading.

For naturally occurring shells, Hu et al. (2012) suggested that shells for different protective functions will exhibit different trends for their thickness to radius ratio, as indicated by a theoretical scaling analysis on experimental data of eggs, turtle shells, skulls, and whales.

Within civil, mechanical, and architectural engineering, thin spherical shells of even larger size, from meters to hundred meters, are used for a variety of structural applications. For example, architectured domes have been constructed since the prehistory (Fitch & Branch, 1960). Common construction material for these domes include mud, snow, stone, wood, brick, and concrete. Nowadays, rib-stiffened structure and steel-reinforced concrete for improving the load bearing capacity of domes are widely used, as we shall describe in Sec. 4.1. Moreover, shells are used for the purpose of storage and transport. Storage structures such as cargo tanks for ship transportation of liquified natural gas (Pedersen & Jensen, 1995) and containment vessels for nuclear power plants (Pedersen & Jensen, 1995) tend to comprise a complete spherical shape. Many types of transportation vehicles also have spherical shell segments as a part of their structure, for example, submersibles (Nash, 1995) and aircraft nose structures (Brown et al., 1983).

Often, the utility of a spherical shell depends crucially on its response to an externally imposed local load or uniform pressure. Shells buckle when these loading conditions reach a threshold value, *e.g.*, a critical pressure, thereby reducing its volume by forming a localized indentation on its surface. In Fig. 1-1, we present four representative examples of spherical shell structures, over a wide range of length scales, that have buckled under an imposed load. An optical microscopic image of a solid-shell microcapsule is shown in Fig. 1-1(a). Datta et al. (2012) fabricated these microcapsules using a microfludic device and studied their buckling behavior. First, water-in-oil-in-water droplets were prepared by microfluidic techniques, and then, the middle oil phase was polymerized to form a solid shell. Their microcapsules buckled when the external osmotic pressure was higher than a critical value, and then released their encapsulated contents. In many cases, these microcapsules are inhomogeneous, with a spatially varying thicknesses profile and elastic constants. Datta et al. (2012)

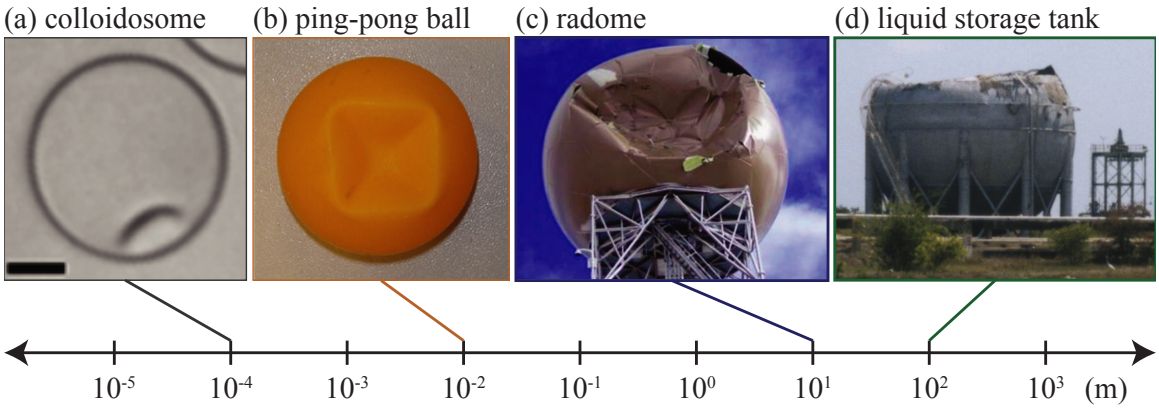

Figure 1-1: **Buckling of spherical shells across length-scales.** (a) Colloidal capsule buckled under osmotic pressure. Scale bar, 20 µm (Datta et al., 2012). (b) A ping-pong ball buckled in response to impact (Dong et al., 2008). (c) The radome in Reno, Nevada was punctured by extremely violent winds in a typhoon (Belles, 2017). (d) Liquid storage tank buckled under negative internal pressure, in Penuelas, Puerto Rico (Godoy, 2016).

were able to predict the critical buckling pressure of these microcapsules by applying shell theory using the thickness of the thinnest part.

Going up in length scale, in Fig. 1-1(b), a buckled ping-pong ball is presented as an example at the centimeter scale. Experiments with ping-pong balls demonstrated that the deformation and buckling mode of thin spherical shells can depend on the loading rate (Dong et al., 2008).

Continuing our progression of increasing sizes, now at the meter scale, in Fig. 1-1(c), we present a photograph of a radome, the type of shell structures that typically covers radar antennas. High wind loading (*e.g.*, in a hurricane) can severely damage radomes. The specific example of a spherical radome shown in Fig. 1-1(c) was empirically designed to sustain winds over 130 mph, and it was destroyed with a 140 mph wind in a typhoon (Belles, 2017).

Finally, in Fig. 1-1(d), an example of buckling of liquid storage tank under pressure loading is provided. Buckling of tanks under negative internal pressure can be commonly observed (Godoy, 2016), and this failure tends to be catastrophic.

In all of the examples above, the accurate prediction of the critical buckling load is crucial to prevent failure and improve the range of functional working conditions.

For a perfect spherical shell (*i.e.*, with perfect spherical geometry, without thickness variation, made with the homogeneous material, and under uniform external loading), the critical pressure at which buckling occurs can be calculated using a linearized analysis of shell theory (Zoelly, 1915), as we shall detail in the next section. However, many shells have imperfections, including deviations from the perfect shell geometry, variations of the shell thickness, non-uniform boundary conditions, and the existence of pre-buckling deformation. A deeper predictive understanding of the mechanisms that underlie this strong imperfection sensitivity calls for a careful investigation of buckling of spherical shells with tunable and well-defined imperfections, which is the central topic of this thesis.

1.2 Buckling of spherical shells

The buckling of shells has long been a canonical problem in the mechanics community (Babcock, 1983; Samuelson & Eggwertz, 2003; Elishakoff, 2014). The first prediction for the critical buckling load of a thin spherical shell under uniform external pressure was proposed by Zoelly (1915), who followed a linear buckling analysis to obtain the critical buckling pressure,

$$p_{\mathrm{c}} = \frac{2E}{\sqrt{3(1-\nu^2)}}\eta^{-2}, \tag{1.1}$$

where E is Young's modulus, ν is Poisson's ratio, and $\eta = R/h$ is the dimensionless radius of the shell, of radius R and thickness h. For decades, this theoretical prediction was found to be in disagreement with experimental results (Tsien, 1942; Kaplan & Fung, 1954; Homewood et al., 1961; Seaman, 1962; Krenzke & Kiernan, 1963; Carlson et al., 1967) and attempting to reconcile the two has been a cornerstone in structural mechanics (Elishakoff, 2014).

In Fig. 1-2, we plot a survey of historical experimental results from the literature for the knockdown factor,

$$\kappa_{\mathrm{d}} = \frac{p_{\max}}{p_{\mathrm{c}}}, \tag{1.2}$$

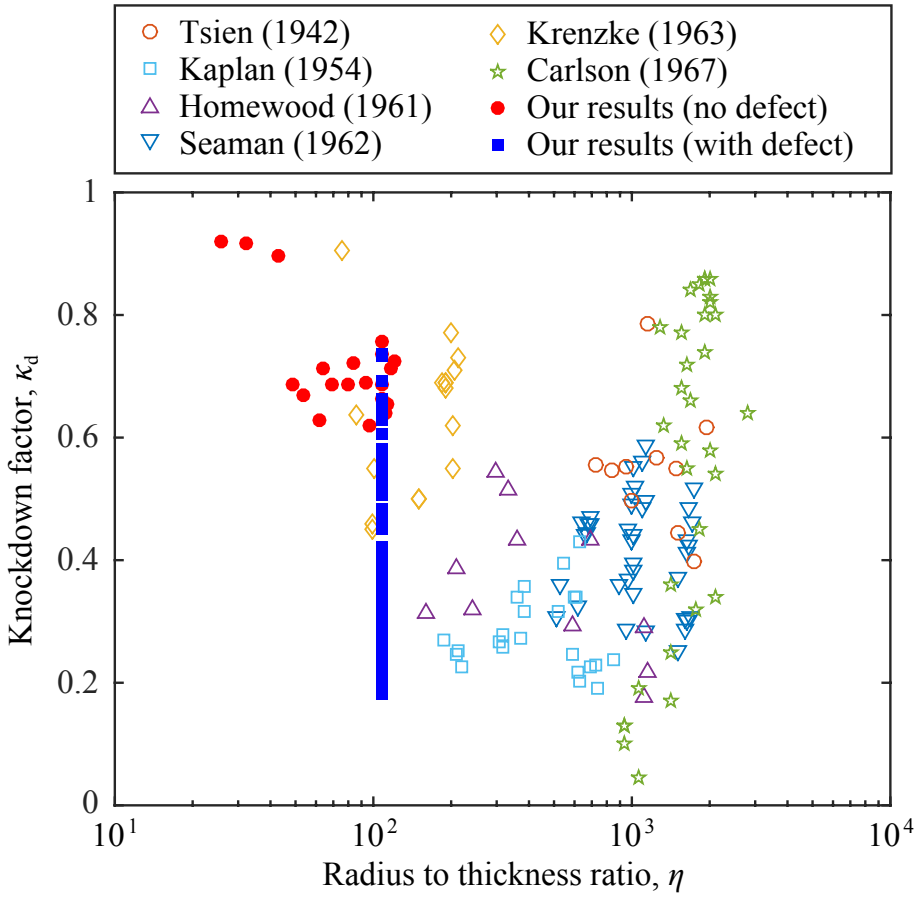

Figure 1-2: **Experimental results of the knockdown factor, κ_d, versus the radius to thickness ratio, $\eta = R/h$, of spherical shells.** Most of the past experiments (open symbols) were conducted with shallow spherical segments and resulted in a large variation in κ_d = 0.17-0.9. Carlson et al. (1967) used complete spherical shells and increased the knockdown factor from 0.05 to 0.86 by improving the shell surface and loading conditions. Our near-perfect shells (closed circles) have a small variation in κ_d = 0.61-0.92, which can be lowered significantly by engineering a dimple-like defect (closed squares).

defined as the ratio between the experimental buckling pressure, $p_{\max}$, and p_c from Eq. (1.1), as a function of the dimensionless shell radius, η. When a uniform external pressure is imposed, the most shells actually buckled at pressure $p_{\max}$ that is much lower than p_c. In this collection of historical experimental studies, the dimensionless shell radius was varied in the range $76 \leq \eta \leq 2834$, resulting in a wide spread of knockdown factors: $0.17 \leq \kappa_d \leq 0.9$. The general trend of these data is that κ_d decreases with increasing values of η, albeit with a broad spread. Low precision spherical shells produced by metal spinning (Kaplan & Fung, 1954; Homewood et al., 1961) or plastic vacuum drawing (Seaman, 1962) were found to buckle at relatively low values of the critical pressure ($0.17 < \kappa_d < 0.8$), compared to the theoretical prediction of Eq. (1.1), presumably due to significant material and geometric imperfections imparted through the fabrication process. By contrast, high precision shells fabricated by machining aluminum (Krenzke & Kiernan, 1963) tended to attain higher buckling pressures ($0.45 < \kappa_d < 0.9$), but still with considerable scatter. Note that most of these experimental investigations were conducted with shallow spherical shell segments.

Complete spherical shells were fabricated by electro-forming (Thompson, 1960; Carlson et al., 1967) with a quality of surface finish that could be enhanced through improvement of the fabrication process and a chemical polishing treatment to reduce the thickness variation, thereby increasing the knockdown factor from $\kappa_d = 0.05$ to 0.86. Historically, these results were very important in unequivocally providing a direct correlation between large imperfections and the low values of the knockdown factor; improving the surface finish reduced the magnitude of the imperfections and led to an increase of the knockdown factor. However, in their experiments, the imperfection could not be varied systematically, and consequently, the quantitative relationship between the imperfection and the knockdown factor was unrevealed. Still, all these findings have led to the now well-established recognition that the critical buckling load of a shell structure is highly sensitive to imperfections.

Explanations for the large discrepancies between theory and experiments have been proposed (von Kármán, 1939; von Kármán et al., 1940; von Kármán & Tsien,

1941) by finding equilibrium states of the shell involving large deflections that can be maintained by a much lower applied load than p_c. These studies suggested that the knockdown factors were connected with the elastic post-buckling behavior of shells. Subsequently, Tsien (1942) assumed the existence of arbitrary disturbances (initial deformation), and attributed the knockdown factors to the highly unstable post-buckling behavior of the shells, and compared his theory against experiments.

In 1945, Koiter (1945) made a groundbreaking contribution to the field of buckling by developing the general theory of stability for elastic structures subject to conservative loading. In this work, he introduced an asymptotic method to connect the initial post-buckling behavior with the sensitivity to imperfections. Following the English translation (from Dutch) in 1967 of Koiter's seminal work, there was an upsurge of research on the imperfection sensitivity of the buckling of thin structures and his general theory was applied to a variety of shell structures and loading conditions (Hutchinson & Koiter, 1970). In these investigations, the discrepancies between theory and experiments were attributed to variations of the shell thickness, nonuniformity of loading (Bijlaard & Gallagher, 1959), boundary conditions (Kobayashi, 1968), an influence of pre-buckling deformations (Almroth, 1965), and deviations from the perfect shell geometry (Budiansky & Hutchinson, 1972). Focusing on cylindrical shells, Babcock (1983) performed a direct comparison of the effect on buckling between different types of imperfection from these various studies (Bijlaard & Gallagher, 1959; Kobayashi, 1968; Almroth, 1965; Budiansky & Hutchinson, 1972) and concluded that the most important factor was the presence of geometric imperfections.

1.3 Experimental investigations on the imperfection sensitivity of shell buckling

As noted by Babcock (1983), fundamental experimental research to help advance the understanding of imperfection sensitivity has typically lagged behind theoretical analysis and computation. As a result, even to date, the practical design of shell struc-

tures tends to be based on classical results, such as Eq. (1.1), together with empirical corrections (Samuelson & Eggwertz, 2003). In these empirical approaches, from the collected experimental data of the knockdown factor, such as the plot in Fig. 1-2, as a function of the radius to thickness ratio, a lower bound can be represented by an equation of the fitted curve. Then, this lower-bound provides a correction factor for shell design. Still, attempts to experimentally validate theories on imperfection sensitivity were done extensively for cylindrical shells (Elishakoff, 2014) and, more rarely, for spherical shells (Seaman, 1962; Chen, 1959). In these experimental studies on imperfection sensitivity, the shape of the specimen was precisely measured before carrying out the buckling test. However, experimental fabrication protocols typically impart randomness to the size and shape distributions of shell defects. As such, deterministic relationships have rarely been found between representative imperfection distributions and the load-bearing capacity of the shell.

With an alternative point of departure, statistical approaches have also been developed to study the problem of shell buckling (Elishakoff, 2014). First, initial imperfections were measured and collected to provide imperfection distribution. Characteristic imperfection distributions were associated with the different fabrication processes. The probability of buckling of shells, made by the specific fabrication process, at given pressure was quantified. However, this probabilistic approach has not yet been widely adopted for design purposes due to the lack of high-precision experimental information on the characteristic distributions of the imperfections and knowledge of their influence on buckling.

In contrast to spherical shells, cylindrical shells with near-perfect geometry and with intended imperfections have been fabricated and tested in axial compression since the 1960s. For example, Babcock & Sechler (1963) fabricated cylindrical copper shells by electro-forming that consisted of plating a copper shell on an accurately machined wax mandrel and later melting the mandrel. To ensure uniform plating, the mandrel was rotated and the bath containing a copper anode was mixed during the process. The shells without the intended imperfection had knockdown factors in the range $0.72 \leq \kappa_{\mathrm{d}} \leq 0.76$. An initial imperfection with a half sine geometry along the

axial direction was systematically varied and their effect on the buckling load was investigated. As the imperfection amplitude increased, the knockdown factor decreased as low as 0.44. Tennyson (1963, 1964, 1968); Tennyson & Welles (1968) fabricated cylindrical shells by spin-casting a liquid photoelastic plastic in an acrylic tube. In these experiments, to ensure a circular cross-section and to minimize thickness variations, a plastic liner shell was first cast onto the inside of an acrylic tube. Finally, after a liquid releasing agent was added, a liquid photoelastic plastic was cast. High rotational speeds ($\approx$ 800 rpm) were required to evenly distribute the liquid. Upon curing, the final photoelastic shell was pushed out from the mold by an applied axial pressure. These spin-casted shells had a $\pm 6\%$ thickness variation and were found to have high knockdown factors within $0.86 \leq \kappa_{\mathrm{d}} \leq 0.94$ (Tennyson, 1963; Tennyson & Welles, 1968). Then, these near perfect cylindrical shells were used to study post-buckling behavior (Tennyson, 1964) and to find the effect of circular cut-outs on the buckling process (Tennyson, 1968).

More recently, experimental studies on imperfection sensitivity of cylindrical shells have been regaining interest in the mechanics community. A few studies used engineered imperfections for a variety of purposes, including reducing the imperfection sensitivity (Ning & Pellegrino, 2017) and tailoring the elastic post-buckling behavior of cylindrical shells (Hu & Burgueño, 2017).

To increase the knockdown factor of cylindrical shells, Ning & Pellegrino (2017) fabricated circumferentially wavy cylindrical shells that were imperfection insensitive under axial compression. Three wavy shells and two circular shells were fabricated by laying a composite laminate on steel mandrels, as shown in Fig. 1-3(a). The magnitude of the resulting imperfection, δ, as measured by the difference between the designed and the fabricated shell, were $\bar{\delta} = \delta/h = 2.2 \pm 0.78$. These wavy cylindrical shells collapsed at higher loads than the buckling load expected for a perfect wavy shell, with $\kappa_{\mathrm{d}} = 1.08$-$1.12$. The experimentally measured knockdown factors of wavy shells were also predicted through simulations for shells that contained the actual geometry of the measured imperfections. On the other hand, circular shells had relatively low knockdown factors $\kappa_{\mathrm{d}} = \{0.499, 0.589\}$.

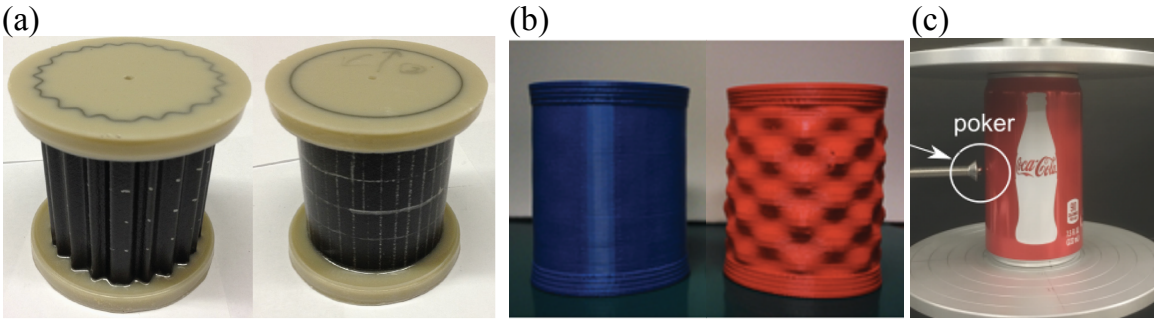

Figure 1-3: **Cylindrical shells with seeded geometric imperfections.** (a) Composite cylindrical shells that have wavy (left) and circular (right) cross section (Ning & Pellegrino, 2017). (b) 3D printed cylindrical shells with eigenshape-based geometries (Hu & Burgueño, 2017). (c) Cylindrical shells under axial loading and poking (Virot et al., 2017).

From the load carrying behavior of a shell, a defect can be characterized, even before buckling occurs. Virot et al. (2017) measured the response of cylindrical shells to poking and identified a stability landscape that characterizes the stability of both perfect and imperfect shells, in the case where a single defect dominates. These authors axially compressed cylindrical shells and probed them from the side with a 'poking' force, as shown in Fig. 1-3(c). The stability of these shells was described by a two-dimensional surface in a three-dimensional phase space (axial load, poking displacement, and poking force).

Instead of being regarded as a failure, the buckling of shells can also be used as opportunities for smart applications such as energy harvesters and self-powered sensors. Hu & Burgueño (2017) designed eigenshape-based geometries and fabricated wavy cylindrical shells through polymer-based 3D printing. Their experiments and simulations showed that the elastic post-buckling response could be controlled by varying the number of waves in the axial and circumferential directions.

1.4 Experimental to fabrication of spherical shells

Above, we reviewed the results of buckling tests with thin spherical shells in Sec. 1.2 and experiments with cylindrical shells that contain engineered imperfections in Sec. 1.3.

Imperfect spherical shells exhibited a scatter of values in their knockdown factor ($\kappa_{\mathrm{d}} = 0.17 - 0.9$, see Fig. 1-2), while near perfect cylindrical shells had consistently higher knockdown factors ($0.72 \leq \kappa_{\mathrm{d}} \leq 0.76$ with electro-forming and $0.86 \leq \kappa_{\mathrm{d}} \leq 0.94$ with spin-casting). For spherical shells, most of the experimental investigations were conducted with shallow spherical cap segments produced by metal spinning (Kaplan & Fung, 1954; Homewood et al., 1961), plastic vacuum drawing (Seaman, 1962), and machining aluminum (Krenzke & Kiernan, 1963). Complete spherical shells were fabricated by electro-forming (Thompson, 1960; Carlson et al., 1967). To improve the surface quality of shells, Carlson et al. (1967) tended to first improve both the surface conditioning of the mandrel and the mandrel casting process. Second, because the thickness was not uniform and varied depending on the location of two electrodes, they chemically polished the thicker regions. Through the combined improvement, the knockdown factor was increased from $\kappa_{\mathrm{d}} = 0.05$ to 0.86. However, the geometry (*e.g.*, thickness and its uniformity) of the shells was not predictable and the imperfection could not be systematically varied (Carlson et al., 1967). Therefore, there is a need for simple, predictable and versatile fabrication methods of spherical shells.

Some recent studies have used 3D printing to fabricate shells (Ning & Pellegrino, 2017) (see Fig. 1-3), a technique that is particularly appropriate to obtain a complex shapes. However, circular cylindrical shells showed a relatively low quality, with $\kappa_{\mathrm{d}} = \{0.499, 0.589\}$, and wavy cylindrical shells showed material failure before buckling. Thus, 3D printing still requires improvement to be used for shell buckling studies.

Recently, fabrication of elastic shells using elastomers has facilitated a new wave of exploration of the mechanics of shells, including geometry-induced rigidity (Lazarus et al., 2012), localization of deformation (Nasto et al., 2013), and wrinkling on curved surfaces (Terwagne et al., 2014). In these studies, double-curved shells were made by molding process filling polymeric liquid into a designed solid mold, which results in thick shells, or by coating polymeric liquid on the curved surface with empirical adjustments to obtain the required thickness of thin shells, with no predictive knowledge to design the shells. The fabrication of shells by coating polymeric liquid has the potential to result in thin shells with high quality. Moreover, these shells can be

deformed elastically at lower loads than those required to deform metal and plastic shells, which offers practical advantages for conducting buckling test. Therefore, in this thesis, we seek to develop a new method that is both robust and predictable to fabricate thin elastic shells with a high degree of flexibility in their material and geometric properties.

1.5 Liquid film coating to produce thin structures

In contrast to the empirical usage of liquid coating to fabricate double-curvature shells mentioned above, for flat and cylindrical surfaces, a variety of thin film coating techniques are well established (Weinstein & Ruschak, 2004). In this section, we will review a few existing liquid coating techniques to produce thin films. A significant advantage for these flat and single curvature geometries is that, when compared to their double-curved counterparts, they are more amenable to theoretical modeling to predict how the final film thickness depends on the control parameters (Landau & Levich, 1942; Bretherton, 1961). In these cases, the flow driven by viscous stresses and held by capillary forces is 'frozen' as the media cools, cures or dries, yielding a defect-free and uniform thin structure. Consequently, these robust coating techniques have matured to be ubiquitous in both industry and in the laboratory.

The dynamics of viscous liquids is described by incompressible Navier-Stokes equations:

$$\rho\left(\frac{\partial \boldsymbol{v}}{\partial t} + \boldsymbol{v}\cdot\nabla\boldsymbol{v}\right) = \mu\nabla^2\boldsymbol{v} - \nabla\pi + \rho\boldsymbol{f}, \tag{1.3}$$

where t is the time, ρ is the density, μ is the viscosity, $\boldsymbol{v}$ and π are the Eulerian velocity and pressure fields, respectively, and $\boldsymbol{f}$ is the external force per unit mass. The external force can, for example, be gravity in the case of dip coating or a centrifugal force in the cases of spin-coating and spin-casting. The bases of each of these coating techniques - (i) dip coating, (ii) spin-coating and (iii) spin-casting - are described and explained in more detail next.

(i) Dip coating:

Dip coating is the simplest way of depositing a uniform thin film of liquid onto flat and cylindrical substrates (Scriven, 1988). In this case, the film thickness is determined by the competition between viscous forces, capillary forces and gravity. The faster the surface is withdrawn from the liquid bath, the thicker the film that is formed, up to a limit. Conversely, the thinner the film is desired, the slower the surface must be withdrawn.

Let us first consider dip coating of a 'continuous' sheet, as shown in Fig. 1-4(a), so the drainage reaches the steady state. When the viscosity of the liquid and the withdrawing speed are high enough to overshadow surface tension effects. The film thickness, h, is set by a balance between viscous drag ($\mu U/h$) and gravity ($\rho g h$), such that

$$h = c\left(\frac{\mu U}{\rho g}\right)^{1/2}, \tag{1.4}$$

where c is a proportionality constant (for example, $c = 0.8$ for Newtonian liquids (Spiers et al., 1974)), U is the speed of withdraw of the surface, and g is the acceleration of gravity. On the other hand, when the viscous drag, gravity, and surface tension all compete (Landau & Levich, 1942), one obtains

$$h = 0.994\left(\frac{\mu U}{\sigma}\right)^{1/6}\left(\frac{\mu U}{\rho g}\right)^{1/2}, \tag{1.5}$$

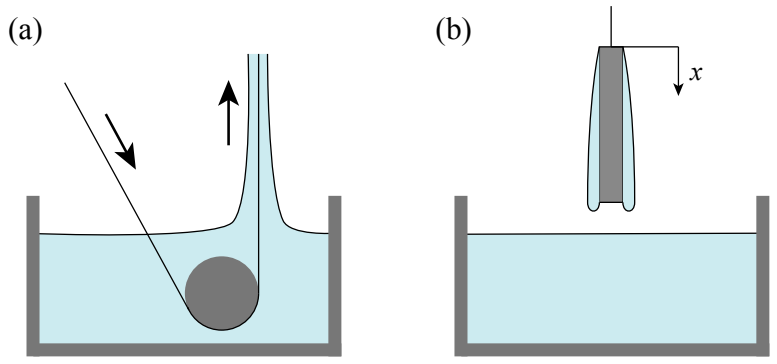

Figure 1-4: **Schematics of dip-coating processes.** (a) Dip-coating of a continuous sheet, in which the drainage reaches the steady state. (b) Dip-coating of a slab, where the thickness of a liquid film coated on the slab increases with x.

where σ is the surface tension of the liquid. When the substrate is a slab (see Fig. 1-4(b)) or cylinder, the deposited film has a parabolic profile at the leading edges:

$$h = \sqrt{\frac{\mu}{\rho g}\frac{x}{t}}, \tag{1.6}$$

with x the downward distance from the leading edge and t the time since the leading edge left the bath.

(ii) Spin-coating:

To generate (ultra-) thin sheets, spin-coating is now a common method to attain constant and tunable film thicknesses (Emslie et al., 1958; Meyerhofer, 1978). It is essential in lithographic techniques that are now regulrarly employed in laboratory settings to fabricate microfluidic devices (Wu et al., 2005), as well as in the micro-electronics industry (Rai-Choudhury, 1997). During the spinning of a flat disk, the liquid is drained radially, and centrifugal and viscous forces compete. The thinning of a Newtonian liquid on a rotating disk was first derived as (Emslie et al., 1958)

$$\frac{dh}{dt} = -\frac{2\rho\Omega^2 h^3}{3\mu} \tag{1.7}$$

where t is the rotating time and Ω is the rotating speed. From this equation, the thickness of the film is obtained as (Scriven, 1988)

$$h(t) = \frac{h_\mathrm{i}}{\sqrt{1 + 4\rho\Omega^2 h_\mathrm{i}^2 t/3\mu}} \tag{1.8}$$

with uniform initial thickness, h_i.

(iii) Spin-casting:

Similarly to spin-coating, spin-casting also exploits centrifugal forces, but now on a rotating cylindrical surface to evenly distribute a polymer solution. This technique can be used to fabricate nearly constant thickness shells in a highly controllable manner (Kalpakjian & Schmid, 2014). High rotational speeds (of the order of 100 to 1000 rpm) are required to evenly distribute the liquid on the cylindrical surface.

Centrifugal forces drive out any air bubbles existing in the liquid and produce a smooth film. The final thickness is set by the amount of polymer solution. This technique was instrumental in identifying the role of imperfections on the critical buckling conditions of cylindrical shells in the 1960s (Tennyson, 1968; Elishakoff, 2014), as mentioned in Sec. 1.3.

For double-curved surfaces such as spherical shells, there is a need for simple and versatile fabrication methods that are analogous to the coating of fibers, plates and cylinders and able to yield uniform, controllable and predictable results.

1.6 Outline of the thesis

This chapter has introduced the context and the objective of this thesis. We were motivated by a lack of experimental studies on the relationship between the knockdown factor and the defect geometry for spherical shells. Therefore, we seek to develop a fabrication technique to produce near perfect thin spherical shells. With variations of this technique, we will conduct experiments to find the role that a geometric imperfection has on the buckling pressure of a spherical shell.

In Chapter 2, we investigate fabrication mechanism of thin spherical shells by the coating of polymer solution onto a spherical surface; upon curing the liquid film yields thin structure. We provide a predictive model to describe the drainage dynamics, which set the geometry of final shell structure. Moreover, we explain the uniformity, robustness, and tunability of our fabrication mechanism. In Chapter 3, we revisit the classic problem of shell buckling, for which employ the technique developed in Chapter 2. We fabricate thin elastic hemispherical shells containing a single precisely engineered geometric imperfection. Through a series of precision buckling tests, we present quantitative relationships between the knockdown factor and the geometry of an imperfection that we design into the shell. We demonstrate that our experimental results for these knockdown factors can be predicted by both the finite element method (FEM) and numerical analyses of a reduced shell theory model. In Chapter 4, we fabricate bilayer shells with two different polymer solutions that contain a defect.

In these bilayer shells, uncrosslinked residual polymers diffuse from one layer to the other. This residual swelling changes the shell geometry over time and produces residual stresses. We experimentally investigate the effect of residual swelling in modifying the buckling pressure of our imperfect bilayer shells.

Chapter 2

Fabrication of thin spherical shells

Various manufacturing techniques exist to produce double-curvature shells, including injection, rotational and blow molding, as well as dip coating. However, these industrial processes are typically geared for mass production and are not directly applicable to laboratory settings, where versatile and predictable prototyping tools are desirable. In this chapter, we study the rapid fabrication of hemispherical elastic shells by the coating, viscous drainage and subsequent curing of polymer solutions on spherical molds. We experimentally characterize how the curing of the polymer affects its drainage dynamics and eventually selects the shell thickness. The coating process is then rationalized through a theoretical analysis that predicts the final thickness, in quantitative agreement with experiments and simulations. Our approach provides a rapid, robust and predictable mechanism to fabricate thin elastic shells with a nearly constant thickness, which we will use to study shell buckling in Chapters 3 and 4.

In Sec. 2.1, we describe our motivation and present a literature review. Then, we introduce the experimental process and present results on the shell thickness in Sec. 2.2, followed by a quantification of the rheology of polymer solutions and drainage dynamics in Secs. 2.3-2.4. In Sec. 2.5, lubrication equations are combined with the time-varying viscosity to model our system. In Sec. 2.6, the thickness uniformity is demonstrated by experiments and a theoretical model. The other factors that affect the thickness and uniformity of the shells are discussed in Sec. 2.7. Finally, the robustness and tunability of this fabrication technique are described in Secs. 2.8-2.9.

2.1 Motivation and literature review

Our motivation to develop a novel experimental technique to fabricate thin shells stemmed from the need for more systematic and extensive experimental studies of the buckling of spherical shells. As introduced in Chapter 1, fabrication of elastic shells using elastomers was implemented to explore novel mechanics of elastic shells such as geometry-induced rigidity (Lazarus et al., 2012), localization of deformation (Nasto et al., 2013), and wrinkling on curved surfaces (Terwagne et al., 2014). In these past studies, double-curved shells were produced by casting a polymer solution with a custom designed mold (resulting in thick shells), or by coating a polymer solution on the curved surface (although this technique at the time is purely empirical and not supported by a predictive understanding, which limited the design process). Moreover, since the 1960s, there has been a lack of experimental studies on the imperfection sensitivity of the buckling of spherical shells. Thus, we seek to provide a robust and predictable method to fabricate thin elastic shells with flexibility in the design of their material and geometric properties. The fabrication technique that we have developed can be used to broaden the scope of experiments on the mechanics of buckling of thin elastic spherical shells, as well as will be demonstrated in Chapters 3 and 4 of this thesis.

Hollow chocolate shells have been fabricated since the 1600s by pouring molten chocolate into a mold and then draining the excess. Solidification upon cooling ceases the flow and results in a solid chocolate shell of nearly constant thickness (Crawford, 2012). Beyond chocolatiers, the polymer industry abounds with needs to fabricate thin shell structures, and a plethora of manufacturing processes have been developed for this purpose, including injection (Rees & Catoen, 2006), rotational (Crawford, 2012) and blow molding (Lee, 2006), as well as dip coating (Scriven, 1988). All of the above techniques have limitations in the thickness of the shells that they can produce (*e.g.*, $\sim$0.5 mm for injection molding) and its uniformity (typically $\sim$20% for rotational molding (Beall, 1998)). Furthermore, there is a striking lack of predictive theoretical models due to the multi-physics complexity of the processes. For example,

rotational molding involves coating the inner surface of a hollow mold with a polymer melt, which is then rotated biaxially while applying a decreasing heating profile until a solid shell is formed (Crawford, 2012). As another example, injection molding is developed for mass-production manufacturing and requires costly precision-machined molds that are inflexible to variations in the geometry of the part (Rees & Catoen, 2006). In these processes, the optimization of the control parameters is largely tuned empirically, with compromises on versatility, predictability, and reproducibility (Beall, 1998). As such, these techniques are not directly applicable to laboratory settings where adaptable, inexpensive, and predictable rapid-prototyping tools are more desirable. This is particularly the case for the fabrication of thin, smooth and flexible three dimensional structures.

For flat and cylindrical surfaces, a variety of thin film coating techniques are well established (Weinstein & Ruschak, 2004). A significant advantage for these geometries is that, when compared to their double-curved counterparts, they are more amenable to theoretical modeling to predict how the final film thickness depends on the control parameters (Landau & Levich, 1942; Bretherton, 1961). In these cases, the flow, driven by viscous stresses and held by capillary forces, is 'frozen' as the media cools, cures or dries, yielding a defect-free and uniform thin structure. As a result, these robust coating techniques have matured to be ubiquitous in industrial and laboratory settings. To generate (ultra-) thin sheets, spin-coating is now widespread (*e.g.*, in microfluidics and microfabrication) to attain constant and tunable film thicknesses (Emslie et al., 1958; Meyerhofer, 1978). Similarly, spin-casting exploits centrifugal forces on a rotating cylindrical surface to evenly distribute a polymer solution and fabricate nearly constant thickness shells in a highly controllable manner (Kalpakjian & Schmid, 2014). This technique was instrumental in identifying the role of imperfections on the critical buckling conditions of cylindrical shells in the 1960s (Tennyson, 1968; Elishakoff, 2014) as mentioned in Chapter 1. The imperfection sensitivity of thin shells will be studied in detail later in Chapter 3. For double-curved surfaces such as spherical shells, there is a need for simple and versatile fabrication methods that are analogous to the coating of fibers, plates, and cylinders

and able to yield uniform, controllable and predictable results.

2.2 Fabrication method and the resulting thickness of thin shells

In this section, we first introduce the experimental procedure to produce thin spherical shells. We also describe materials and geometrical properties we explore. Then, we present experimental results on the shell thickness. Moreover, a scaling analysis explains the trend of the thickness data.

2.2.1 Experiments to fabricate shells with a variety of materials and geometrical properties

In Fig. 2-1(a), we present a series of photographs that illustrate our coating process. A silicone-based liquid polymer solution is poured onto a rigid spherical mold, drains under the effect of gravity and eventually covers the entire surface. With time, cross-linking of the polymer film that emerges from the drainage process yields a thin elastic shell that can be readily peeled from the mold.

We used both vinylpolysiloxane (VPS, Elite Double 8, 22 and 32, referenced throughout the text as VPS-8, VPS-22 and VPS-32, respectively, Zhermack, Italy) and polydimethylsiloxane (PDMS, Sylgard 184, Dow Corning), at different mixing and curing conditions to achieve a variety of rheological properties. VPS was mixed at room temperature (20°C) with a base/catalyst ratio 1:1 in weight using a centrifugal mixer (ARE-310, Thinky Co.) for 10 s at 2000 rpm (clockwise), and then 10 s at 2200 rpm (counterclockwise). Curing of the PDMS was performed in a convection oven at 20, 35 and 40°C. The base and curing agent were mixed in a 10:1 weight ratio using a centrifugal mixer for 30 s at 2000 rpm (clockwise), and then for 30 s at 2200 rpm (counterclockwise). We sped up the curing process using a cure accelerator (3-6559 Cure Accelerator, Dow Corning) that was mixed to the PDMS elastomer in the weight proportion 5:1 (PDMS-base:Cure-accelerator).

Figure 2-1: **Photographs of coating process.** (a) Liquid VPS-22 is poured onto a metal sphere ($R = 38$ mm), then drains under gravity and eventually cures to produce an elastic shell. The time interval between each frame is 2 s. (b) Liquid VPS-22 is poured on to metal spheres in a range of radii, $1 \leq R\,[\text{mm}] \leq 375$. Scale bar, 10 mm.

The above procedure was repeated with various molds in a range of radii ($1 \leq R\,[\text{mm}] \leq 375$, see Fig. 2-1(b)). For the molds, we have used a polyacetal hemispherical mold, stainless steel balls, a spherical glassware and a gym-ball. Upon curing, the final thickness, h_f, of the elastic shells was measured with an optical microscope after cutting the shell along a meridian using a scalpel. Throughout the thesis, we only focus on the upper hemispherical part of the shells because the thickness of draining film and resulting shell steeply increases beyond the equator of the sphere.

We measured the final shell thicknesses and plot the value at the pole of each shell in Fig. 2-2. We found that $h_\text{f} \sim R^{1/2}$, and this result is robust and independent of either the details of the polymer/mold or the curing temperature. We also measured the thickness profile along a meridian of the hemispherical shells. The final thickness of these elastic shells is found to be uniform (to within 6.6% (VPS) and 8.7% (PDMS)

mean-standard deviation of thickness over the meridian of the hemisphere), which will be more discussed in Sec. 2.6.

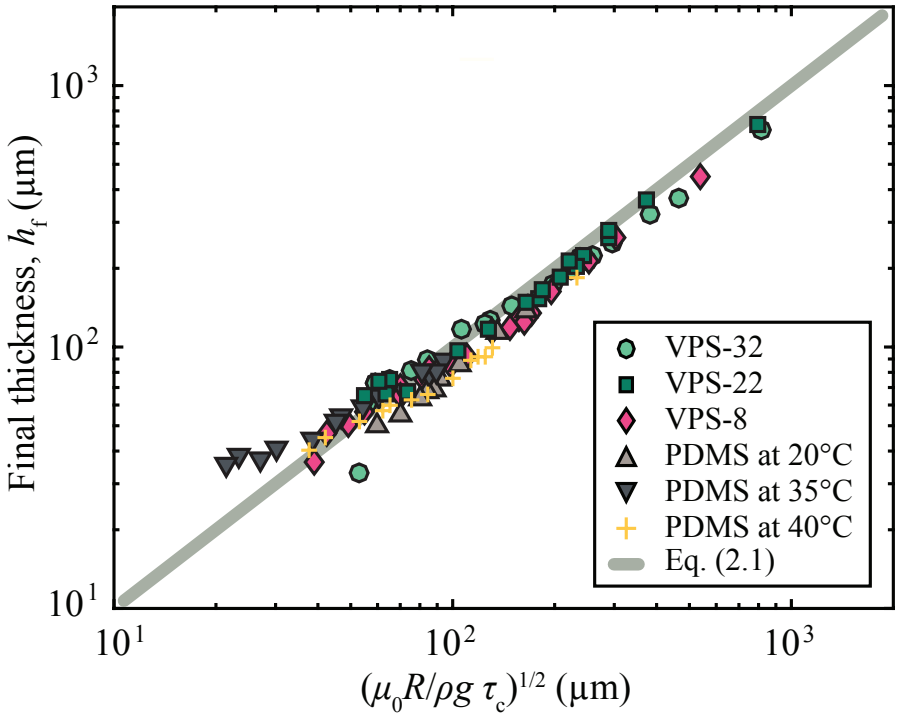

Figure 2-2: **Final thickness of elastic shells.** Thickness of the elastic shells, h_f, as a function of $\sqrt{\mu_0 R/(\rho g \tau_c)}$, for various polymer solutions (VPS and PDMS) and temperatures (20, 35, and 40°C for PDMS). The solid line corresponds to Eq. (2.1).

2.2.2 Physical ingredients that determine the thickness of the fabricated shells

The square-root dependence of h_f on R can be rationalized by balancing the characteristic curing time, τ_c, of the polymer solution and the characteristic drainage time, $\mu_0 R/(\rho g h_f^2)$, that is obtained when balancing the viscous stresses and gravity in the lubrication layer, such that

$$h_f \sim \sqrt{\frac{\mu_0 R}{\rho g \tau_c}}, \tag{2.1}$$

where μ_0 is a characteristic viscosity of the polymer (*e.g.*, its initial value), ρ is its density, and g is the acceleration of gravity. The fact that all the data in Fig. 2-2

collapse onto a master curve, irrespectively of the polymer and curing temperature, over a wide range of R, supports this scaling analysis. In Sec. 2.5, we will develop a theoretical description that more formally recovers this scaling. Before doing that, we continue with the investigation of the rheology of curing polymers that will be combined with the lubrication equations.

2.3 Time-varying viscosity of polymer solutions

The rheology of various polymer solutions (VPS-8, 22, 32 and PDMS) was characterized with a rheometer (AR-G2, TA Instruments) as a function of time and at a constant temperature (20°C for VPSs and 20, 35 and 40°C for PDMS). During the viscosity measurement, the shear rate was fixed at $\dot{\gamma} \approx u/h \approx 0.1$ s^{-1}, consistently with the characteristic drainage velocity ($u = 0.1$ mm/s) and film thickness ($h = 1$ mm). When the polymer solution drains over the hemisphere, the shear rate varies from zero at the apex to its peak value at the equator and also depends on R and t. In Sec. 2.6.3, it will be validated that $\dot{\gamma} \approx 0.1$ s^{-1} is indeed a good estimation by scrutinizing the shear rate over the full hemisphere within the drainage period and effects of its variation on the final shell thickness. The viscosity data were acquired every 10 s for VPS and 20 s for PDMS.

In Fig. 2-3, we plot the viscosity of various polymer solutions as a function of time for VPS-8, 22 and PDMS at 35 and 40°C, Fig. 2-5(b) for VPS-32, and Fig. 2-14 for PDMS at 20°C. The viscosity is nearly constant at first and then sharply increases as the polymer cures. The data for the measured viscosity was then fitted with the piecewise model proposed by our collaborators, Pierre-Thomas Brun (Princeton University), Gioele Balestra (EPFL), and François Gallaire (EPFL). The time-varying viscosity can be expressed as a piecewise function of the form

$$\mu(t) = \begin{cases} \mu_0 \exp(\beta t)\,, \text{if } t \leq \tau_c\,, \\ \mu_1 t^{\alpha}\,, \text{if } t > \tau_c, \end{cases} \tag{2.2}$$

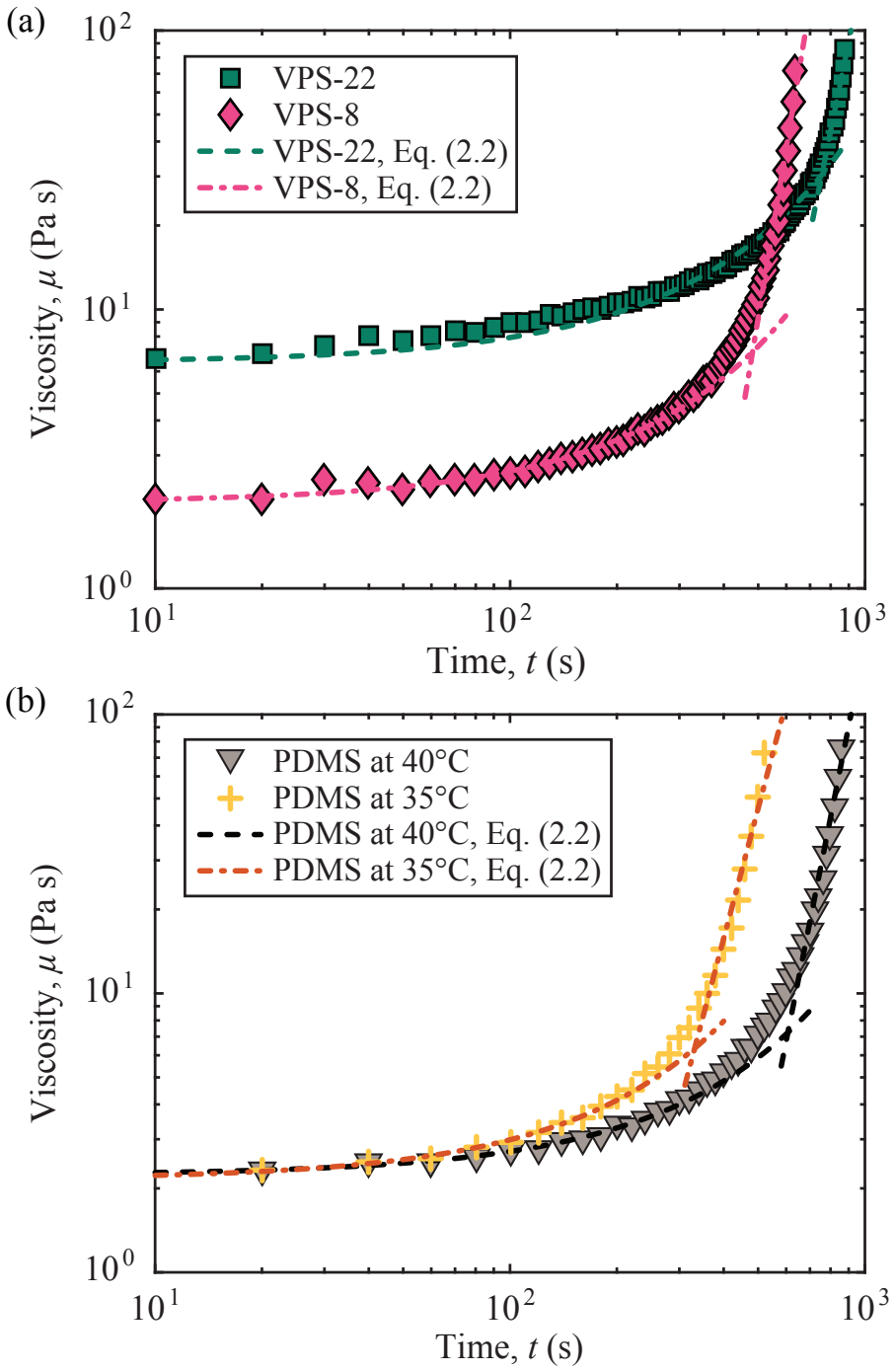

Figure 2-3: **Rheology of the polymer solutions.** Time evolution of the viscosity for (a) VPS-8 and 22 at 20°C, and (b) PDMS at 35 and 40°C. Points are experimental data and the dashed and dash-dot lines correspond to fits of the Eq. (2.2). The shear rate is fixed at $\dot{\gamma} \approx u/h \approx 0.1$ s^{-1}, which is consistent with the flow field during the coating process.

Table 2.1: **Coefficients to describe the time evolution of the viscosity of polymer solutions.**

Polymer	μ_0 (Pa.s)	α	$\beta(\times 10^{-3})$	τ_c (s)
VPS-32	7.1±0.2	5.3±0.7	2.06±0.09	574±11
VPS-22	6.5±0.3	6.3±0.7	2.05±0.01	738±16
VPS-8	2.0±0.1	7.7±1.2	2.57±0.01	479±7
PDMS, 20°C	2.4±0.1	3.7±0.2	0.056±0.001	2836±81
PDMS, 35°C	2.2±0.1	6.4±1.0	1.94±0.01	613±14
PDMS, 40°C	2.2±0.1	4.8±0.9	3.27±0.03	338±12

with $\mu_1 = \mu_0 \exp(\beta\tau_c)\tau_c^{-\alpha}$ chosen to ensure continuity at τ_c and where β and α are fitting parameters. Eq. (2.2) is fitted to the experimental data and found to accurately describe the viscosity evolution (Figs. 2-3 and 2-5). The initial viscosity, the curing time, and the model fitting parameters for the polymer solutions used in the experiments are presented in Table 2.1. The VPS polymers that we have used have initial viscosities in a range of $2.0 \leq \mu_0$ [Pa.s] ≤ 7.1, and the curing time varies from 479 to 738 s. The measuring temperature of PDMS has a negligible effect on the initial viscosity, $2.2 \leq \mu_0$ [Pa.s] ≤ 2.4, but significantly affects the curing time, $338 \leq \tau_c$ [s] ≤ 2836.

2.4 Free surface velocity profiles

We proceed by experimentally characterizing the drainage dynamics of polymer solution that results in a thin elastic shell upon curing of the polymer (Fig. 2-1(a)). As a representative case, we focus on VPS-32 poured onto a sphere with $R = 38\,\text{mm}$. We measured the free surface velocity as a function of space and time.

A schematic diagram of our system is presented in Fig. 2-4(a). A hemispherical mold is aligned such that gravity is parallel to the axis that connects its center to the pole; $\mathbf{g} = -g\,\mathbf{e}_z$. Both the local thickness, $h(\phi, t)$, and the free surface velocity, $u(\phi, t)$, of the draining film are assumed axisymmetric and vary in both time, t, and space (*i.e.*, zenith angle, ϕ).

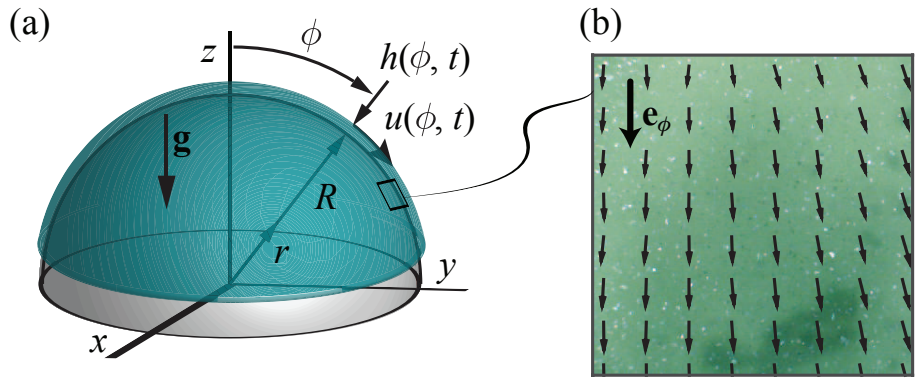

Figure 2-4: **Schematic diagram of the coating problem.** (a) $h(\phi, t)$ is the thickness of the liquid film and $u(\phi, t)$ is the flow velocity at the liquid-air interface during drainage. (b) Instantaneous velocity field at $t = 60$ s in a 1×1 cm^2 region of the VPS-32 film located at $\phi = 60°$ of a sphere ($R = 38$ mm), obtained through PIV.

The velocity field of the draining polymer was measured using an open-source package for particle imaging velocimetry (PIVlab (Thielicke & Stamhuis, 2014)). A powder spray (Sparkler, Body Shop) was sputtered onto the surface of the flow and imaged using a digital microscope camera (Discovery VMS-004, Veho).

At the pole ($\phi = 0$), the fluid flow vanishes due to symmetry. Elsewhere, the velocity is predominantly in the polar direction, $\mathbf{e}_\phi$. This is supported by the representative velocity field shown in Fig. 2-4(b), obtained through PIV, at $t = 60\,$s in a $1{\times}1\,$cm^2 region of the film whose center is located at $\phi = 60°$. Moreover, the instantaneous local velocity, $u(\phi, t = 60$ s) is plotted as a function of the zenith angle, ϕ, in Fig. 2-5(a) and is found to increase approximately linearly with ϕ.

In Fig. 2-5(b), we plot the free surface velocity as a function of time at the specific polar location, $u(\phi = 60°, t)$. The free surface velocity progressively slows down and eventually comes to a halt in finite time. This leaves a coating of the final thickness, h_f, on the mold. The velocity profile and its arrest are found to correlate directly to the change in the viscosity, μ, as the polymer cures. We overlapped the viscosity profile obtained in Sec. 2.3 onto the time variation of the velocity in Fig. 2-5(b). Note that the initial drainage and subsequent curing regimes are separated by the characteristic curing time of the polymer, τ_c, which is significantly larger than

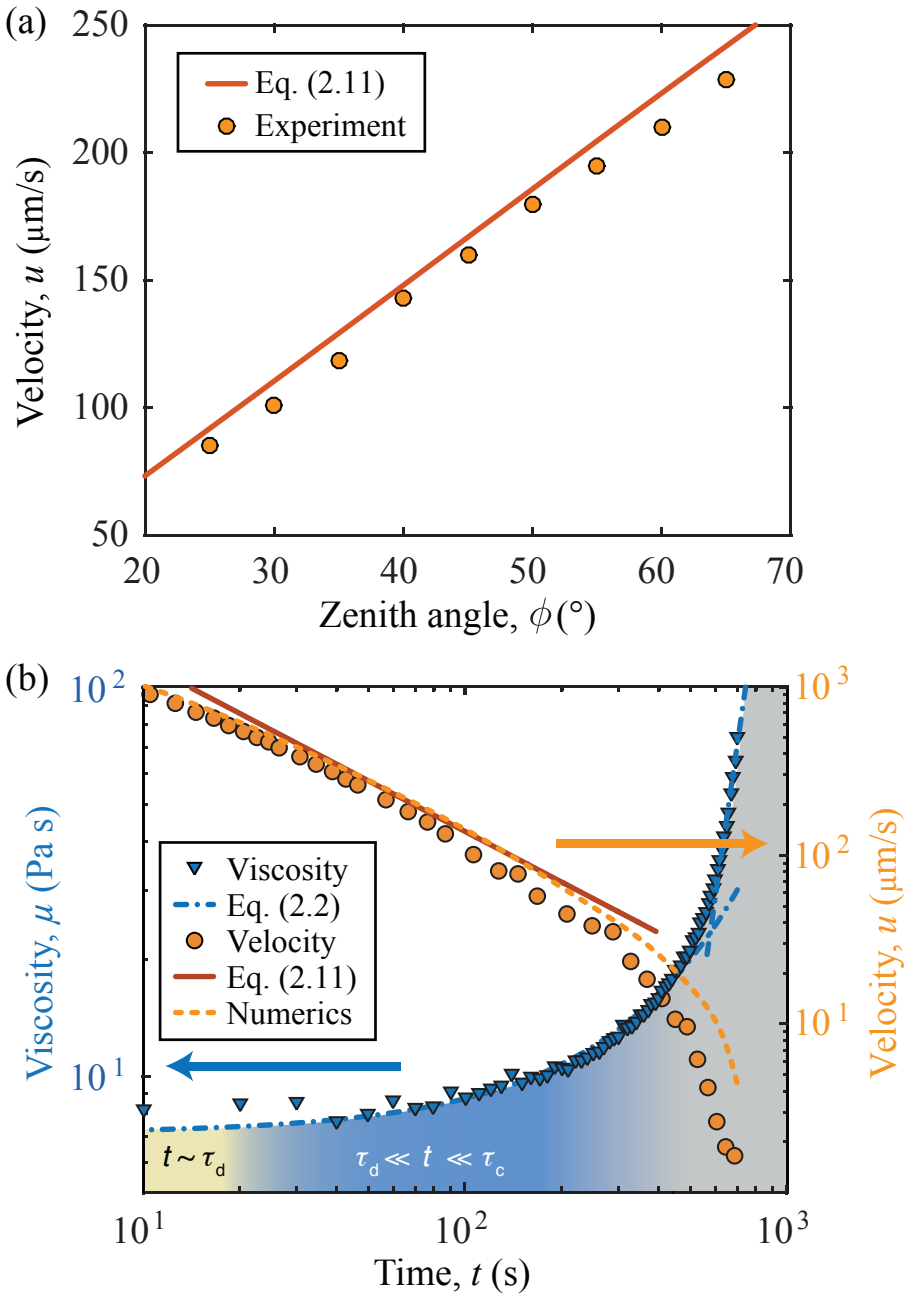

Figure 2-5: **Spatial and temporal variation of the flow velocity.** (a) The instantaneous local velocity, $u(\phi, t = 60\,\text{s})$ versus ϕ. (b) Time variation of the velocity, $u(\phi = 60°, t)$ orange circles, and the viscosity, $\mu(t)$ blue triangles, of VPS-32. The dash-dot line is the best fit for the viscosity. The solid and dashed lines are the predictions from the model for the velocity field and direct numerical simulations, respectively.

the initial drainage time, $\tau_\mathrm{d} = \mu_0 R/(\rho g h_\mathrm{i}^2)$, where h_i is the initial average coating thickness. For example, in the representative case above for VPS-32, we find $\tau_\mathrm{d} = 5.9\,\mathrm{s} \simeq 0.01\,\tau_\mathrm{c}$ using $h_\mathrm{i} = 2\,\mathrm{mm}$, $R = 38\,\mathrm{mm}$, $\rho = 1160\,\mathrm{kg\ m^{-3}}$, $\mu_0 = 7.1\,\mathrm{Pa\ s}$ and $\tau_\mathrm{c} = 574\,\mathrm{s}$. A direct consequence of this separation of timescales is that there is a loss of memory in the process, such that h_f should be independent of h_i. This prediction will be thoroughly examined in Sec. 2.8 by varying the height of poring and the volume of poured polymer.

Returning to the time evolution of u and μ in Fig. 2-5(b), at early times ($t < \tau_\mathrm{d}$) there are some disturbances due to initial conditions and we do not attempt to describe this regime. During intermediate times ($\tau_\mathrm{d} \ll t \ll \tau_\mathrm{c}$), μ is approximately constant, and the velocity is set by viscous drainage with $u \sim 1/t$ (Takagi & Huppert, 2010). For $t > \tau_\mathrm{c}$, as the curing of the polymer accelerates, μ sharply increases with time, and consequently, the flow velocity dramatically slows down.

The separation of the drainage and curing timescales can be leveraged further to tune the final thickness of the shell. Since h_f is determined by the interplay between the drainage timescale and curing timescale, τ_c, the final thickness can be increased by accelerating the curing process. One strategy to achieve this would be to alter τ_c by modifying the kinetics of cross-linking (*e.g.*, through additives or temperature), which would also modify the viscosity of the thin film or the elastic modulus of the final shell. An alternative is to shift the origin of the process by waiting time, τ_w, between the preparation of the polymer and the moment when the polymer solution is poured onto the mold. This waiting procedure offers an additional lever in tuning the properties of the fabricated shells.

Having presented our robust and versatile mechanism to fabricate thin elastic shells by the coating and subsequent curing of a polymer film, we proceed by rationalizing this process through a theoretical framework that is able to predict the final shell thickness, h_f.

2.5 Theoretical model with time-varying viscosity

In this section, we first introduce an existing model that predicts the thickness of the liquid film as a function of time. Then, we develop a model that is able to predict the final shell thickness at the pole of a sphere by combining the time-varying viscosity and the lubrication equations. It should be noted that the generalized solution that accounts for the spatial variation of the film was obtained by our collaborators, Pierre-Thomas Brun, Gioele Balestra, and François Gallaire, and will be described in Sec. 2.6.1.

2.5.1 Lubrication equation for a liquid film draining on a spherical surface

For the analytical description of the lubrication flow, we consider a hemisphere of radius, R, initially coated with a fluid of initial average thickness, h_i. Note that $h(\phi, 0)$ may vary spatially. Taking advantage of axisymmetry, we derive the model in a zenith coordinate system as shown in the schematic of Fig. 2-4(a). By assuming $h_\mathrm{i} \ll R$ and considering mass conservation, the flow velocity, $\mathbf{u} = (u, v)$, can be regarded to be essentially one-dimensional and predominantly tangential to the surface of the sphere in the ϕ direction. The velocity normal to the interface is $v \sim uh/R \ll u$. Under low Reynolds number conditions, the lubrication equations (Leal, 2007) for this flow yield the following nonlinear partial differential equation:

$$h_t = -\frac{1}{3\mu R \sin\phi}\Bigg[h^3 \sin\phi\Bigg\{\frac{\gamma}{R}\Big(h_{\phi\phi\phi} + 2h_\phi + h_{\phi\phi}\cot\phi - h_\phi \csc^2\phi\Big) + \rho g\Big(-\frac{h_\phi \cos\phi}{R} + \sin\phi\Big)\Bigg\}\Bigg]_\phi, \tag{2.3}$$

where the subscripts denote differentiation with respect to time and zenith angle, *i.e.* $\partial/\partial t$ and $\partial/\partial\phi$, respectively. Furthermore, under the assumptions that the thickness of the fluid film varies slowly along ϕ and that the effects of surface tension are

negligible, Eq. (2.3) can be simplified to (Takagi & Huppert, 2010)

$$h_t + \frac{\rho g}{3\mu R \sin\phi}\left(h^3 \sin^2\phi\right)_\phi = 0. \tag{2.4}$$

Under the above conditions, the flow is primarily governed by viscous forces and the component of gravity along the flow such that the drainage time, τ_d, is the relevant time scale of the problem. At the pole ($\phi = 0$), the thickness varies according to the well established drainage law, $h_0(t) = h_\mathrm{i}(1 + \frac{4}{3}t/\tau_\mathrm{d})^{-1/2}$ (Takagi & Huppert, 2010; Trinh et al., 2014), which we generalize further in our problem, in the context of time-varying viscosities, $\mu(t)$.

2.5.2 Including the effects of curing into the flow solution

In order to obtain the prediction for the final film thickness, we need to take into account the time-varying viscosity, $\mu(t)$, of the polymer solution while solving Eq. (2.4). At the pole ($\phi = 0$), due to the symmetry $\partial h/\partial\phi = 0$, Eq. (2.4) is simplified to

$$h_t + \frac{2\rho g h^3}{3\mu(t) R} = 0 \tag{2.5}$$

combined with $\mu(t)$. Solving this ordinary differential equation yields the film thickness at the pole during the curing regime as

$$h_0(t) = \frac{h_i}{\sqrt{1 + \frac{4\rho g h_i^2}{3R}\int_0^t \frac{1}{\mu(t')}dt'}}. \tag{2.6}$$

At times that are much larger than the initial drainage time ($t \gg \tau_\mathrm{d}$), the above equation can be simplified to

$$h_0(t) \approx \sqrt{\frac{3R}{4\rho g \int_0^t \frac{1}{\mu(t')}dt'}}, \tag{2.7}$$

such that it becomes independent of the initial thickness. Substituting the piecewise functions of the viscosity (Eq. (2.2)) and in the limit of $t \to \infty$, we obtain the following

prediction for the final thickness,

$$h_{0,\mathrm{f}} \approx \sqrt{\frac{3\mu_0 R}{4\rho g}\frac{1}{K}} \tag{2.8}$$

with $K = \{(k - e^{-\beta\tau_c})/\beta\} + \{\tau_c e^{-\beta\tau_c}/(\alpha - 1)\}$, where $k = 1$ when there is no delay between the preparation and the coating with the polymer solution. In Sec. 2.9, we will introduce a technique to tune the thickness of the shell by delaying the moment of pouring of the polymer solution.

In Fig. 2-6, we plot the final thickness of the shells, h_f, versus the radius, R, for the representative case of VPS-32 obtained from experiments (circles), theoretical prediction (solid line) from Eq. (2.8), and numerics (dashed line). All numerical simulations in this chapter were conducted through a collaboration with Gioele Balestra

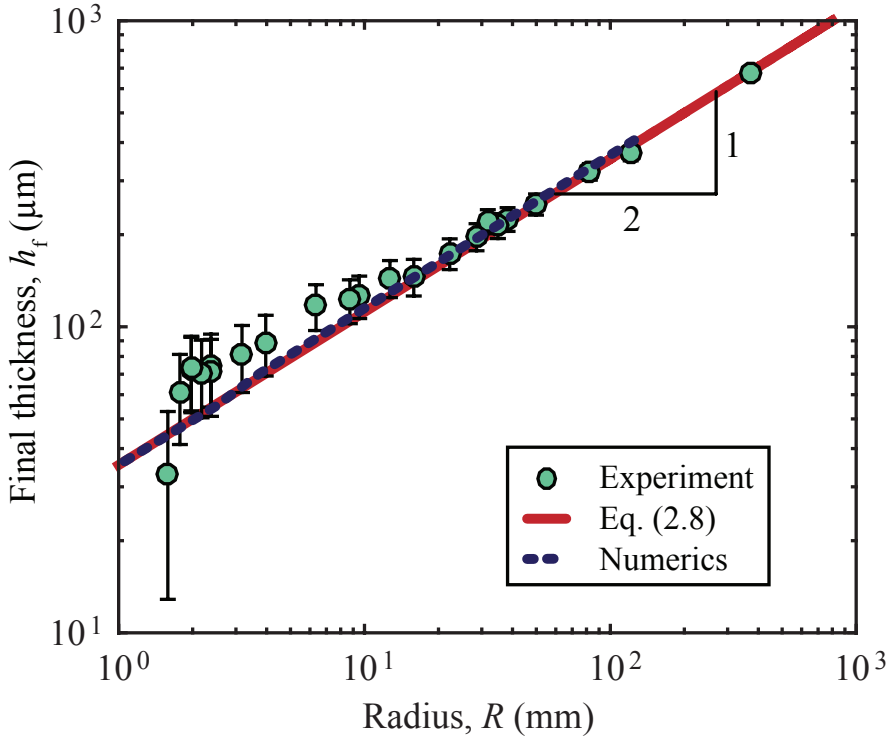

Figure 2-6: **Final thickness of shells made with VPS-32.** Comparison between theory, numerics and experiments for the dependence of h_f on R, for the representative case of VPS-32. The results are consistent with the power law $h_\mathrm{f} \sim R^{1/2}$ and in agreement with Eqs.(2.1) and (2.8).

and François Gallaire. The experimental results (circles) are consistent with the power law $h_f \sim R^{1/2}$ and, also, in good agreement with both the theory (solid line) and numerics (dashed line). It is important to note that our model has no adjustable parameters. All numerical coefficients (α, β and τ_c) are independently determined once and for all from the viscosity profile and then plugged into the theory.

2.6 Profiles of the liquid film and final shell thickness

The variation of the thickness from the pole to the equator of the hemispherical shells was found to be at most 6.6% (VPS) and 8.7% (PDMS) for each shell. These values were obtained from the experiments using standard deviations of the shell thicknesses along one of its meridians. In this section, we describe the nonlinear drainage flow solution, which is able to predict the spatial variation of the film thickness during the drainage and the final shell thickness. The thickness profiles measured through experiments are then compared with the theoretical prediction, yielding good agreement when PDMS was used and moderate agreement for VPS (yet having a smaller standard deviation than PDMS shell has). Various factors that affect the spatial uniformity of the shell thickness will be discussed in the following section.

2.6.1 Nonlinear drainage flow solution

The generalized solution accounting for the spatial variation in ϕ of the film was obtained in collaboration with Pierre-Thomas Brun, Gioele Balestra, and François Gallaire. A nonlinear expansion of the form $h(\phi, t) = h_0(t) + \phi^2 h_2(t)$ was performed on the lubrication equations (Takagi & Huppert, 2010) that describe our axisymmetric flow on a hemispherical substrate to obtain

$$h(\phi, t) = h_0(t) \left[1 + \frac{\phi^2}{10} \left(1 + c \left(1 + \frac{4}{3} \frac{t}{\tau_d} \right)^{-5/2} \right) \right], \tag{2.9}$$

where c is a numerical factor that depends on the initial condition (*e.g.*, $c = -1$ if the initial thickness profile is uniform). In the limit of $t \gg \tau_\mathrm{d}$, Eq. (2.9) simplifies to

$$h(\phi, t) \approx \sqrt{\frac{3\mu_0 R}{4\rho g t}} \left(1 + \frac{\phi^2}{10}\right). \tag{2.10}$$

The memory loss of the flow mentioned earlier arising from the separation of the drainage and curing timescales is well captured by this description, given that h_i is absent from Eq. (2.10). Moreover, there is a weak dependence on ϕ (7.0% standard deviation); a general result that has also been observed in the thinning of an air bubble formed in a fluid bath (Lhuissier & Villermaux, 2012), as well as in the thin air layer that supports a drop bouncing on a fluid interface (Couder et al., 2005).

As an indirect validation of Eq. (2.10), we substitute it into the free surface velocity equation describing the parabolic flow profile on a sphere, $u = \rho g h^2 \sin\phi/(2\mu_0)$ (Takagi & Huppert, 2010), to obtain

$$u(\phi, t) \approx \frac{3}{8}\frac{R}{t}\left(1 + \frac{\phi^2}{10}\right)^2 \sin\phi. \tag{2.11}$$

This prediction for the variation of u on both ϕ (at fixed t) and t (at fixed ϕ) is in agreement with the experimental velocity profiles shown in Fig. 2-5 for $\tau_\mathrm{d} \ll t \ll \tau_\mathrm{c}$, in the regime after the initial drainage, when the polymer viscosity is approximately constant, and prior to curing. In particular, u is found to be almost linear in ϕ as the cubic term of the Taylor expansion is $\phi^3/30$, which is much smaller than the conventional cubic term, $\phi^3/6$, of the Taylor series of the $\sin\phi$. Strikingly, the velocity field in this regime is independent of both gravity and viscosity and is solely set by the geometry of the problem, so that no material parameters enter the prediction.

For predicting the final thickness profile, the time-varying viscosity is combined with Eq. (2.10), following the same procedure described in Sec. 2.5.2.

$$h_\mathrm{f}(\phi) \approx \sqrt{\frac{3\mu_0 R}{4\rho g}\frac{1}{K}} \left(1 + \frac{\phi^2}{10}\right) \tag{2.12}$$

2.6.2 Shear thinning effects

We plot the shell thickness profiles as a function of the zenith angle, ϕ, in Fig. 2-7. As a representative case, Fig. 2-7(a) shows the final thickness of a shell fabricated by pouring PDMS on the outside of a sphere with $R = 38$ mm, and Fig. 2-7(b) presents the final thickness of shells fabricated by pouring VPS-32 either on the outside or the underside of a hemisphere with $R = 25$ mm. The experimentally obtained thickness of PDMS shell (circles) is almost constant in the vicinity of the pole and gradually increases with ϕ. The error bars of the data for h_{f} (y-axis) correspond to the standard deviation on multiple measurements. The error bars of the data for ϕ (x-axis) correspond to the size of the angular range used to bin the data. The experimental results are well described by Eq. (2.12) (solid line) without any adjustable parameters. This agreement validates the variation of theoretical model that also takes into account the time-varying viscosity of the polymer and the spatial variation of the film thickness. For VPS-32, however, the thickness is slightly larger in the vicinity of the pole than in the remainder of a shell. This is because of the shear thinning of VPS that leads to an increase of the thickness at the apex where the viscosity is largest. These effects are not captured by our model, yet they do not prevent the shell from being uniform within 6.6% variations. From the data in Fig 2-7(b), we learn that coating the outside (stars) or the underside (crosses) of the hemispherical surface results in almost the same thickness profiles.

In Fig. 2-8, the shear thinning behavior of VPS and the Newtonian behavior of PDMS are presented. In Fig. 2-8(a), we plot the viscosity of VPS-32 as a function of time at the following (constant) values of shear rate: $\dot{\gamma} = \{0.05, 0.1, 0.25, 0.5\}$ s^{-1}. The viscosity is higher when the shear rate is lower. Therefore, during the coating process, the viscosity is largest at the apex where the flow velocity and shear rate are zero. In Fig. 2-8(b), we plot the viscosity of PDMS versus the shear rate at 20°C, when the effects of curing are negligible, and find that the viscosity is independent of the shear rate. Unlike VPS that is a shear-thinning liquid, PDMS has a constant viscosity in the range of shear rates, $0.01 < \dot{\gamma}$ [s^{-1}] ≤ 10, that are relevant to the

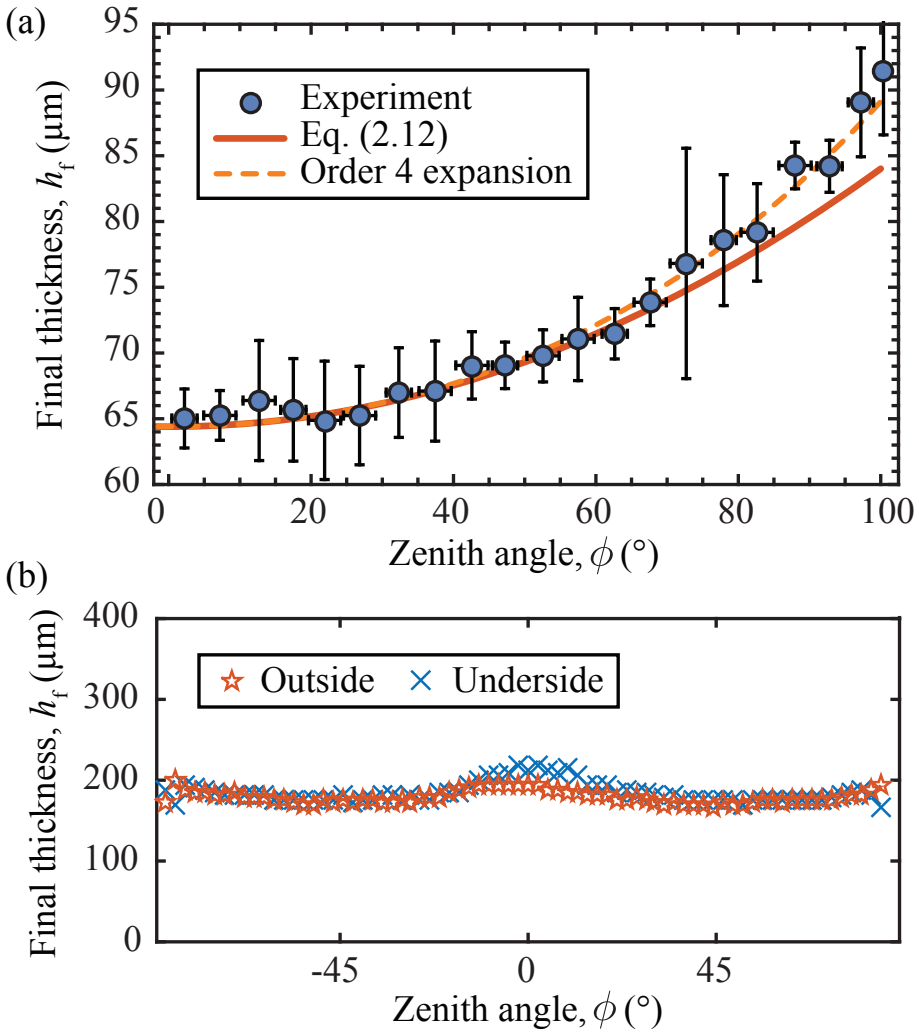

Figure 2-7: **Final shell thickness profiles.** (a) Final thickness of a shell fabricated by pouring PDMS on the outside of a hemisphere with $R = 38$ mm compared to Eq. (2.12); solid line. The dashed line is the prediction obtained by refining the expansion to the next order (Lee et al., 2016a). The error bars of the data for h_f (y-axis) correspond to the standard deviation on multiple measurements. The error bars of the data for ϕ (x-axis) correspond to the size of the angular range used to bin the data. (b) Final thickness of shells fabricated by pouring VPS-32 on the outside or the underside of a hemisphere with $R = 25$ mm.

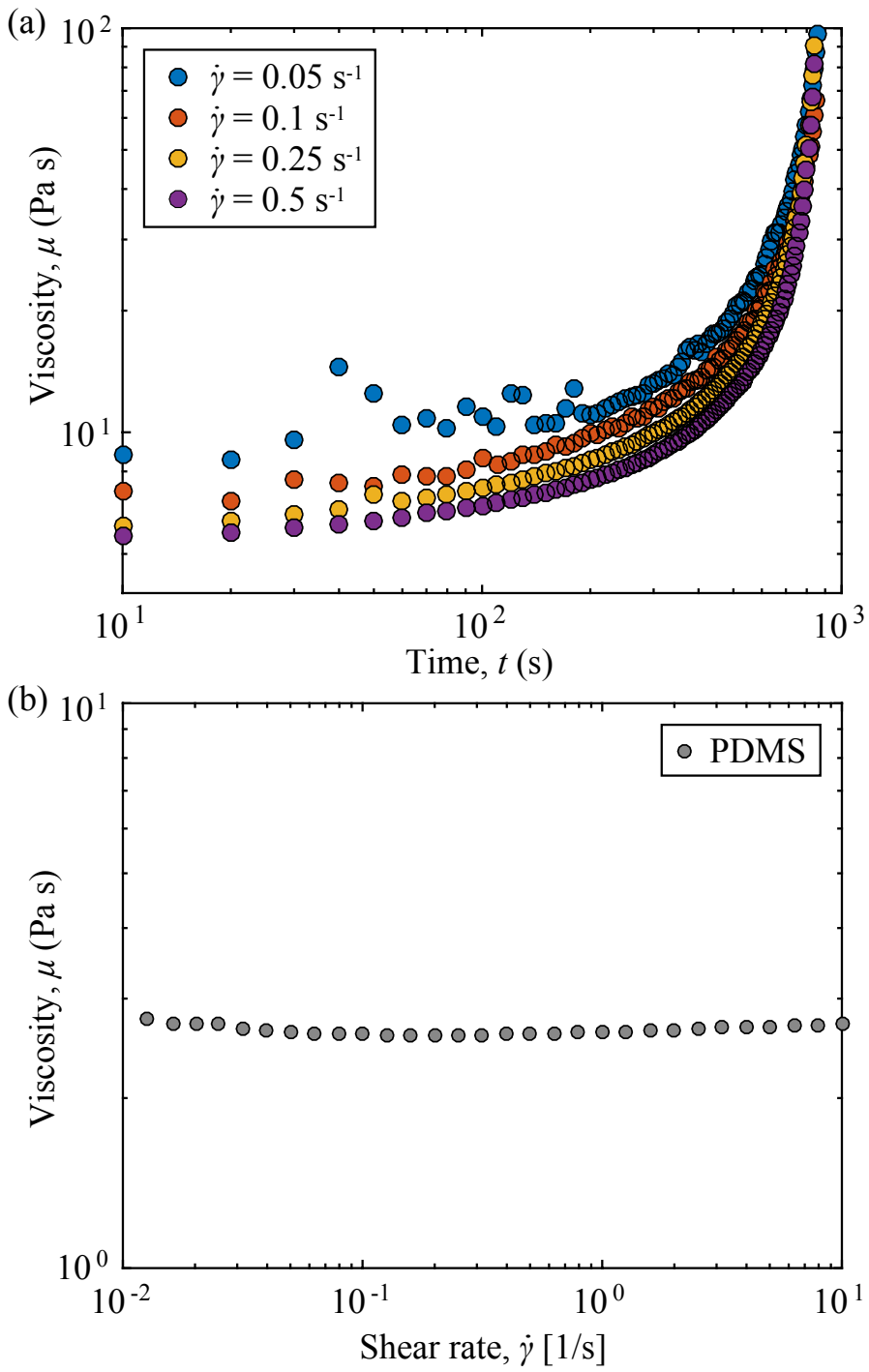

Figure 2-8: **Rheology with different shear rates.** (a) Time dependence of the viscosity of VPS-32 with different constant shear rates. The parameters α ($\pm 7\%$), β ($\pm 7\%$), and τ_c ($\pm 4\%$) do not vary much for different shear rates. Only μ_0 varies significantly with different shear rates: $\mu_0 = \{8.6, 7.1, 5.9, 5.6\}$ Pa.s with $\dot{\gamma} = \{0.05, 0.1, 0.25, 0.5\}$ s^{-1}, respectively. The results are indicative of shear thinning behavior. (b) The viscosity of PDMS (at 20°C) does not depend on the shear rate when below 10 s^{-1}. All data were measured over a period of 5 min when the effects of curing are still negligible.

coating process.

2.6.3 Estimation of the shear rate

Our model, namely Eqs. (2.8) and (2.12), uses physical parameters for the rheology of the polymer. However, we commented above that VPS exhibited shear thinning, while PDMS was found to behave as a Newtonian fluid for small shear rates. We show, in Fig. 2-8(a), four different time evolution of the viscosity of VPS-32 depending on the shear rate, $\dot{\gamma} = \{0.05, 0.1, 0.25, 0.5\}$ s^{-1}. An estimate of the relevant shear rate is therefore needed to measure the viscosity with the appropriate shear rate and use the viscosity profile in the theoretical model. We used the value $\dot{\gamma} = 0.1$ s^{-1}, assuming a uniform shear rate across the sample. In reality, $\dot{\gamma}$ varies from zero at the apex to its peak value at the equator and also depends on R and t. However, our choice for $\dot{\gamma}$ is representative of the applied shear rates over the hemisphere and leads to a good agreement between theory and experiments for most values of R and ϕ. We have analyzed the sensitivity of the predictions for h_{f} with respect to $\dot{\gamma}$ and found that it is small.

For the representative case (VPS-32 with $R = 38$ mm) shown in Fig. 2-9, the shear rate $\dot{\gamma} \approx u(\phi, t)/h(\phi, t)$ is a function of ϕ and t and has the average value of 0.13 s^{-1}, for the data within the time period, $\tau_{\mathrm{d}} < t < \tau_{\mathrm{c}}$ ($\tau_{\mathrm{d}} = 6$ s is the initial drainage time and $\tau_{\mathrm{c}} = 574$ s is the curing time) and over the full range of ϕ. This estimation was conducted using the rheology of VPS measured for $\dot{\gamma} = 0.1$ s^{-1}. Since both of these values (the estimated value and the modeled averaged value) are approximately the same, this choice for the shear rate was referred to as self-consistent.

We measured the viscosity of VPS-32 with different shear rates ranging from 0.05 (close to the limit of the resolution of our rheometer) to 0.5 s^{-1} and the results are shown in Fig. 2-8(a). The fitting parameters α ($\pm$7% maximum absolute deviation (MAD)), β ($\pm$7% MAD), and the curing time τ_{c} ($\pm$4% MAD) do not vary significantly for the explored shear rates. By contrast, the initial viscosity, μ_0, does vary in a more pronounced way, as $\mu_0 = \{8.6, 7.1, 5.9, 5.6\}$ Pa.s with $\dot{\gamma} = \{0.05, 0.1, 0.25, 0.5\}$ s^{-1}, respectively. This is indicative of non-Newtonian behavior. Nevertheless, this change

in the shear rate yields only moderate differences in the final thickness of the shell. We found the variations in thickness to be of ±10% (MAD) of the reference case ($\dot{\gamma} = 0.1$ s^{-1}), even though the shear rate is varied by up to 500% of the reference value. Therefore, the choice of a single shear rate of 0.1 s^{-1} does not compromise our results and removes an adjustable parameter from the problem.

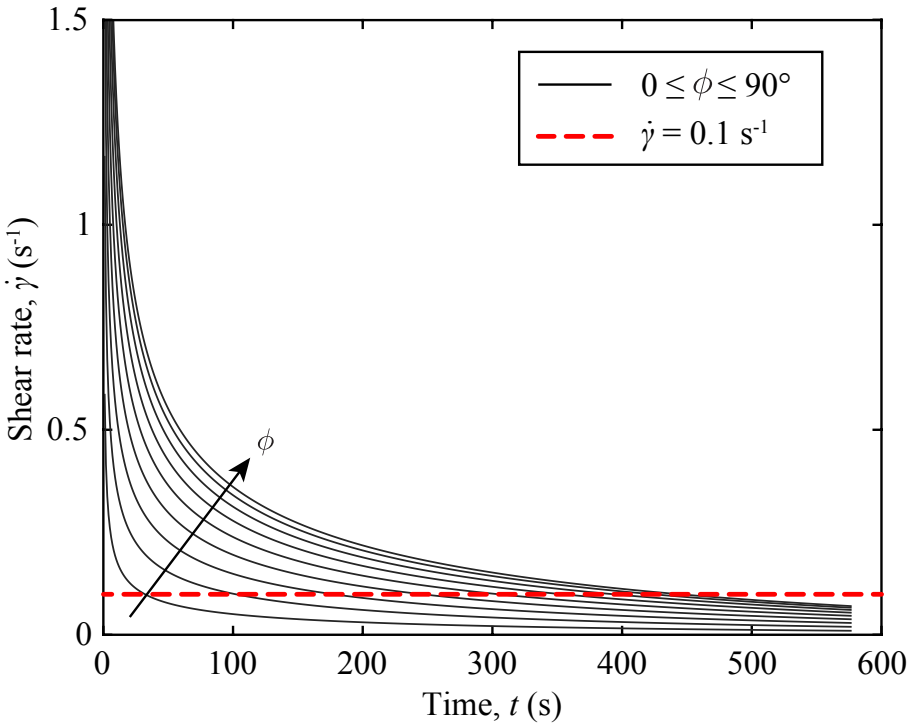

Figure 2-9: **Shear rate evolution at different locations.** Shear rate is estimated as $\dot{\gamma} \approx u(\phi, t)/h(\phi, t)$ from the model with the properties of VPS-32 and $R = 38$ mm. Within the time period, $\tau_d < t < \tau_c$ ($\tau_d = 6$ s is the initial drainage time and $\tau_c = 574$ s is the curing time) and over the full range of ϕ, the average value of these various curves is $\dot{\gamma} = 0.13$ s^{-1} and close to the value of $\dot{\gamma} = 0.1$ s^{-1} used in measurement of viscosity of polymer solutions.

2.7 Other factors that affect the shell thickness and its uniformity

2.7.1 Surface tension effects

The results presented above establish the basis for the rapid and robust coating process to fabricate thin spherical shells of nearly uniform thickness and with radii spanning over two orders of magnitudes ($1 \leq R\,[\text{mm}] \leq 375$). As the radius of the sphere is decreased below $R < 10$ mm, the agreement between our model and the experiments deteriorates due to the influence of the meniscus that connects the flow on the hemisphere to the puddle that forms as the fluid drains. This effect is not accounted for in our model, but we expect it to be negligible when $R \gg \ell_c$, where $\ell_c = \sqrt{\gamma/(\rho g)}$ is the capillary length that prescribes the relative magnitude of capillary and gravitational forces. Since $\ell_c \simeq 1.3$ mm and $\ell_c \simeq 1.4$ mm for VPS and PDMS, respectively, the deviations of the theory from the data for small R are consistent with the onset of these surface tension effects. In Fig. 2-6, the experimental results (circles) and the theory (solid line) are in excellent agreement when $R > 10\ell_c$ and deviate from each other for smaller radii ($R \sim \ell_c$). Note that the meniscus that connects the flow over the hemisphere to the 'puddle' that forms as the fluid drains resists the flow. Hence, the theory underpredicts the experimental results at this small scales. For smaller radii ($R \sim \ell_c$), we need to restore the surface tension terms that were neglected in our lubrication model in order to accurately predict the thickness of shells.

2.7.2 Instabilities of the fluid interface

When the polymer is poured on the underside of a mold, the curvature can suppress the Rayleigh-Taylor instability and thereby prevent the formation of dripping droplets (Trinh et al., 2014). Therefore, the uniformity bounds of the shell that were just stated are ensured, as long as the modified Bond number $B = \rho g R h_i/\gamma$ (which characterizes the relative importance of gravity and surface tension, γ) remains

smaller than the critical value, $B < B_c = 8$ (Trinh et al., 2014). In Fig. 2-10(a), we provide examples of the Rayleigh-Taylor instability. Trinh et al. (2014) investigated the dynamics of a thin liquid film on the underside of a curved cylindrical substrate. The experimental image in Fig. 2-10(a1) is the side view when the Bond number exceeded the critical value, $8 < B < 80$, where small droplets formed on the free surface, and Fig. 2-10(a2) is an image when the Bond number was even larger, $80 < B$, where drops pinched off from the free surface. In our experiments, we could not observe the Rayleigh-Taylor instability.

On the other hand, when the outside of a mold is used, fingering instabilities can occur at the advancing front of the flow, but this can be precluded by pouring a sufficiently large volume of liquid over the surface (Takagi & Huppert, 2010). A critical volume can be derived following the study conducted by Takagi & Huppert (2010), and we estimated that it is of the order of 1 mL for a hemisphere of radius $R = 20$ mm. Under these conditions, pouring on the underside or outside of complementary molds yields identical shells of the same uniform thickness, h_f. An experimental image is shown in Fig. 2-10(b), where VPS-22 was poured on the sphere with $R = 121$ mm

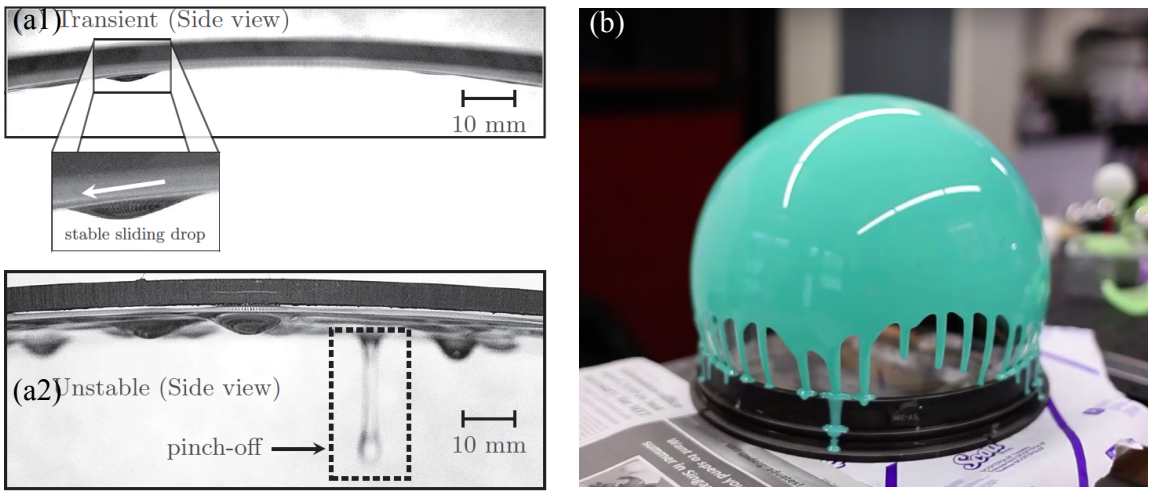

Figure 2-10: **Instabilities of the fluid interface on curved substrates.** (a) Rayleigh-Taylor instability on the underside of a curved cylindrical substrate when (a1) $8 < B < 80$ and (a2) $80 < B$. Adopted from (Trinh et al., 2014). (b) Fingering instability on the outside of a spherical substrate. VPS-22 was poured on the sphere with $R = 121$ mm.

and fingering instability occurs at the advancing front of the flow below the equator of the sphere. Note that during this process, approximately $\approx 90\%$ of the volume drains out of the hemisphere. Even if the technique that we have introduced is an excellent rapid-prototyping method, it may not be suitable for large scale industrial applications, due to this large 'waste' of material. With that said, similar limitations are found for spin-coating, a technique that is widespread across both industry and research.

2.8 Robustness and insensitivity of the final shell thickness to the initial conditions

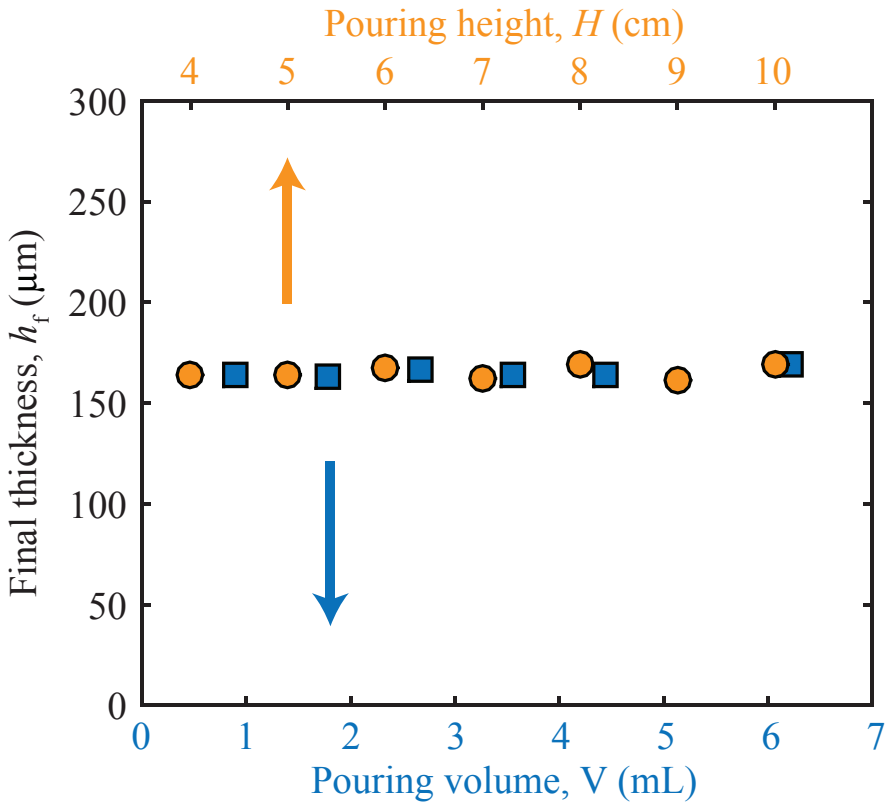

Figure 2-11: **Robustness of the coating mechanism.** Final shell thickness, h_f obtained with different pouring conditions: pouring height, H, and volume, V, poured onto a spherical mold with $R = 20$ mm using VPS-32.

The physical principles that underlay the dynamics of the coating process have been rationalized by our analytical model presented above, to which the separation between the initial drainage and curing timescales is key. Drainage occurs significantly faster than the polymer curing, such that the memory of the flow vanishes before it is arrested by cross-linking to yield the final elastic shell. Consequently, geometry prevails, and the curvature of the mold together with the rheology of the polymer set both the dynamics of the flow and the final thickness of the shell ($h_\mathrm{f} \sim R^{1/2}$).

The robustness of this mechanism and its insensitivity to the initial conditions are now corroborated by experiments and simulations. We measured the thickness of shells fabricated by pouring VPS-32 on a spherical mold with $R = 20$ mm obtained for different values of the height from which the polymer is poured onto the mold ($4 \leq H\,[\mathrm{cm}] \leq 10$), as well as the volume poured ($0.9 \leq V\,[\mathrm{mL}] \leq 6.3$). In Fig. 2-11, we plot the thickness versus H (circles) or V (rectangles) and find that h_f is constant to within 5.6% (MAD) across these various pouring conditions.

Furthermore, the memory loss of flow was investigated using both the theoretical model and the simulations. In Fig. 2-12(a), the time-series of the normalized film thickness profiles with a constant viscosity are plotted versus the zenith angle, ϕ. Solid lines are the theoretical prediction with uniform initial thickness profile, $h(\phi, t = 0)/h_\mathrm{i} = 1$, and dashed lines correspond to the numerically computed evolution of an initially sinusoidal thickness profile of the form $h(\phi, t = 0)/h_\mathrm{i} = 1 + 0.375\cos(10\phi)$. We used the average initial thickness of film $h_\mathrm{i} = 0.2$ mm, the radius of sphere $R = 20$ mm, and the material properties of VPS-32. The initially sinusoidal thickness profile in numerics is flattened at the early time ($t/\tau_\mathrm{d} = 5$) and agreement with the theoretical prediction improves with time. In Fig. 2-12(b), simulations that were initiated with four significantly different initial fluid distributions – uniform (solid line), sinusoidal (dashed-dotted line), as well as tapered profiles towards the pole (dashed line) and the equator (dotted line) – converge to the same final shell thickness (thick solid line), which agrees well with the prediction from Eq. (2.12) (black dashed line).

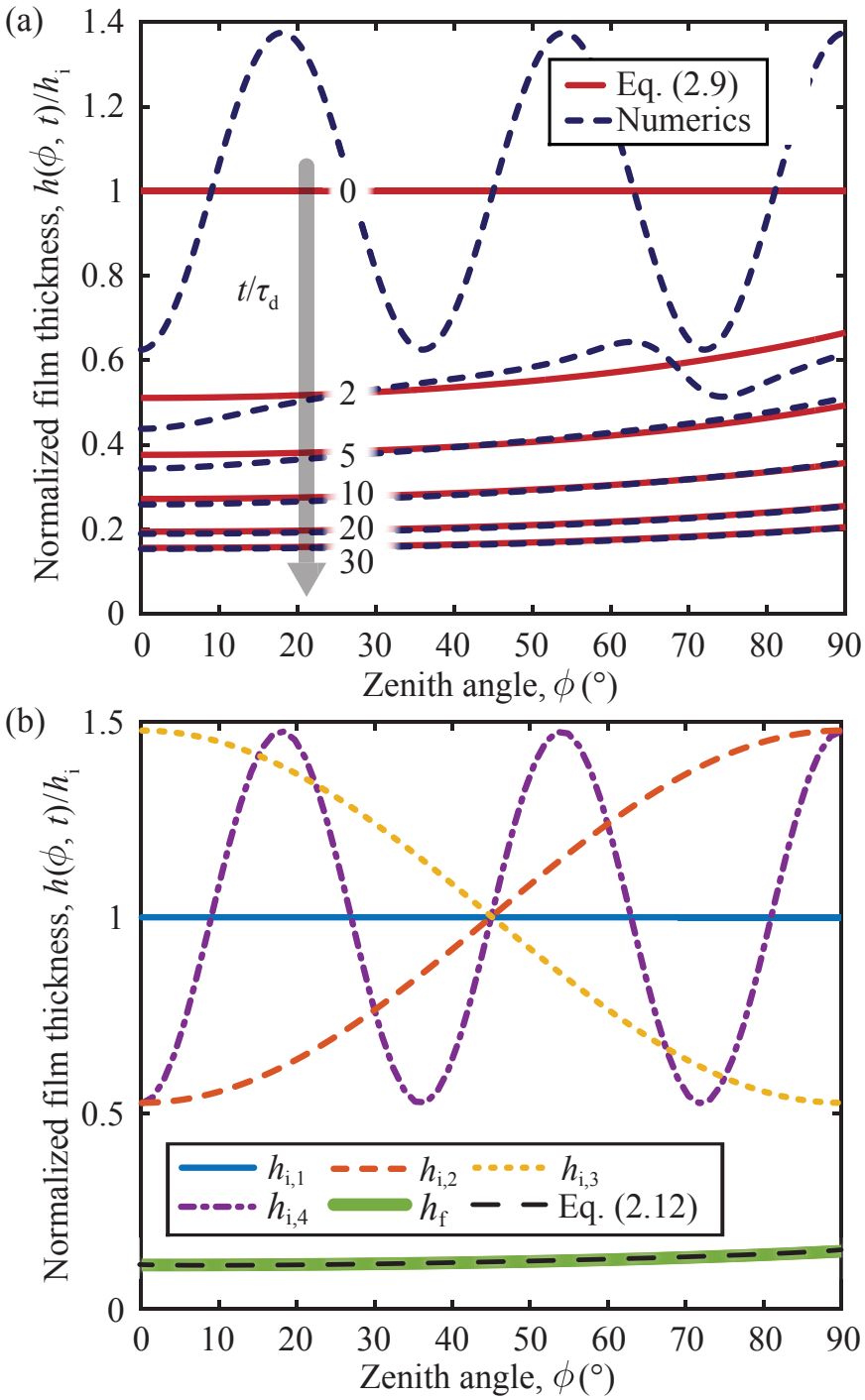

Figure 2-12: **Insensitivity to the initial conditions.** (a) Time-series of the normalized film thickness profiles, $h(\phi, t)/h_i$, with a constant viscosity, at t/τ_d =0, 2, 5, 10, 20, and 30. Dashed lines correspond to the numerically computed evolution of an initially sinusoidal thickness profile. Solid lines are the theoretical prediction with uniform initial thickness profile. The various parameters are: $h_i = 0.2$ mm, $R = 20$ mm, and the material properties of VPS-32. (b) Four different initial thickness profiles used in the numerics versus the zenith angle which are combined to one curve at the final.

2.9 Tuning the final thickness

Since the final shell thickness, h_{f}, is directly connected to the curing time, this thickness can be continuously tuned by waiting a time τ_{w} between the preparation of the polymer mixture and the instant when it is poured onto the mold. In Fig 2-13, we plot the normalized film thickness, $h_{\mathrm{f}}/h_{\mathrm{f},0}$ (where $h_{\mathrm{f},0}$ is the value of the final thickness when $\tau_{\mathrm{w}} = 0$) as a function of the waiting time, τ_{w}, normalized by the curing time, τ_{c}. We find that h_{f} can be increased by as much as 60% for VPS-22 and 32, sixfold for VPS-8 and elevenfold for PDMS. Substituting $e^{-\beta\tau_{\mathrm{w}}}$ for k in Eq. (2.8) allows for a direct comparison to the experimental result, with a favorable agreement in the case of VPS-22 and 32. For the VPS-8 and PDMS, however, an additional adjustment to our framework is required since we found that its rheology differs if the curing occurred in a quiescent state (*e.g.*, when waiting in bulk for τ_{w} before pouring) versus when sheared as during coating.

For the representative case of PDMS, rheometry measurements were performed where the values of τ_{w} were systematically varied, and the viscosity evolutions are plotted as a function of time in Fig. 2-14(a). The viscosity was measured after holding the PDMS mixture for a time $\tau_{\mathrm{w}} = \{0, 10, 20, 30\}$ min in a quiescent state prior to testing in the rheometer. If the rheology is constant, whether in a quiescent state or when sheared, the viscosity curves would collapse when the time axis for each test is shifted by τ_{w}. However, we plot the viscosity versus the sum of the measuring time and the effective waiting time, $t + \delta\tau_{\mathrm{w}}$, in Fig. 2-14(b), and find that all of the data collapse onto the master curve obtained for $\tau_{\mathrm{w}} = 0$ when the time axis for each of tests is shifted by $\delta\tau_{\mathrm{w}}$ (the constant factor $\delta = 2.02 \pm 0.02$ was determined by fitting). We have therefore concluded empirically that PDMS cures δ times faster when quiescent compared to under shear, but we have not been able to find this specific result in the literature. We speculate that the shifting factor required for collapse will likely depend on the shear rate and the specifics of the polymer. With this additional information at hand, substituting $e^{-\beta\delta\tau_{\mathrm{w}}}$ for k in Eq. (2.8) accounts for the effective waiting time, and yields a prediction for h_{f} (dashed lines) that is in agreement with

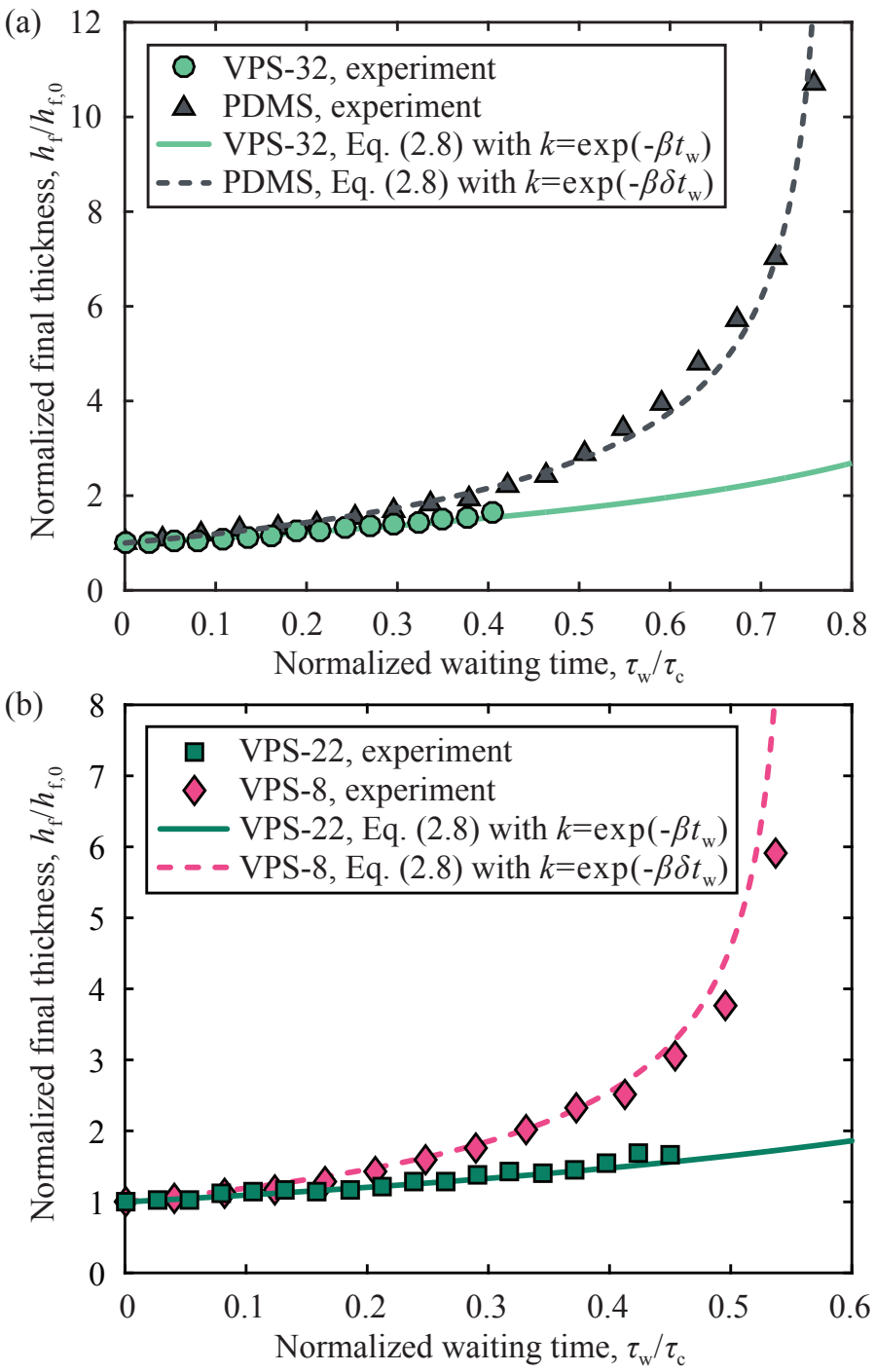

Figure 2-13: **Varying the shell thickness by delaying pouring.** The normalized shell thickness by its value when $\tau_w = 0$ can be tuned by delaying the pouring time by τ_w from the moment of preparation of the polymer solution. (a) Results for both VPS-32 (circle) and PDMS (triangle) are shown. Solid and dashed lines are prediction for VPS-32 and PDMS, respectively. (b) Experimental results for VPS-8 (diamond) and 22 (rectangle) and predictions for VPS-8 (dashed line) and 22 (solid line). The shift factor of VPS-8 is $\delta = 2.1 \pm 0.1$.

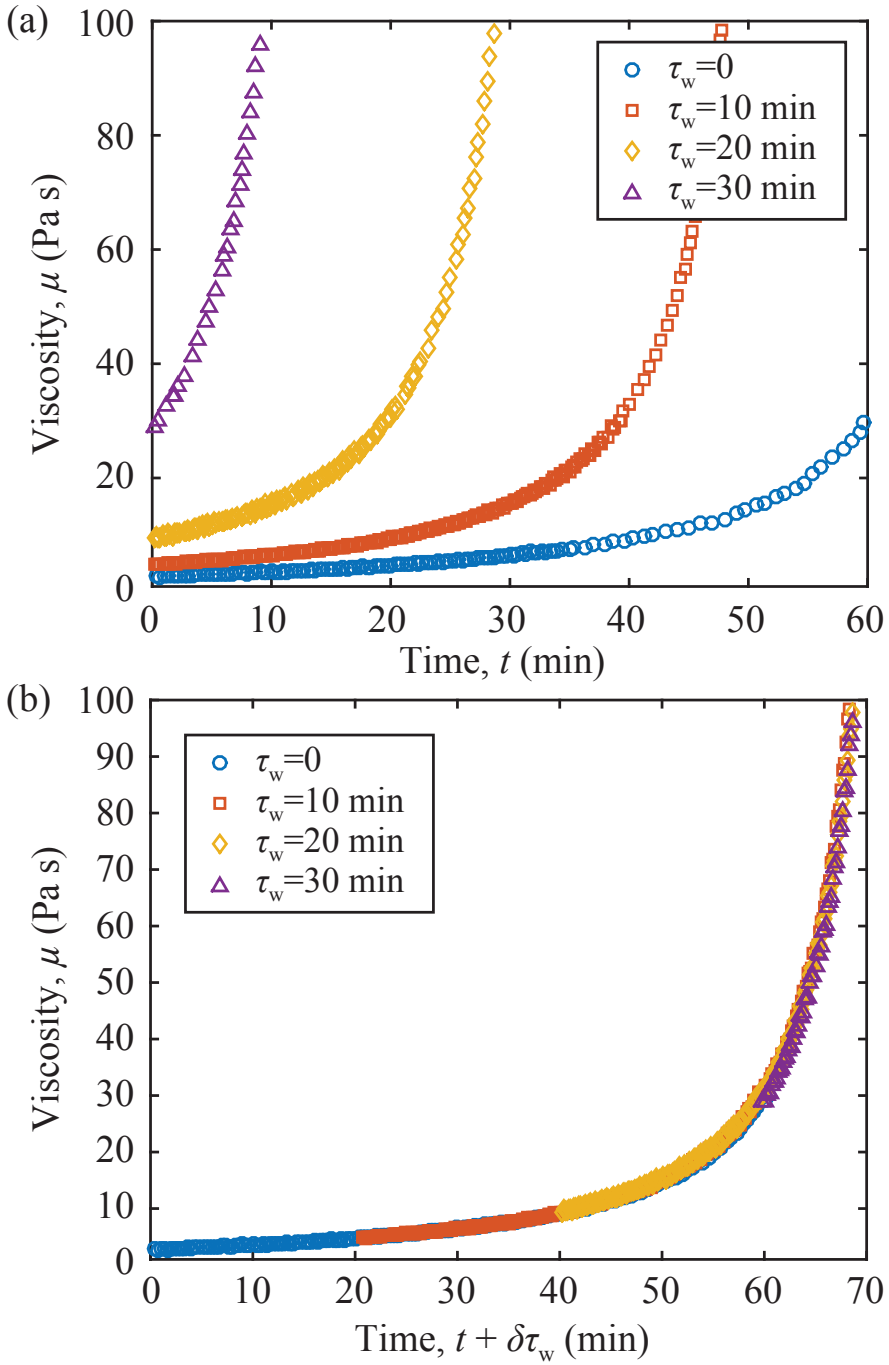

Figure 2-14: **Viscosity of PDMS as a function of time with different waiting time.** (a) Viscosity as measured after holding the mixture for a time τ_w in a quiescent state prior to testing in the rheometer. (b) Viscosity versus the sum of the measuring time, t, and the effective waiting time, $\delta\tau_w$ ($\delta = 2.02 \pm 0.02$ from fitting all the curves to the master curve obtained for $\tau_w = 0$).

the experimental data for VPS-8 (diamonds) and PDMS (triangles) in Fig. 2-13.

Our model is, therefore, able to accurately capture the elevenfold continuous variation of the shell thickness obtained when pouring partially cured polymer solutions. We did not have to consider δ for VPS-22 and 32 because the entire bulk of these more viscous polymer solutions are experiencing sustained shear while they were sequentially poured onto a series of identical molds. It is important to note that our theoretical description is only applicable if $\tau_w < \tau_c$.

For low viscosity polymer solutions (PDMS and VPS-8) the shift factor δ is needed to predict the final thickness. We speculate that, when waiting in bulk in a container, the boundary layers are thin compared to the size of the container due to the low viscosity of these polymers. Consequently, the majority of the polymer solution is not disturbed by the movement of the container, which is therefore in a quiescent state until τ_w. On the other hand, the higher viscosity of VPS-32 and 22, results in the diffusion of shear in the entire bulk of the solution during the waiting time, τ_w, while the bulk of the polymer solution is sequentially and continuously poured onto a series of identical molds. Thus, the theoretical model without a shift factor agrees well with the experimental results of VPS-32 and 22, but δ is finite for the other polymers.

2.10 Summary and outlook

In summary, we have shown that coating hemispherical molds with a polymer solution yields thin uniform shells whose thickness can be accurately predicted. Moreover, the final shell thickness can be tuned by modifying the time between polymer preparation and the moment of pouring. The resulting shells are a realization of the drainage dynamics, driven by gravity, slowed down by viscous stresses and eventually arrested by the curing of the polymer. The robustness and flexibility of this mechanism are inherent consequences of the loss of memory in the flow field.

The generality of this framework should open the door for future studies to fabricate slender solid structures in a variety of other geometries. A particularly interesting case outside the scope of the current study is the coating of ellipsoidal molds (Vaziri

& Mahadevan, 2008), with two distinct principal curvatures, where the difference between the pouring direction and the orientation of the surface could also play a role.

Furthermore, our fabrication technique could be important in the ongoing revival of the mechanics of thin elastic shells, in particular since it enables fully elastic structures that can reversibly explore strong geometric nonlinearities in their post-buckling regime (Audoly & Pomeau, 2010; Vaziri & Mahadevan, 2008; Katifori et al., 2010; Lazarus et al., 2012; Terwagne et al., 2014; Stoop et al., 2015; Nasto & Reis, 2014; Vella et al., 2015; Bende et al., 2015; Reis, 2015).

In the following chapters, the coating technique will be applied directly or with modifications, to fabricate thin elastic shells, which will be used to study the sensitivity of buckling to imperfections. The shells that we can manufacture are fully elastic and have a nearly constant thickness. These shells are therefore ideal to be used in buckling experiments. In Chapters 3 and 4, we also take advantage of the flexibility of our fabrication technique to finely tune the thickness and, therefore, produce shells in a range of thicknesses with a single mold. Moreover, an elastic shell fabricated with the above technique can itself be used as a mold to fabricate another shell. Thus, by deforming and then holding an elastic mold while polymer solution cures on the underside of the deformed mold, we can fabricate stress-free and geometrically imperfect spherical shells. In Chapter 3, we will use this precisely imperfect shell to find a relationship between the geometric imperfection and the critical buckling pressure.

Chapter 3

Defect-controlled buckling of pressurized spherical elastic shells

In this chapter, we combine experiments and numerical analysis to revisit the buckling of spherical elastic shells under uniform pressure loading, with an emphasis on determining the geometric role of precisely engineered imperfections on the buckling pressure. First, we build up on the work from Chapter 2 to develop a novel fabrication method of thin elastic shells containing a single 'dimple-like' defect of known geometry and measure their critical buckling pressure (Sec. 3.2). Finite element method (FEM) simulations are used to characterize the shape of the defects and analyze the buckling behavior of our imperfect shells (Sec. 3.3). Then, FEM results are found to be in excellent agreement with experiments (Sec. 3.4). Moreover, the FEM and experimental results are compared to a first order shell theory that was recently specialized to both perfect and imperfect spherical shells (Sec. 3.5). This theory yields a set of nonlinear ODEs that describes the mechanical response of our shells (Sec. 3.6). Remarkably good agreement is found across the triangle of experiments, FEM and ODE simulations for both the critical buckling pressure as a function of the amplitude of the imperfection, as well as the load-deformation behavior (Sec. 3.7). Finally, we find that beyond a critical defect amplitude, the buckling pressure becomes independent of the amplitude of the defect and quantitatively characterize this plateau (Sec. 3.8).

3.1 Motivation and literature review

For the research reported in this chapter, we were motivated by a lack of experimental studies relating a geometric imperfection and the critical buckling load of thin spherical shells. Furthermore, given that we had developed a technique to fabricate spherical elastic shells that can be used for buckling experiments, which was an ideal match for these attempts. In Chapter 2, we introduced a rapid, versatile and precise fabrication technique to manufacture thin elastic shells with controlled geometric and mechanical properties. As we described and explained in detail in the previous chapter, this technique involves the coating of hemispherical molds with a polymeric (elastomeric) solution, which, upon curing, produces an elastic shell of nearly uniform thickness. Elastomeric shells allow for the onset of buckling, as well as the large deformations, to occur at operating pressures that are significantly lower than that for metallic shells. Consequently, these lower values of the working pressures significantly reduce experimental complexity.

While thermoplastic shells can be produced through injection, rotational and blow molding, as pointed out in Chapter 1, these techniques are typically geared for industrial mass production and less suitable to a laboratory research setting, where reproducible, adaptable, and inexpensive prototyping tools are desirable. However, to make the experimental technique developed in Chapter 2 relevant to the study of imperfection sensitivity of pressurized shells, there is a need to adapt it so that the fabricated shells also contain one single precisely designed defect of known geometric properties. In this chapter, we develop a customizable rapid prototyping technique through which the geometry and magnitude of the defect can be designed and precisely fabricated. We experimentally investigate the effect of a dimple-like geometric imperfection on the critical buckling load of spherical elastic shells under pressure loading. Moreover, the experimental results are predicted through both finite element modeling and numerical solutions of a reduced shell theory.

The critical buckling load of a thin spherical shell under uniform external pressure is predicted by Eq. (1.1). However, for decades, this classical prediction was found

to be in disagreement with experimental results, which resulted in the knockdown factor, $\kappa_{\mathrm{d}} = p_{\max}/p_{\mathrm{c}}$, much lower than the unity, as shown in Fig. 1-2. It is now well recognized that this discrepancy between the theory and experiments is because of the sensitivity of shell buckling to imperfections. Koiter (1945) developed the general theory of stability for elastic structures subject to a conservative loading, and by applying this shell theory, a plethora of theoretical and computational studies were conducted to investigate the effect of various imperfections on the buckling behavior, as reviewed in Chapter 1. In addition, it was found that the most critical type of imperfections is those that comprise a geometric variation from the original target shape. Still, there is a lack of experimental studies showing a direct relationship between the critical buckling pressure of spherical shells and the geometric properties of their imperfections.

3.2 Fabrication and experimental measurement of the buckling load of imperfect shells

We have performed precise model experiments to investigate how the buckling strength of hemispherical elastic shells under pressure loading is affected by a geometric imperfection. In this section, we start by describing the rapid prototyping technique used to fabricate our elastomeric shells containing a well defined 'dimple-like' defect at their pole. The profile of this dimple-like defect is then characterized through digital image processing. Finally, we present the experimental apparatus used to pneumatically load the thin hemispherical shells and measure the critical pressure at which the shells buckle.

3.2.1 Fabrication method to produce precisely imperfect thin elastic shells

Our thin elastic shells were fabricated by coating a spherical mold with a polymer solution, following a protocol similar to that introduced in Chapter 2, the basis of

which is highlighted next. Two variations of this technique enable us first to fabricate deformable (elastic) molds, which are then used to produce thin elastic shells containing a single dimple-like defect.

First, the hemispherical elastic molds were fabricated by coating the surface of a rigid hemisphere (radius $R = 24.85\,\text{mm}$, machined out of polyacetal by CNC milling) with a polymer solution of Vinylpolysiloxane (VPS, Elite Double 32, Zhermack), a silicone-based elastomer. This VPS-32 polymer was mixed with a ratio of base to curing agent 1:1 in weight, for 10 s at 2000 rpm (clockwise), and then 10 s at 2200 rpm (counterclockwise) using a centrifugal mixer (ARE-310, Thinky Co.). The VPS solution was poured on the hemisphere and cured in approximately 20 min at room temperature (20°C). Upon curing and peeling from the rigid hemisphere, a VPS shell of thickness $h = 195\,\mu\text{m}$ was produced. Repeating the coating process multiple times before peeling, enabled us to systematically increase the thickness of the shell, which once thick enough, itself became the flexible (deformable) mold that was subsequently employed to fabricate the actual shell specimens used in the experiments. Three different molds were fabricated with thicknesses, $h_{\text{mold}} = \{585, 975, 1170\}\,\mu\text{m}$, by repeating the coating 3, 5 and 6 times, respectively. The Young's modulus of cured VPS-32 was measured to be $E = 1.255$ MPa and its Poisson's ratio was assumed to be $\nu = 0.5$.

The actual thin spherical specimens used in the experiments were fabricated following the same protocol described above, but using the thick elastic shells, themselves employed as molds. The VPS solution was poured onto the concave underside of the mold and turned upside down to drain the excess polymer and produce a thin lubrication film. The curing of this liquid film yielded a thin shell with $h = 230\,\mu\text{m}$. Note that this value of h was slightly higher than that reported above for a single coating step of the mold due to a slightly longer waiting time between the mixing of the polymer and pouring onto the mold to allow sufficient time to prepare the apparatus and form the defect (more below). The details on relation between the waiting time and the resulting shell thickness was given in Sec. 2.9. The thin shells obtained this way had uncontrollable imperfections that were intrinsic to the fabrication process,

for example, systematic variations of the shell thickness (6.6% standard deviation from pole to equator given in Sec. 2.6), air bubbles, inhomogeneity of the polymer mixture, and the surface roughness of the mold. However, these imperfections could be overshadowed by the single 'dimple-like' defect that was precisely introduced in the shell fabrication protocol, as is described next.

In Fig. 3-1, we present a series of photographs, along with corresponding schematic diagrams, which illustrate the fabrication protocol of our *imperfect* thin hemispherical shells containing a precisely engineered defect. After filling the thick flexible mold with the VPS-32 solution (Fig. 3-1(a1, b1)), and then draining the excess liquid (Fig. 3-1(a2, b2)), the pole of the mold was indented by a flat plate (Fig. 3-1(a3, b3)) that was attached to a universal testing machine (5943, Instron). We assume that the mold indentation results in the same displacement of the shell pole from its perfect spherical geometry, such that it defines the amplitude, δ, of the defect. This assumption will be validated in Sec. 3.3.1 through FEM simulations. To set δ, we programmed the Instron to move the indentation tip at a constant velocity (0.3 mm/min) until a specific load was detected by a 10 N load cell, corresponding to the targeted amplitude (based on the linear load-displacement relation), and then fixed this position. The defect amplitude, δ, was therefore defined as the distance

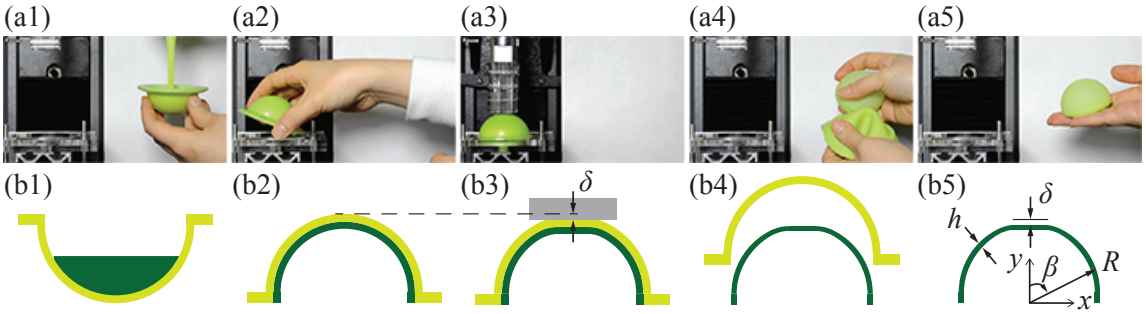

Figure 3-1: **Fabrication of the thin shell specimens.** (a) Photographs and (b) schematic diagrams of the fabrication protocol used to produce thin spherical shells with a dimple-like defect. (1) A thick VPS mold shell is filled with VPS solution and (2) turned upside down. (3) A dimple-like defect is introduced by indenting the pole of the mold shell with an Instron machine, immediately after pouring of VPS. (4-5) Upon curing, a thin elastic shell containing a geometric defect is peeled off from the mold.

between the position where the onset of a non-zero load was first detected and the position at which the target load was reached. While holding the indentation constant, the VPS solution cured inside of the deformed mold (Fig. 3-1(a3, b3)). Upon curing and peeling from the mold (Fig. 3-1(a4, b4)), the final shells had the thickness, $h = 230 \pm 11\,\mu\text{m}$ (the uncertainty corresponds to a standard deviation of 10 fabricated shells), resulting in a radius to thickness ratio of $\eta = 108$. Moreover, this procedure of deforming the mold through indentation allowed us to produce shells with a single 'dimple-like' defect at its pole, whose amplitude could be varied in the range $0 < \delta\,[\mu\text{m}] < 542$. A localized thicker band ($\approx 2\,\text{mm}$ thickness) at the equator due to the accumulation of excess polymer ensured that the boundary conditions there were clamped.

3.2.2 Shape of the 'dimple-like' defect

Whereas the fabrication technique presented above enables us to control the amplitude of the defect, δ, through the depth of the indentation, the precise shape of the dimple is self-selected by the elastic properties and, hence, the deformation of the flexible mold. In particular, we are interested in characterizing the defect by the radial deviation from a spherical shape, w_{I}, as a function of the zenith angle, β.

We experimentally measured this $w_{\text{I}}(\beta)$ profile through digital imaging. First, we took side-view photographs of shells (Nikon D3200 camera, with a Micro-NIKKOR 60 mm lens). Then, we extracted the shell contour from digitized images by an edge detection algorithm (image processing toolbox, Matlab). A circle was fit to the region away from the pole, where the effect of the indentation is negligible, corresponding to the profile of the defect-free spherical shell. The difference between this circle and the digitized profile defines $w_{\text{I}}(\beta)$.

Two representative examples of experimental imperfection profiles are provided in Fig. 3-2(b), for two shells fabricated using molds with $h_{\text{mold}} = 585$ and $1170\,\mu\text{m}$, both of which with the same defect amplitude $\delta = 207\,\mu\text{m}$. These profiles exhibit inward, radially symmetric, and 'dimple-like' deflections at the vicinity of the pole ($\beta \lesssim 20^\circ$), beyond which the shell remains spherical, $w_{\text{I}}(\beta \gtrsim 20^\circ) \approx 0$. We have also performed

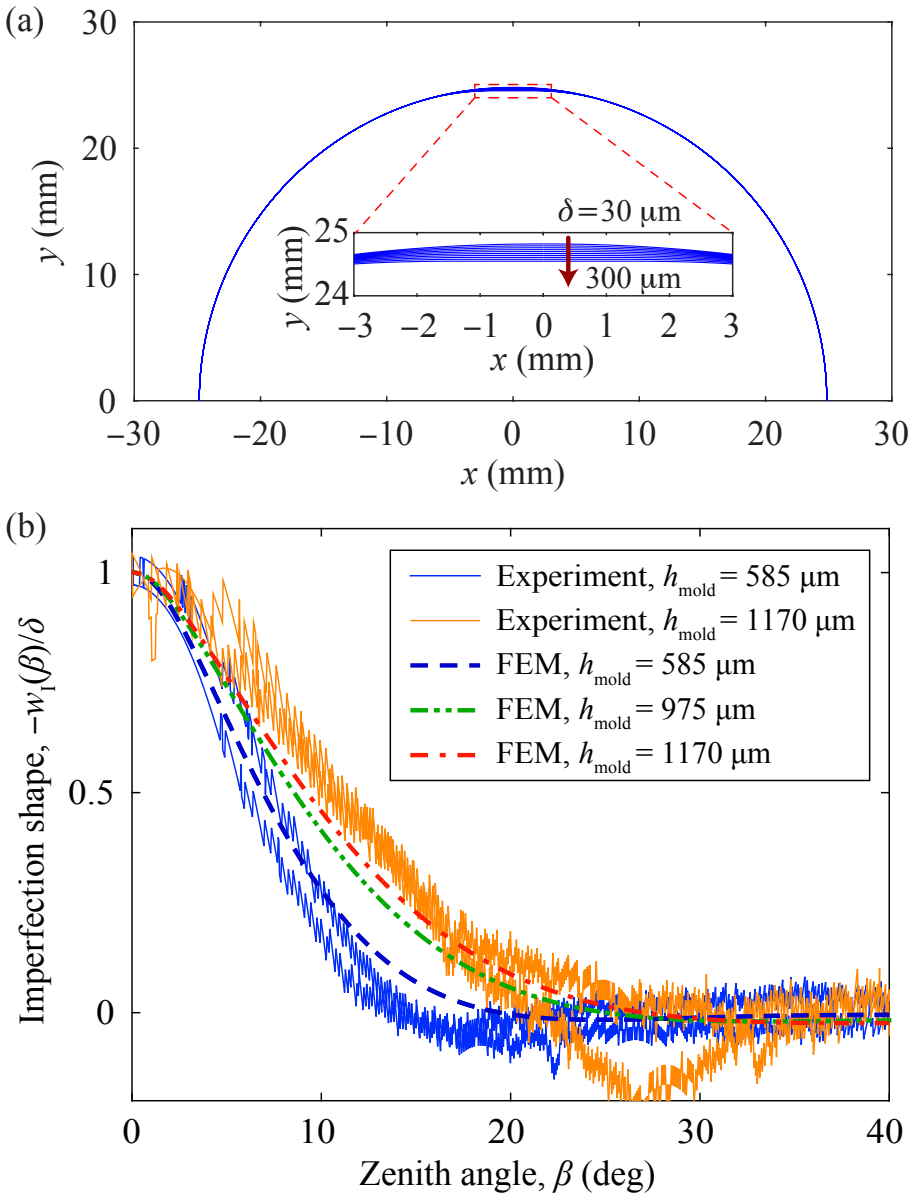

Figure 3-2: **Profiles of the dimple-like defects.** (a) Profiles of the indented mold calculated by FEM with $h_{\text{mold}} = 585$ μm and $30 \leq \delta$ (μm) ≤ 300 (in steps of 30) are plotted in (x, y)-coordinates. Inset: Magnified profiles in the vicinity of the pole. (b) Angular profile of the defect versus zenith angle for shells with $\delta = 207$ μm: experiments with $h_{\text{mold}} = \{585, 1170\}$ μm (solid lines) FEM with $h_{\text{mold}} = \{585, 975, 1170\}$ μm (dashed, dashed-dotted-dotted, and dashed-dotted lines, respectively).

FEM simulations to corroborate these findings, which will be presented in Sec. 3.3.1.

3.2.3 Measuring the critical buckling pressure of the shells

The experimental critical buckling pressure, $p_{\max}$, was measured for each shell using the following procedure. The shell was first mounted onto an acrylic plate with a hole at its center, and connected to both a syringe pump (NE-1000, New Era Pump Systems, Inc.) and a pressure sensor (MPXV7002, NXP semiconductors). The air inside the shell was then extracted at the imposed constant flow rate of 0.1 ml/min while monitoring its internal pressure at an acquisition rate of 1 Hz using the pressure sensor. The internal pressure decreased gradually with time, until a minimum value was reached, at which point the shell buckled. In Fig. 3-3, we plot the time variation of the net external pressure, p, that is differential between the outside (atmospheric pressure) and the inside of the shell. The pressure, p, continuously increased with

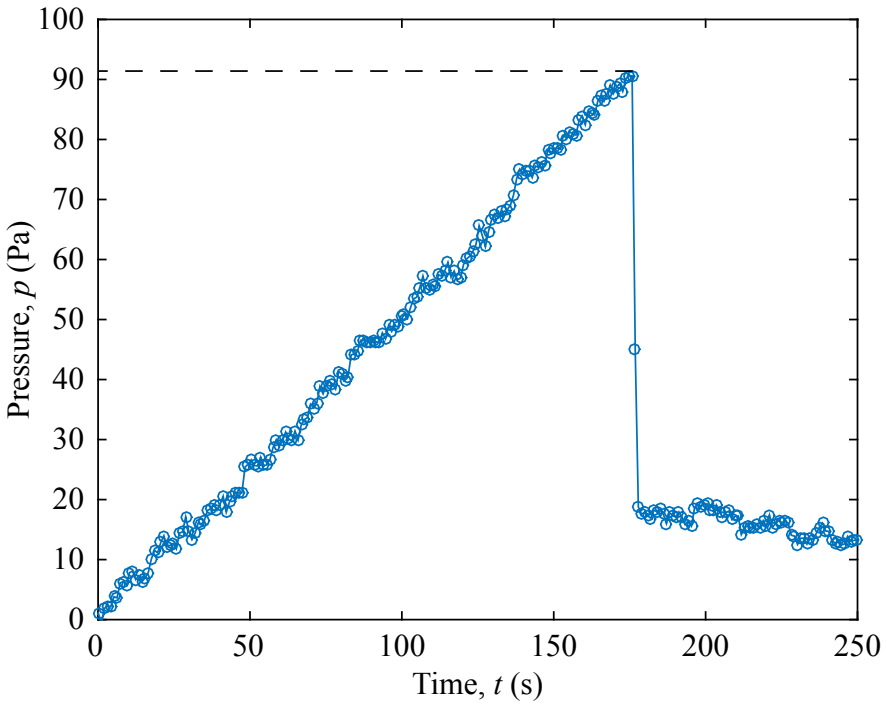

Figure 3-3: **Net external pressure versus time during air extraction.** Pressure differential between the outside and inside of the shell with $h = 230\,\mu$m, $R = 24.74$ mm and no defect.

time and jumped down right after it reached the maximum. This maximum pressure attained (dashed line) was defined as the critical buckling pressure, $p_{\max}$.

3.2.4 Experimental procedure and range of parameters

We proceed by describing the experimental procedure used to measure $p_{\max}$ for a collection of shells containing precisely designed geometric imperfections, of different amplitudes and widths. First, 60 shells were fabricated following the protocol detailed in Sec. 3.2.1, using the three elastic molds with $h_{\text{mold}} = \{585, 975, 1170\}$ µm to change the width of the defect, and we systematically varied the mold indentation depth to obtain defect amplitudes in the range $0 \leq \delta\,[\mu\text{m}] \leq 542$. Throughout, the radius and thickness of the shell were kept fixed at $R = 24.74\,\text{mm}$ and $h = 230\,\mu\text{m}$, such that $\eta = R/h = 108$. For each shell, three identical experimental runs were conducted; each experimental data point represents the average of these measurements, and its error bars represent the standard deviation, although these are typically smaller than the size of symbols .

3.3 Finite Element Simulations to characterize the imperfect shells

The FEM simulations reported in the present chapter were performed in collaboration with Francisco López Jiménez (University of Colorado Boulder) and using the commercial package Abaqus/Standard. The model was simplified to be two-dimensional by assuming axisymmetry. This simplification reduced the computational cost by approximately a factor of 20, compared to an equivalent model using a three-dimensional description of the structure using shell elements. The shells were treated as incompressible Neo-Hookean solids, and reduced hybrid axisymmetric elements CAX4RH were employed. A convergence study was performed, which led to the selection of a regular mesh with 1000 elements in the zenith direction and an equivalent mesh size in the radial direction (between 6 and 30 elements, depending on the shell thickness).

All analyses considered a nonlinear geometry.

Two different sets of FEM simulations were performed for the following purposes. The first set was to characterize the shape of the shells obtained through the fabrication process, and the second set was to calculate the buckling load and post-buckling response of the shells under external pressure, for shells with a variety of defect geometries.

3.3.1 FEM results for the profile of the deformed molds

The goal of the first set of FEM simulations was to model the fabrication procedure and determine the shape of the engineered defect, for different levels of indentation of the flexible molds. Each mold was essentially a flexible thick shell (mold thicknesses, $h_{\text{mold}} = \{585,\, 975,\, 1170\}\,\mu\text{m}$) and the indentation plate was modeled as a rigid surface using RAX2 elements. A frictionless general contact was defined between all free surfaces. The indentation loading was modeled by imposing the vertical displacement of the plate, which resulted in the deformation of the mold. At the end of the simulation, the position of the inner surface of the mold was extracted and assumed to be equal to the outer surface of the fabricated shell. The defect is defined as the radial displacement, w_{I}, as a function of the zenith angle, β. The amplitude of the defect, δ, is equal to the negative of the deflection at the pole, $-w_{\text{I}}(\beta = 0)$.

Our simulations show that the width of the defect, defined as the zenith angle at which the deflection, w_{I}, becomes negligible, increases significantly with the thickness of the mold, h_{mold}, and only very slightly with the defect amplitude, δ. Figure 3-2(a) shows the profiles of shells with $h_{\text{mold}} = 585\,\mu\text{m}$ and $30 \leq \delta\,[\mu\text{m}] \leq 300$. The defect is highly localized near the pole ($\beta = 0$), and the small variation of the profile of the shell for increased values of δ can be seen in the zoomed inset of Fig. 3-2(a).

The shape of different defects can be more easily compared when $w_{\text{I}}(\beta)$ is normalized by δ. In Fig. 3-2(b), we compare the defect profiles obtained from FEM simulations and experiments (see Sec. 3.2.2), finding excellent agreement between the two. The results used in this comparison correspond to shells with the same defect amplitude, $\delta = 207\,\mu\text{m}$, fabricated using two molds of thickness, $h_{\text{mold}} = 585$

and 1170 µm. The clear difference between the two profiles obtained with the different molds demonstrates that the overall shape of the defect (*e.g.*, its width) can be controlled by varying the thickness of the mold.

Given the good agreement between the FEM simulations and the experiments, for the remainder of this chapter, the reported defect amplitudes and the corresponding profiles will be computed from FEM using the corresponding experimental parameters. This choice was made due to the laborious procedure that would be required to systematically extract the same quantities from the experiments.

3.3.2 FEM results for the imperfection sensitivity

The second set of FEM simulations was then performed to investigate the effect of the geometry of the imperfections on the buckling load of shells under external pressure. In this case, the loading was modeled as a live pressure and applied on the outer surface of the shells. We found that using the BUCKLE analysis in Abaqus significantly overestimates the buckling pressure, even with an existent defect. The reason is that the BUCKLE procedure involves a linearized buckling analysis that does not take into account the deformation prior to the instability, which takes place in the principal solution. To account for the nonlinear geometry and given that the collapse of the shells is unstable (Thompson, 1962), the simulations employed the Riks (1979) method to simultaneously solve for loads and displacements, and the progress of the analysis was measured by the arc-length of the load-displacement. The buckling pressure was then defined as the maximum pressure attained in the analysis.

The thickness of the shell was set to $h = 230\,\mu\text{m}$, and the geometric imperfections were directly introduced in the mesh. Two approaches for defining the shape of the defect were followed. First, for one-to-one comparison with the experiments, the profile of the shells was directly taken from the complete modeling of the full fabrication process detailed in Sec. 3.3.1. In this set of simulations, the geometry of the defects changed for every value of the thickness of the mold and the applied indentation. The results from these simulations are presented and compared to experiments in Figs. 3-

2(b) and 3-4. Secondly, to more thoroughly decouple the effect of the amplitude and the width of the defect, we chose the simpler defect profile of a Gaussian dimple

$$w_{\mathrm{I}} = -\delta e^{-(\beta/\beta_0)^2}, \tag{3.1}$$

where β_0 controls the width of the defect. This simple parameterization allowed us to perform a systematic study of the effect of the dimple geometry on the buckling pressure of the shells, presented in Secs. 3.7 and 3.8.

Moreover, to eventually establish parallels with existing literature, we introduce the geometric parameter (Kaplan & Fung, 1954) to characterize the defect in a dimensionless manner,

$$\lambda = \left\{12(1-\nu^2)\right\}^{1/4} \eta^{1/2}\, \alpha, \tag{3.2}$$

where α is the edge-angle of a shallow spherical shell segment measured from the axis of symmetry. Kaplan & Fung (1954) showed that the nonlinear buckling behavior of a shallow spherical shell is set by λ, and subsequent studies have tended to present the buckling pressure of shallow spherical shells as a function of this geometric quantity (Kaplan & Fung, 1954; Homewood et al., 1961; Seaman, 1962; Krenzke & Kiernan, 1963). In the results presented in Sec. 3.8, we will use a minor modification of the above definition of λ that replaces α by the angular width of the imperfection β_0 from Eq. (3.1), thereby assuming that the nonlinear deformation occurs only in the region of the shell containing the 'dimple-like' defect. This replacement is similar to the approach followed in the classic numerical analysis of Koga & Hoff (1969).

3.4 Comparison between experiments and FEM

We now follow the methodologies presented in Secs. 3.2 and 3.3 to compare the experimental and FEM results on the critical buckling pressure. In Fig. 3-4, we plot the knockdown factor, $\kappa_{\mathrm{d}} = p_{\max}/p_{\mathrm{c}}$ (normalized critical buckling pressure), as a function of the dimensionless defect amplitude, $\bar{\delta} = \delta/h$ (normalized by the shell thickness), of a single 'dimple-like' defect. Three data sets are presented for

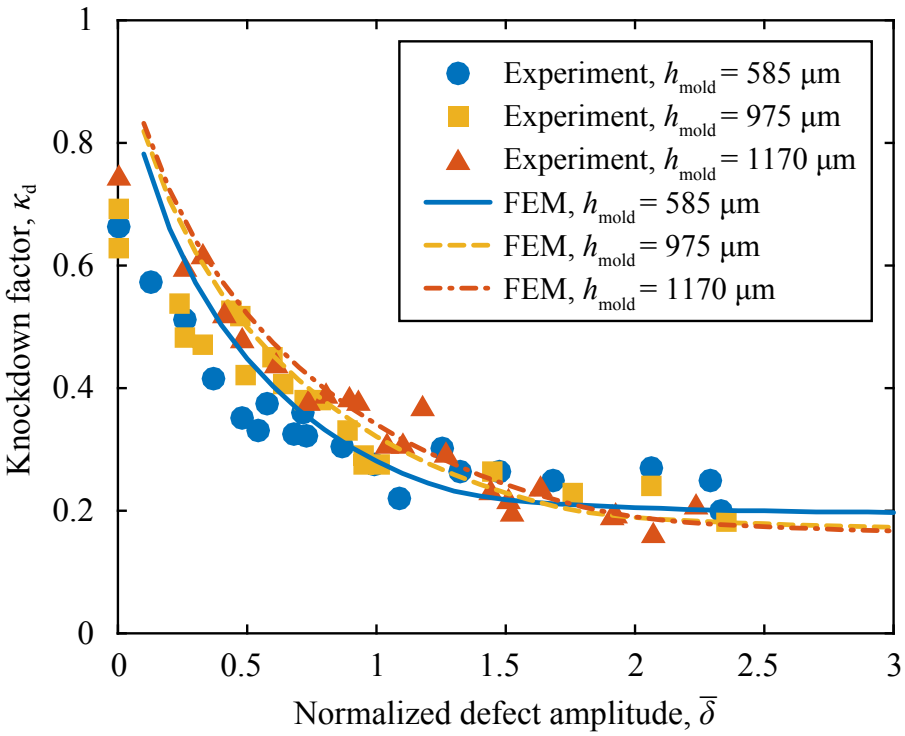

Figure 3-4: **Knockdown factor, $\kappa_d = p_{max}/p_c$, versus the normalized defect amplitude, $\bar{\delta} = \delta/h$.** In experiments (closed symbols), the shell specimens were fabricated in the ranges of parameters, $h_{mold} = \{585, 975, 1170\}$ μm and $0 \leq \bar{\delta} \leq 2.36$. The lines represent FEM data in which the defect profiles obtained by simulations with $h_{mold} = \{585, 975, 1170\}$ μm were introduced to vary the angular width of the defect.

shells fabricated from molds with $h_{mold} = \{585, 975, 1170\}$ μm, resulting in defects of increasingly larger angular width, as characterized in Secs. 3.2.2 and 3.3.1.

Focusing first on the experiments, for a shell without an engineered defect ($\bar{\delta} = 0$), we find a knockdown factor of $\kappa_d = 0.69 \pm 0.06$. This lower than unity value is due to the uncontrollable imperfections that are intrinsic to the fabrication and experimental procedures. These include variations in the shell thickness from the pole to the equator (Sec. 2.6), small air bubbles trapped in the elastomer during fabrication and self-weight of the shell, all of which are not taken into account in the classic theoretical prediction of Eq. (1.1). With the presence of a defect ($\bar{\delta} > 0$), the knockdown factor varies widely in the range $0.15 < \kappa_d < 0.75$, but in a way that can be robustly and reproducibly set by systematically varying the geometry of the defect. The $\kappa_d(\bar{\delta})$ data

first sharply decreases for $0 < \bar{\delta} \lesssim 1.5$, but eventually reaches a plateau when $\bar{\delta} \gtrsim 1.5$ at $\kappa_{\mathrm{d}} \sim 0.2$. For $\bar{\delta} \lesssim 1.5$, shells with wider defects (*e.g.*, obtained by using the thicker mold with $h_{\mathrm{mold}} = 1170\,\mu\mathrm{m}$) have knockdown factors that are slightly higher than narrower defects (*e.g.*, obtained by using the thinner mold with $h_{\mathrm{mold}} = 585\,\mu\mathrm{m}$), but this trend is inverted for $\bar{\delta} \gtrsim 1.5$, even if the differences between the three datasets are relatively small.

The experimental results presented above corroborate the seminal numerical predictions both by Hutchinson (1967) for defect shaped with the critical buckling mode at onset and by Koga & Hoff (1969) for axisymmetric dimple-like defects. Note, however, that the shape of the defect considered by Hutchinson was different from ours, and Koga and Hoff overestimated the effect of the dimpled defects (Hutchinson, 2016). Moreover, the maximum defect amplitudes considered by both of these previous studies were $\bar{\delta} = 0.75$ (Hutchinson, 1967) and $\bar{\delta} = 0.5$ (Koga & Hoff, 1969), respectively, such that they did not observe the development of the plateau, whereas we were able to fabricate shells with a defect up to $\bar{\delta} = 2.36$.

In Fig. 3-4, we superpose FEM results onto the experimental data for identical parameter values and find remarkable quantitative agreement. Specifically, the FEM data show the presence of a clear plateau at high values of $\bar{\delta}$, as well as the crossing and subsequent inversion in the relative buckling strength for shells with different angular widths of defects, when $\bar{\delta} \gtrsim 1.5$. For the parameters explored, the level of this plateau lies in the range $0.17 < p_{\mathrm{plateau}}/p_{\mathrm{c}} < 0.20$, such that the buckling pressure has a lower bound at these values. In Sec. 3.8, we will further explore the FEM simulations results to systematically quantify the level and onset (in $\bar{\delta}$) of the plateau as functions of the defect geometry.

To the best of our knowledge, this is the first time that experimental results are reported showing a direct relationship between the critical buckling pressure of spherical shells and the systematically varied geometric properties of the imperfection. Moreover, for a given defect geometry, we are able to accurately predict the associated knockdown factors through FEM simulations. Our results are in stark contrast to the broad spread in the experimental data extracted from the literature shown in Fig. 1-2,

as well as the inability for the classic theories, *e.g.*, Eq. (1.1), to predict them.

We proceed by supporting this comparison between FEM simulations and experiments with an analytical description based on a first order shell theory. John Hutchinson has specialized this theory for shells containing a single 'dimple-like' defect, which yields a set of nonlinear ODEs. In Sec. 3.7, numerical solutions of this set of ODEs will be compared directly with FEM results.

3.5 Formulation of the shell theory

We now review a formulation of shell buckling equations using a small strains and moderate rotations theory, and the numerical solution of the underlying ODEs for the special case of a spherical shell containing a dimple-like defect, which were recently developed by our collaborator John W. Hutchinson. A more detailed account of the material of this section can be found in the following references: (Hutchinson, 2016; Lee et al., 2016b). In the context of the research of this thesis, by focusing on the maximum pressure that the shell can support, Hutchinson demonstrated that middle surface strains remain *'very small'* and rotations remain *'moderately small'*. In nonlinear shell theory, the above qualitative statements translate into middle surface strains, ϵ, satisfying $|\epsilon| \ll 1$ and rotations, φ, satisfying $\varphi^2 \ll 1$. Rotations about the tangents to the middle surface are the most important, while rotation about the normal to the shell middle surface turns out to be small in spherical shell buckling. Nevertheless, the equations employed accommodate moderate rotations about the normal. This analysis indicated that there is essentially no difference between dead and live pressure for the behavior of interest in the current study. Accurate equations for the first-order shell theory with small strains and moderate rotations were given by Sanders Jr. (1963), Koiter (1966, 1967) and Budiansky (1968). Below, we describe how Hutchinson specialized this shell theory for initially perfect spherical shells followed by the introduction of initial imperfections (in Sec. 3.6), emphasizing that all of the work of *this section* is his, even it was largely motivated by the experimental and FEM results presented throughout this thesis.

Euler coordinates (ω, θ, r) were employed with r as the distance from the origin, ω as the circumferential angle, and $\theta = \pi/2 - \beta$ as the meridional angle ranging from 0 at the equator to $\pi/2$ at the pole. The r of the undeformed middle surface of the shell is R. A material point at (ω, θ, R) on the middle surface of the undeformed shell is located on the deformed shell at

$$\mathbf{r} = u_\omega \mathbf{i}_\omega + u_\theta \mathbf{i}_\theta + (R + w)\mathbf{i}_r, \tag{3.3}$$

where $(\mathbf{i}_\omega, \mathbf{i}_\theta, \mathbf{i}_r)$ are unit vectors tangent and normal to the undeformed middle surface associated with the respective coordinates. For general deflections, the displacements (u_ω, u_θ, w) are taken as functions of ω and θ. For axisymmetric deflections, $u_\omega = 0$, while the other two displacements are functions only of θ.

The nonlinear strain-displacement relations make use of the linearized middle surface strains $(e_{\omega\omega}, e_{\theta\theta}, e_{\omega\theta})$ and the linearized rotations $(\varphi_\omega, \varphi_\theta, \varphi_r)$ with the rotation components about $\mathbf{i}_\omega$, $\mathbf{i}_\theta$ and $\mathbf{i}_r$, respectively, which are expressed as

$$\begin{aligned}
e_{\omega\omega} &= \frac{1}{R}\left(\frac{1}{\cos\theta}\frac{\partial u_\omega}{\partial \omega} - \tan\theta u_\theta + w\right), \\
e_{\theta\theta} &= \frac{1}{R}\left(\frac{\partial u_\theta}{\partial \theta} + w\right), \\
e_{\omega\theta} &= \frac{1}{2R}\left(\frac{\partial u_\omega}{\partial \theta} + \frac{1}{\cos\theta}\frac{\partial u_\theta}{\partial \omega} + \tan\theta u_\omega\right),
\end{aligned} \tag{3.4}$$

and

$$\begin{aligned}
\varphi_\omega &= \frac{1}{R}\left(-\frac{1}{\cos\theta}\frac{\partial w}{\partial \omega} + u_\omega\right), \\
\varphi_\theta &= \frac{1}{R}\left(-\frac{\partial w}{\partial \theta} + u_\theta\right), \\
\varphi_r &= \frac{1}{2R}\left(\frac{1}{\cos\theta}\frac{\partial u_\theta}{\partial \omega} + \tan\theta u_\omega - \frac{\partial u_\omega}{\partial \theta}\right).
\end{aligned} \tag{3.5}$$

In the small strain and moderate rotation theory, the middle surface strains are

nonlinear

$$
\begin{aligned}
E_{\omega\omega} &= e_{\omega\omega} + \frac{1}{2}\varphi_\omega^2 + \frac{1}{2}\varphi_r^2, \\
E_{\theta\theta} &= e_{\theta\theta} + \frac{1}{2}\varphi_\theta^2 + \frac{1}{2}\varphi_r^2, \\
E_{\omega\theta} &= e_{\omega\theta} + \frac{1}{2}\varphi_\omega\varphi_\theta,
\end{aligned}
\tag{3.6}
$$

while the curvatures are linear

$$
\begin{aligned}
K_{\omega\omega} &= \frac{1}{R}\left(\frac{\partial\varphi_\omega}{\partial\omega} - \tan\theta\varphi_\theta\right), \\
K_{\theta\theta} &= \frac{1}{R}\frac{\partial\varphi_\theta}{\partial\theta}, \\
K_{\omega\theta} &= \frac{1}{2R}\left(\frac{\partial\varphi_\omega}{\partial\theta} + \frac{1}{\cos\theta}\frac{\partial\varphi_\theta}{\partial\omega} + \tan\theta\varphi_\omega\right).
\end{aligned}
\tag{3.7}
$$

Similar to the work performed throughout this thesis, the imperfections were assumed to be in the form of a small, initial stress-free radial deflection of the middle surface, w_{I}, from the perfect spherical shape with $(u_\omega, u_\theta)_{\mathrm{I}} = 0$. Other imperfections in the form of thickness variations or residual stresses were not investigated. In addition, the attention has been limited to *axisymmetric imperfections* such that w_{I} is a function only of θ, not of ω. Assuming that w_{I} itself produces small middle surface strains and moderate rotations (a condition easily met in all our examples), $E^I_{\alpha\beta}$ denotes the strains in Eq. (3.6) arising from w_{I}. The total strains due to $(u_\omega, u_\theta, w_{\mathrm{I}} + w)$, where the radial displacement, w, is additional to the imperfection, w_{I}, are denoted by $E^{I+U}_{\alpha\beta}$ and the strains that give rise to stress arising from displacements additional to w_{I} are $E_{\alpha\beta} = E^{I+U}_{\alpha\beta} - E^I_{\alpha\beta}$:

$$
\begin{aligned}
E_{\omega\omega} &= e_{\omega\omega} + \frac{1}{2}\varphi_\omega^2 + \frac{1}{2}\varphi_r^2, \\
E_{\theta\theta} &= e_{\theta\theta} + \frac{1}{2}\varphi_\theta^2 + \frac{1}{2}\varphi_r^2 - \frac{1}{R}\frac{dw_{\mathrm{I}}}{d\theta}\varphi_\theta, \\
E_{\omega\theta} &= e_{\omega\theta} + \frac{1}{2}\varphi_\omega\varphi_\theta - \frac{1}{2R}\frac{dw_{\mathrm{I}}}{d\theta}\varphi_\omega.
\end{aligned}
\tag{3.8}
$$

Given that the curvatures are linear in the displacements and their gradients, the same process reveals that Eqs. (3.7) still hold for the relationship between the curvatures and the additional displacements, with no influence of w_{I}. From hereon, the additional displacements (u_ω, u_θ, w) will simply be referred to as *'the displacements'*.

The stress-strain relations for a shell of isotropic material in the first order shell theory are (Budiansky, 1968)

$$\begin{aligned} N_{\alpha\beta} &= \frac{Eh}{(1-\nu^2)}\left[(1-\nu)E_{\alpha\beta} + \nu E_{\gamma\gamma}\delta_{\alpha\beta}\right], \\ M_{\alpha\beta} &= D\left[(1-\nu)K_{\alpha\beta} + \nu K_{\gamma\gamma}\delta_{\alpha\beta}\right] \end{aligned} \tag{3.9}$$

with bending stiffness $D = Eh^3/[12(1-\nu)^2]$. The resultant membrane stresses are $(N_{\omega\omega}, N_{\theta\theta}, N_{\omega\theta})$ and the bending moments are $(M_{\omega\omega}, M_{\theta\theta}, M_{\omega\theta})$. With S denoting the spherical reference surface specified by $r = R$ and the Euler angles (ω, θ), the strain energy in the shell is

$$SE(u_\omega, u_\theta, w) = \frac{1}{2}\int_S \left\{M_{\alpha\beta}K_{\alpha\beta} + N_{\alpha\beta}E_{\alpha\beta}\right\} dS. \tag{3.10}$$

For a perfect shell, the potential energy, PE, of the uniform inward pressure p on the shell is the negative of the work done by the pressure. In the case of *dead pressure* (per original unit area of the middle surface and acting radially), the potential energy is

$$PE = p\int_S w dS. \tag{3.11}$$

Hutchinson (2016) has shown that, for our problem, live and dead pressure give identical results.

We proceed by introducing the effect of an axisymmetric initial imperfection w_{I} using the process described above for the strains, where w becomes additional to w_{I}. Because it is linear in w, the PE for dead pressure remains as Eq. (3.11). The energy of the loaded shell system is therefore

$$\Psi = SE(u_\omega, u_\theta, w) + pF(u_\omega, u_\theta, w), \tag{3.12}$$

where $PE = pF$, with F given by Eq. (3.11) for dead pressure.

3.6 Axisymmetric deformations of clamped hemispheres containing axisymmetric imperfections: a set of nonlinear ODEs

The equations presented in the previous section have been specialized by Hutchinson to axisymmetric deformations such that u_θ, w, and w_I are functions of θ and $u_\omega = 0$. Hemispherical shells ($0 \le \theta \le \pi/2$) clamped at the equator and subject to uniform inward pressure, p, were considered. Dimensionless displacements are defined as $U = u_\theta/R$, $W = w/R$ and $W_\mathrm{I} = w_\mathrm{I}/R$, and let $d()/d\theta = ()'$. Then, with

$$\begin{aligned} \varphi &\equiv \varphi_\theta = -W' + U, \\ e &\equiv e_{\theta\theta} = W + U', \end{aligned} \tag{3.13}$$

the non-zero strains and curvatures are

$$\begin{aligned} E_{\omega\omega} &= W - U\tan\theta, \\ E_{\theta\theta} &= e + \frac{1}{2}\varphi^2 - W_\mathrm{I}'\varphi, \\ K_{\omega\omega} &= -\frac{1}{R}\tan\theta\varphi, \\ K_{\theta\theta} &= \frac{1}{R}\varphi'. \end{aligned} \tag{3.14}$$

Equilibrium equations are generated either by requiring $\delta\Psi = 0$ in Eq. (3.12) for all admissible variations $(\delta U, \delta W)$ or, equivalently, by enforcing the principle of virtual work. The two equilibrium equations for the case of dead pressure are obtained as

$$\bar{m}_\theta'' + (\tan\theta\bar{m}_\omega)' - \frac{1}{(1-\nu^2)}\left[\hat{n}_\theta + \hat{n}_\omega + \{\hat{n}_\theta(\varphi - W_\mathrm{I}')\}'\right] - \hat{p} = 0, \tag{3.15}$$

and

$$\bar{m}_\theta' + \tan\theta\bar{m}_\omega + \frac{1}{(1-\nu^2)}\left\{\hat{n}_\theta' + \tan\theta\hat{n}_\omega - \hat{n}_\theta(\varphi - W_\mathrm{I}')\right\} = 0, \tag{3.16}$$

where $(\hat{n}_\omega, \hat{n}_\theta) = \frac{\hat{\alpha}}{Et}\cos\theta(N_{\omega\omega}, N_{\theta\theta})$, $(\bar{m}_\omega, \bar{m}_\theta) = \frac{R}{D}\cos\theta(M_{\omega\omega}, M_{\theta\theta})$, $\hat{p} = \frac{R^3}{D}\cos\theta p$, and $\hat{\alpha} = 12(R/h)^2$. The clamped boundary conditions at the equator require $U(0) =$

$W(0) = W'(0) = 0.$

The equilibrium equations can be expressed through the constitutive equations and the strain-displacement relations in terms of U and W or, equivalently, in terms of φ and W, with $U = W' + \varphi$. The most highly differentiated terms are φ''' and W''', thereby yielding a sixth order nonlinear ODE system. In all the problems considered in this thesis, the axisymmetric behavior is such that the inward deflection at the pole, $-W(\pi/2)$, increases monotonically, while the dimensionless pressure, $\tilde{p} = R^3 p/D$, increases in the early stages and then usually attains a limit point after which it decreases. For this reason, it is effective to treat $\tilde{p}$ as an unknown to introduce an extra ODE, $d\tilde{p}/d\theta = 0$, and to prescribe $-W(\pi/2)$ as the 'load parameter'. This augmented system can be reduced to seven first order ODEs in the standard form

$$\frac{d\mathbf{y}}{d\theta} = \mathbf{f}(\theta, \mathbf{y}), \tag{3.17}$$

where $\mathbf{y} = (\varphi'', \varphi', \varphi, W'', W', W, \tilde{p})$. Next, we provide the expressions for $\mathbf{f}(\theta, \mathbf{y})$ in Eq. (3.17), for the case of dead pressure:

$$\begin{aligned}
f_1 = \varphi''' =& \frac{1}{\cos\theta}\Big[(2+\nu)\sin\theta\varphi'' + (1+2\nu)\cos\theta\varphi' \\
&- \nu\sin\theta\varphi - \tan\theta\bar{m}'_\omega - \frac{\bar{m}_\omega}{\cos^2\theta} \\
&+ \hat{n}_\theta(1 + \varphi' - W''_{\mathrm{I}}) + \hat{n}_\omega + \hat{n}'_\theta(\varphi - W'_{\mathrm{I}}) + \hat{p}\Big], \\
f_2 = \varphi'',\ f_3 =& \varphi', \\
f_4 = W''' =& -\varphi'' - W' - \varphi'(\varphi - W'_{\mathrm{I}}) + \varphi W''_{\mathrm{I}} \\
&+ \tan\theta(E_{\theta\theta} + \nu E_{\omega\omega}) + \frac{1}{\hat{\alpha}\cos\theta}\Big[\hat{n}_\theta(\varphi - W'_{\mathrm{I}}) \\
&- \tan\theta(\hat{n}_\omega + \bar{m}_\omega) - \bar{m}'_\theta\Big], \\
f_5 = W'',\ f_6 =& W',\ f_7 = 0.
\end{aligned} \tag{3.18}$$

with $\bar{m}_\omega = -sin\theta\varphi + \nu\cos\theta\varphi'$, $\bar{m}'_\omega = \nu\cos\theta\varphi'' - (1+\nu)\sin\theta\varphi' - \cos\theta\varphi$, $\bar{m}'_\theta = \cos\theta(\varphi'' - \nu\varphi) - (1+\nu)\sin\theta\varphi'$, $\hat{n}_\omega = \hat{\alpha}\cos\theta(E_{\omega\omega} + \nu E_{\theta\theta})$, and $\hat{n}_\theta = \hat{\alpha}\cos\theta(E_{\theta\theta} + \nu E_{\omega\omega})$,

where $E_{\omega\omega}$ and $E_{\theta\theta}$ are given by Eqs. (3.13) and (3.14) using $U = \varphi + W'$. The derivative, $\hat{n}'_\theta$, is directly computed in terms of φ, W, and their derivatives.

At the equator ($\theta = 0$), the clamped boundary condition requires $\varphi = 0$, $W' = 0$ and $W = 0$. The functions φ and W are analytic at the pole, with φ being odd and W being even about the pole such that $\varphi = \varphi'' = W' = W''' = 0$ at $\theta = \pi/2$. At the pole, $f_2 = 0$, $f_3 = \varphi'$, $f_4 = 0$, $f_5 = W''$, $f_6 = 0$ and $f_7 = 0$. A somewhat lengthy expansion about the pole provides the following expression for φ''' at $\theta = \pi/2$:

$$\begin{aligned} f_1 = & \frac{3}{8}\Bigg[2\left(-\frac{1}{3}+\nu\right)\varphi' \\ & + 2\hat{\alpha}(1+\nu)(\varphi' + W'' + W)(1 + \varphi' - W''_{\mathrm{I}}) + \tilde{p}\Bigg]. \end{aligned} \tag{3.19}$$

Hutchinson has solved Eqs. (3.17) using a modern nonlinear ODE solver, which provides highly accurate results. In particular, the buckling pressure, *i.e.*, the maximum pressure attained at the limit point, can be calculated accurately and efficiently. This simulation effort used the ODE solver routine DBVPFD in IMSL (1994), which incorporates Newton iteration to satisfy the nonlinear equations and an automatic mesh refinement to meet accuracy tolerances. As already noted, the inward pole deflection serves as the loading parameter and it is increased in incremental steps using a converged solution at one step as the starting guess for the next step. The solution process is fast and robust. As will be illustrated, solutions can be readily obtained at deflections well past the limit point, beyond the onset of buckling. The results reported throughout have been computed assuming live pressure.

3.7 Comparison between ODE and FEM results

We proceed by comparing the results for the mechanical response of the shells obtained from both the ODE solution and FEM, which also serves as a joint verification of the two frameworks. Figure 3-5 shows the effect that imperfections with different amplitudes have on the pre- and post-buckling behavior, with a focus on the evolution of the pressure during deformation. For the remainder of this chapter, no results are

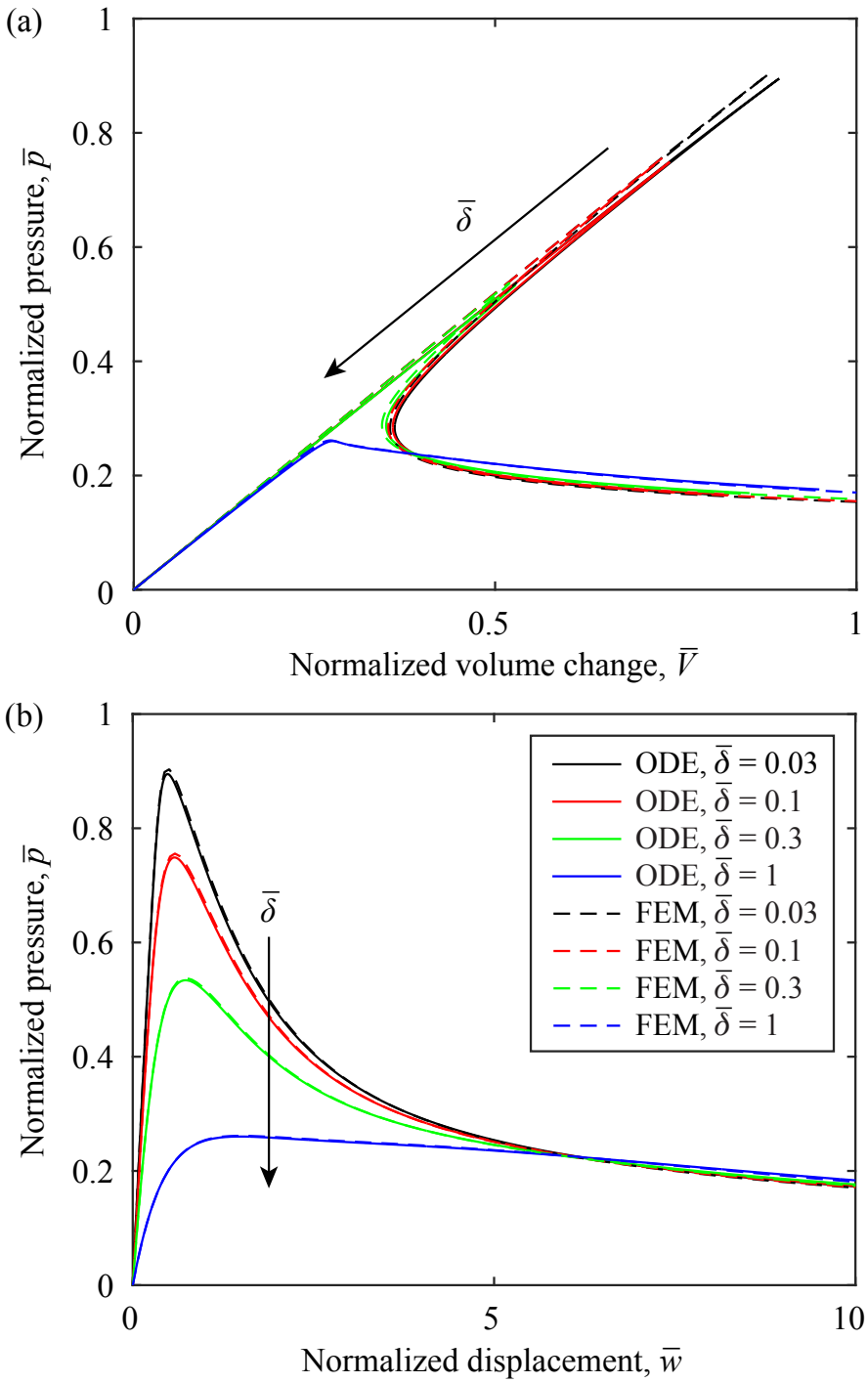

Figure 3-5: **Comparison between ODE (solid lines) and FEM (dashed lines) of the load-carrying behavior of imperfect shells.** (a) Normalized pressure, $\bar{p}$, as a function of the normalized volume change, $\bar{V}$. (b) Normalized pressure, $\bar{p}$, versus the normalized displacement at the pole, $\bar{w}$. Shells with radius-to-thickness ratio $\eta = 100$ containing a Gaussian dimple (Eq. (3.1)) with $\beta_0 = 8.83$ deg and $\bar{\delta} = \{0.03, 0.1, 0.3, 1\}$ were used.

provided for very small values of defect amplitude: $\bar{\delta} < 0.15$ for FEM and $\bar{\delta} < 0.2$ for the ODE solutions. The reason is that such deflections are too small to be accurately and reliably taken into account by the respective numerical algorithms.

In Fig. 3-5(a), we plot the normalized pressure, $\bar{p} = p/p_c$ versus the normalized volume change, $\bar{V} = \Delta V/V_0$, where V_0 is the total inside volume change of the perfect shell immediately prior to the onset of buckling, for both Hutchinson's ODE solution (solid lines) and FEM (dashed lines). For a nearly perfect shell with a small imperfection $\bar{\delta} = 0.03$ (black lines), the pressure first increases linearly with increasing $\bar{V}$ and reaches a maximum value, $\bar{p}_{\max} = p_{\max}/p_c = \kappa_d$, just before buckling occurs. Past this point, $\bar{p}$ decreases with decreasing $\bar{V}$, closely following the upward branch, and then turns around to eventually decreases with increasing $\bar{V}$. If $\bar{V}$ is imposed and increased monotonically, then the shell becomes unstable and undergoes snap-buckling almost immediately after the maximum normalized pressure, $\bar{p}_{\max}$, is attained. If the shell were perfect, there would be a pressure drop when $\bar{V} = 1$ to the lower branch at $\bar{p} \approx 0.2$, after which $\bar{p}$ would continue to decrease for increasing $\bar{V}$. For shells containing defects with higher values of $\bar{\delta}$, the volume change required for buckling decreases and the peak pressure, $\bar{p}_{\max}$, is progressively lower. Thus, even though increasing $\bar{\delta}$ weakens the shell, buckling is less catastrophic. When the imperfection amplitude is sufficiently large (*e.g.*, $\bar{\delta} \geq 1$), the pressure decreases smoothly after the maximum value is attained, without a pressure jump. It is important to highlight that in all of these results, the FEM and ODE data (dashed and solid lines, respectively) are nearly indistinguishable, which serves as a joint verification of both numerical approaches.

In Fig. 3-5(b), the same data presented in Fig. 3-5(a) is now replotted as a function of the normalized displacement of the shell pole, $\bar{w} = w/h$, to show the load-displacement behavior. For all curves (different values of the defect amplitude, $\bar{\delta}$), $\bar{p}$ initially increases sharply with $\bar{w}$ in the early stages of deformation (linear response), until a maximum pressure is reached at $\bar{w} \approx 1$, after which the pressure decreases. With increasing $\bar{\delta}$, the value of $\bar{p}_{\max} = \kappa_d$ decreases and the post-buckling decrease of $\bar{p}$ with $\bar{w}$ becomes less abrupt. Note that all the $\bar{p}(\bar{w})$ curves for the different values of $\bar{\delta}$ explored approach one another in the later stages of deformation ($\bar{w} > 5$).

Again, excellent agreement is found between the ODE solutions (solid lines) and FEM (dashed lines) results, with at most 0.9% relative difference in $\bar{p}_{\max}$ between the two.

3.8 Parametric exploration of the knockdown factor as a function of the imperfection geometry

Having characterized the load-bearing capacity of the imperfect shells with a defect of different amplitudes, $\bar{\delta}$, we now return to characterize the knockdown factor. First, we use a single geometric parameter, λ (Eq. (3.2)) to characterize the imperfect shells and then focus on the plateau observed for large defect amplitude $\bar{\delta} \gtrsim 1.5$ (first reported in Sec. 3.4). In particular, we focus on the dependence of the level and onset of this plateau on both the angular width of the defect, β_0 (Eq. (3.1)), and the radius to thickness ratio of the shell, $\eta = R/h$. Given the excellent agreement found in Sec. 3.4 between experiments and FEM (validation), as well as between FEM and the ODE solutions in Sec. 3.7 (verification), we center this discussion exclusively on the FEM and ODE results.

3.8.1 Characterization of the imperfect shell by a single geometric parameter

Following the works of Kaplan & Fung (1954) and Koga & Hoff (1969), we report our results with respect to the geometric parameter λ introduced in Eq. (3.2), but with $\alpha = \beta_0$, which considers the combined effect of η and β_0 for a dimensionless characterization of the defect geometry. We performed FEM simulations and ODE calculations for two sets of shells with $\eta = \{100, 200\}$ containing defects in the range $1 \leq \lambda \leq 5$ ($2.34^\circ \leq \beta_0 \leq 16.54^\circ$). In Fig. 3-6, their corresponding knockdown factors are plotted versus the normalized imperfection amplitude, $\bar{\delta}$.

In Fig. 3-6(a), we plot the knockdown factor, $\kappa_{\mathrm{d}} = \bar{p}_{\max}$, versus $\bar{\delta}$ for $1.5 \leq \lambda \leq 5$ (in steps of 0.5). For each value of λ, the ODE solutions (solid lines) and the FEM with $\eta = \{100, 200\}$ (dashed and dotted lines, respectively) all collapse onto grouped

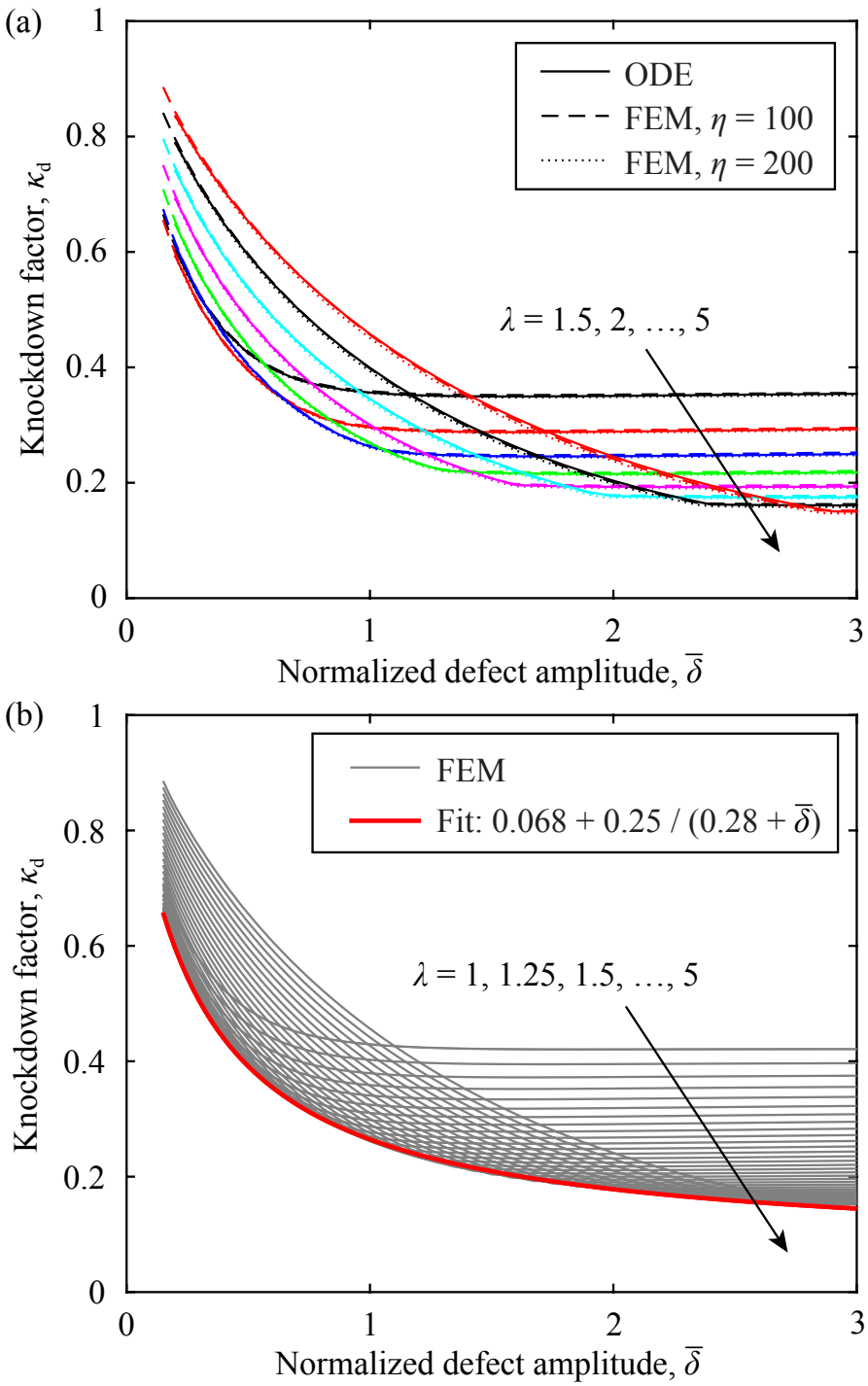

Figure 3-6: **Knockdown factor, κ_d, versus the normalized defect amplitude, $\bar{\delta}$, for a variety of λ.** (a) Solid lines represent the results of the ODE solutions, and dashed and dotted lines correspond to FEM simulations for different $\eta = \{100, 200\}$, respectively, with $1.5 \leq \lambda \leq 5$ in steps of 0.5. (b) FEM results for $1 \leq \lambda \leq 5$ in steps of 0.25. The lower bounding envelope (thick solid line) is determined by fitting (Eq. (3.20)).

curves. This indicates that for a fixed value of λ, the buckling behavior is not affected by different values of η. Moreover, these results demonstrate that the single geometric parameter λ characterizing the defects governs the imperfection sensitivity of our imperfect shells. All curves exhibit an initial decrease of κ_{d} with $\bar{\delta}$, followed by a plateau. As the geometric parameter, λ, of the defect is increased, the plateau appears at higher values of $\bar{\delta}$, and with a level that decreases monotonically with λ. For example, the narrow defect with $\lambda = 1.5$ has an initially sharp decrease of $\kappa_{\mathrm{d}}(\bar{\delta})$ and the plateau is attained at $\bar{\delta} \approx 1$, whereas the widest defect considered ($\lambda = 5$) exhibits a slower initial decay and the plateau is only reached after $\bar{\delta} \approx 3$.

In Fig. 3-6(b), we focus exclusively on FEM and present the same data as in Fig. 3-6(a), but with a higher density of data in the range $1 \leq \lambda \leq 5$, in steps of 0.25. At each value of $\bar{\delta}$, there is a critical geometric parameter, λ_{c}, that corresponds to the lowest buckling pressure, which is plotted in Fig. 3-7. The stepwise nature of these data stems from the discrete increase of λ in steps of 0.25, and a more continuous curve would have been obtained for a finer variation of this parameter. Koga & Hoff (1969) also studied the critical conditions that minimize κ_{d}, for dimple-like defects with amplitudes in the range $0.1 \leq \bar{\delta} \leq 0.5$, and reported a value of $\lambda_{\mathrm{c}} = 4$. By contrast, we observe that λ_{c} increases monotonically with $\bar{\delta}$, within the range of parameters studied, from $\lambda_{\mathrm{c}} = 1.875$ at $\bar{\delta} = 0.15$, up to $\lambda_{\mathrm{c}} = 5$ at $\bar{\delta} = 3$. This discrepancy is likely due to the rudimentary (but pioneering) computational tools available at the time of their study, as pointed out by Hutchinson (2016).

It is also interesting to note that there is a lower bounding envelope (thick solid curve in Fig. 3-6(b)) that encloses all of the $\kappa_{\mathrm{d}}(\bar{\delta})$ curves. Empirically, we have found that this minimum envelope is well described by

$$\kappa_d = 0.068 + \frac{0.25}{0.28 + \bar{\delta}}. \tag{3.20}$$

The empirical description of Eq. (3.20), together with the data in Fig. 3-7, should provide a useful design guideline for the shape that a defect should have in order for a shell to buckle at the lowest possible pressure. Whereas traditional applications

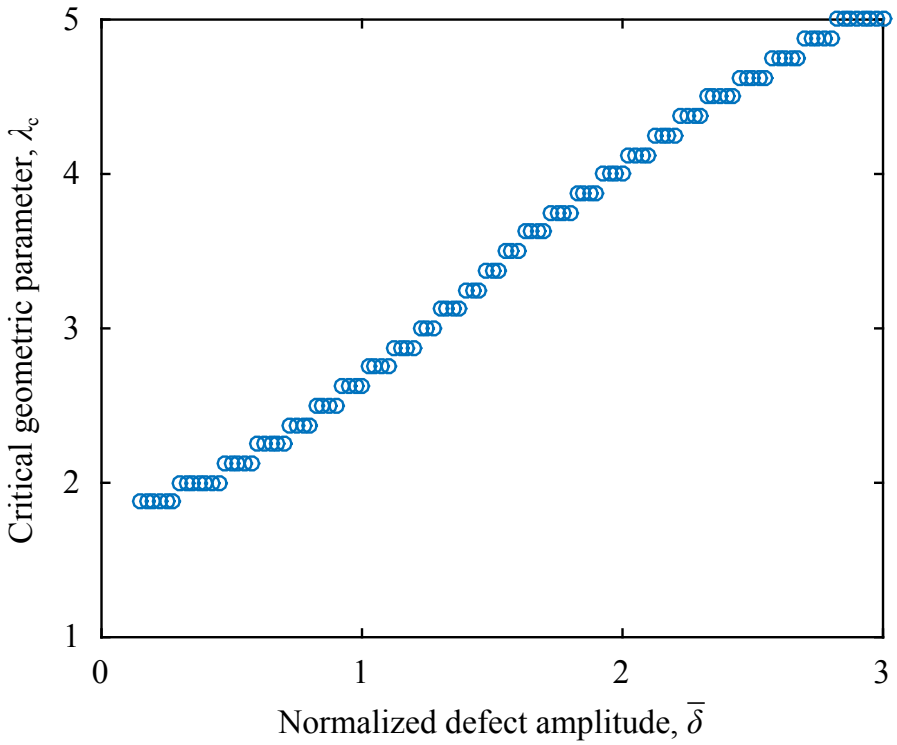

Figure 3-7: **Critical geometric parameter of the defect, λ_c, at which κ_d exhibits its minimum possible value for a given value of $\bar{\delta}$.** Each point was obtained from FEM results in Fig. 3-6(b) analyzing for $1 \leq \lambda \leq 5$ in steps of 0.25, which results in the stepwise nature of the data.

in structural mechanics would typically seek to maximize κ_d, these findings could be useful for the more recent movement of utilizing buckling as a mechanism for functionality (Reis, 2015; Reis et al., 2015).

3.8.2 Buckling plateau for large amplitude defects

Finally, we quantitatively characterize the pressure level and onset amplitude of the plateau in the $\kappa_d(\bar{\delta})$ data of Fig. 3-6(b). The dimensionless pressure level of the plateau, $\langle \kappa_d \rangle_{plateau}$, is the average of κ_d over the extent of the plateau and its onset, $\bar{\delta}_{plateau}$, is determined from

$$\left| \frac{d\kappa_d}{d\bar{\delta}} \right| \leq \xi, \tag{3.21}$$

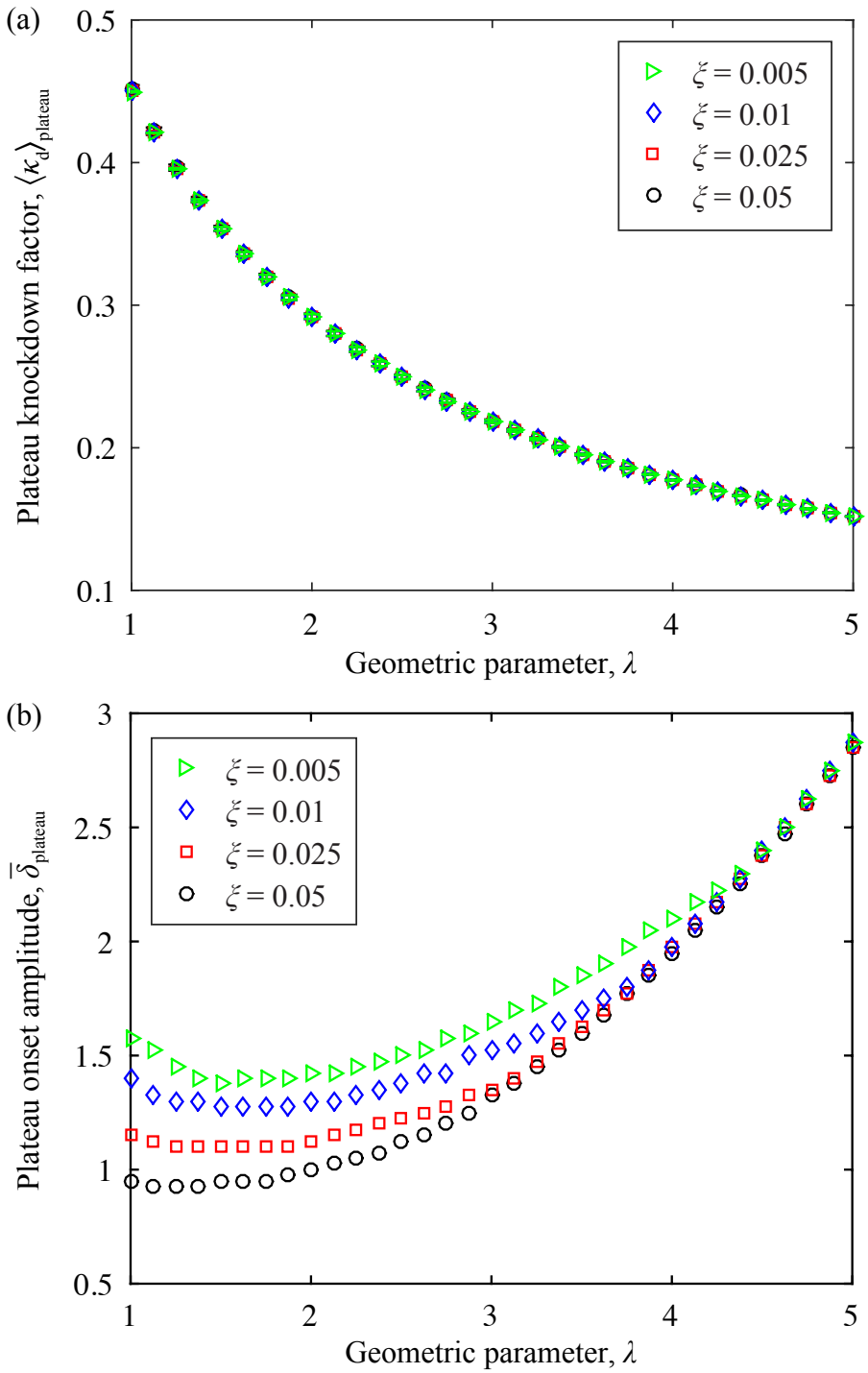

Figure 3-8: **Quantitative characteristics of the plateau.** (a) Pressure level of the plateau versus the geometric parameter, λ, of the defect. (b) Normalized defect amplitude at onset of the plateau versus λ. The various values of the threshold, ξ, used to define the plateau are provided in the legend.

where ξ is a threshold whose sensitivity is evaluated by choosing different values, $\xi = \{0.005, 0.01, 0.025, 0.05\}$. In Fig. 3-8(a), we plot $\langle \kappa_d \rangle_{plateau}$ versus λ and find a monotonic decrease, from $\langle \kappa_d \rangle_{plateau} = 0.45$ at $\lambda = 1$, down to $\langle \kappa_d \rangle_{plateau} = 0.15$ when $\lambda = 5$. The level of the plateau is insensitive to the chosen values of ξ with a variation of at most 0.35% across the four cases.

Figure 3-8(b) plots the onset of the plateau, $\bar{\delta}_{plateau}$, as a function of λ. For small defects in the range $\lambda < 2$, $\bar{\delta}_{plateau}$ is approximately constant, but with a value that depends on the choice of ξ. As λ is increased, $\bar{\delta}_{plateau}$ also increases but the curves with different values for the thresholds converge. Overall, we conclude that the plateau starts when the amplitude of the imperfection is at least larger than the shell thickness ($\bar{\delta}_{plateau} \gtrsim 1$).

3.9 Summary and outlook

We have reported results from experiments on the critical buckling load of spherical elastic shells under uniform pressure loading, with an emphasis on how their knockdown factors are affected by an engineered 'dimple-like' imperfection. A fabrication method was developed to produce elastomeric spherical shells containing a single defect with geometric properties that could be accurately controlled and systematically varied. Precision experiments were performed to measure the critical pressure for the onset of buckling for these shells. The experimental results showed a direct relationship between the critical buckling pressure and the geometry of the imperfection, the amplitude and angular width. In addition, FEM simulations and ODE numerical analyses were conducted by collaborators, showing excellent quantitative agreement with each other and with experiments. To the best of our knowledge, this is the first time that experimental results on the knockdown factors of imperfect spherical shells have been accurately predicted.

Our study is well aligned with efforts currently underway by NASA and others interested in large shell structures to replace the old empirical knockdown factors employed in design codes by an approach that: (i) first, measures the topographic

distributions of imperfections, (ii) then, predicts buckling loads from the measured data, and (iii) finally, determines the corresponding knockdown factors (Hilburger et al., 2006; Hilburger, 2012). In contrast to a statistical approach that starts from measuring uncontrollable imperfections, here we have precisely and systematically controlled a single geometric imperfection and showed that the associated knockdown factors can be predicted.

Furthermore, we found a buckling plateau for large amplitudes of the imperfection by extensively varying the amplitude in experiments, which was a scope receiving no attention in previous numerical studies. We also presented the results of FEM simulations and ODE solutions to characterize the plateau. Both the level of the plateau and its onset are functions of a single geometric parameter set by the angular width of a defect and the radius to thickness ratio of the shell. Existing experimental data collected from the literature on the buckling of spherical shells (Fig. 1-2) provides an indication that the plateau may be connected to the apparent lower limit of the ensemble of historical buckling data. This suggests that replacing the current empirical lower limit curves (Samuelson & Eggwertz, 2003) by a deterministic framework may be a goal worth pursuing.

Chapter 4

Buckling of hemispherical bilayer shells with residual swelling

In this chapter, we introduce a new class of hemispherical shells that can self-repair or self-aggravate existing geometric imperfections. We fabricate these bilayer shells by coating hemispherical molds, which itself contain a single geometric defect, with two different polymeric liquids. Upon curing, the coating process yields an elastic shell with an imposed geometrical defect in the initial stress-free configuration. Within the bilayer structure, uncross-linked residual polymer chains in one of the layers diffuse into the other fully cross-linked layer. As a result, this diffusion process leads to a variation of the volume of each layer and, consequently, the natural curvature of the shell evolves. This time-varying natural curvature can have a positive or a negative value depending on the order of the coating of the polymeric liquids. In turn, the evolution of the natural curvature of the shell can change the geometry of the defect and, hence, modulate the critical buckling pressure.

In Sec. 4.1, we describe the motivation and provide a literature review for this problem. Then, the natural curvature and mechanical properties of bilayer structures are characterized in Sec. 4.2. We describe experimental method and quantify the time evolution of the knockdown factor in Sec. 4.3 and 4.4, respectively. The deformation of bilayer shells is investigated in Sec. 4.5. The thickness variation is analyzed further in Sec. 4.6. Finally, the effective thickness and modulus are discussed in Sec. 4.7.

4.1 Motivation and literature review

As described in Chapter 1, it is now well established that the critical buckling load of shells is highly sensitive to geometric imperfections (Sec. 1.1). In addition, the results from our experiments and simulations in Chapter 3 showed that a small defect could cause a substantial decrease in the buckling strength of the shell. Motivated by low knockdown factors collected from historical experimental studies (Fig. 1-2), we sought to develop the proof of concept for a systematic and robust method to improve the buckling strength of an imperfect shell.

There are various strategies to strengthen the shell, such as: rib stiffening (Meyer & Bellingante, 1964), fiber reinforcing (Song & Hwang, 2004; Sagis et al., 2008), and the multilayer structures (Noor et al., 1996; Sagis et al., 2008). Sandwich shells, which are multilayered structures consisting of stiff facings bonded to a flexible core, combine light weight with high stiffness and have been widely used in aerospace, ship, and construction (Noor et al., 1996). A variety of configurations have been used for the cores, including solid low-density materials, high-density materials in cellular form, and high-density materials in corrugated form (Noor et al., 1996). Rib-stiffening has an old history in architecture since the 6th century (see Fig. 4-1(a)) and such structural strategies were suggested as a replacement for the sandwich structure of common domes and bulkhead (see Fig. 4-1(c)) that have difficulties in their fabrication and inspection (Meyer & Bellingante, 1964; Adam & King, 1965). Mechanical tests of a variety of types of stiffening mechanisms for shells (including meridional, circumferential, combined meridional and circumferential, square-grid, and geodesic stiffening), have demonstrated high knockdown factors $0.82 \leq \kappa_{\mathrm{d}} \leq 2.27$ (Meyer & Bellingante, 1964). In this tests, the buckling pressure was normalized by the classical buckling pressure of an un-stiffened shell with the same weight. As a more effective strategy, fiber-reinforced materials have been increasingly used to construct an entire shell structure, as well as a part of the layers in a multilayer structure (Mallick, 2007). At the large scale, steel-reinforced concrete is widely used in architecture (see Fig. 4-1(b)). For example, adding steel fibers at 2% volume fraction can improve the

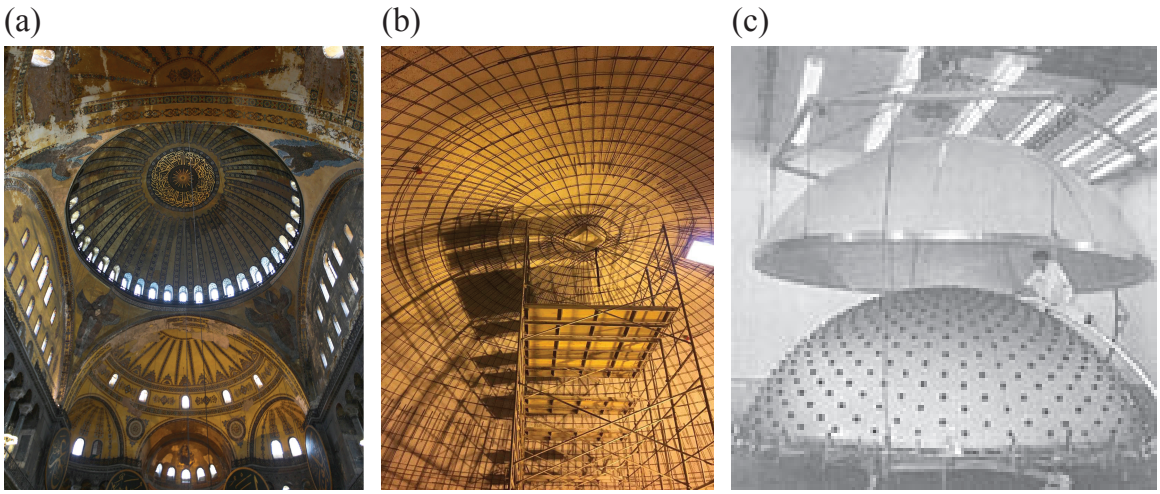

Figure 4-1: **Examples of strengthened spherical shells.** (a) Ribbed dome of the Hagia Sophia, located in Istanbul (Steve Evans, 2011). The original un-stiffened dome was collapsed after the earthquake of 558, and later in 563, a new dome was built with ribs (Maistone, 1988). (b) Steel reinforcing rebar of a dome (Javier Figueroa, 2016). (c) Sandwich structure of the Saturn V's common bulkhead. Two facing sections are being precisely fitted before insulation (core material) is applied between them (Bilstein, 1999).

tensile strength of concrete by 98% (Song & Hwang, 2004). At the micrometer scale, the mechanical stability of fiber-reinforced microcapsules was found to be superior to that of multilayer capsules (Sagis et al., 2008).

In contrast with the design strategies mentioned above for increasing the buckling strength of shells, multilayered shells have a simpler geometry and, for the purposes of a proof of concept, they can be readily fabricated using our coating technique developed in Chapter 2. Our advantage of solid multilayer shells with constant thickness is that they do not involve complex geometrical features such as ribs, grids, and cells. Therefore, one can build a multilayer shell by coating various polymeric liquids, layer by layer. The use of laminated composite shells is indeed found in many engineering applications (*e.g.*, aerospace and submarine structures), and its usage has expanded rapidly since the 1970s (Qatu, 2004). Nevertheless, there is a lack of data on static stability tests of multilayered doubly curved shells (Błachut, 2009). In this chapter, as a proof of concept, we focus on the simplest form of a multilayer shell: the bilayer

shell. To fabricate hemispherical bilayer shells, we shall use two kinds of VPS polymer liquids that, once cured, have different moduli. The stiffer layer can be made to be on top of the more compliant layer, or vice versa by coating two different VPSs in the opposite order. We will compare the critical buckling pressure of both version of bilayer shells: *stiffer layer on top* and *softer layer on top*.

Recently, it has been found that when two different VPSs (for example, VPS-32 and VPS-8) are bonded together into composite structure, uncross-linked residual polymer chains can diffuse from one layer to the other (Pezzulla et al., 2015, 2016). Figure 4-2 presents the schematic of this diffusion process. During curing, polymerization leaves uncross-linked free chains in VPS-8, and these free chains can migrate across the interface to the fully cross-linked VPS-32. This migration process is driven by the concentration gradient of free polymer chains (Fig. 4-2(a)). The associated mass diffusion results in a variation of the volume of each layer (Fig. 4-2(b)) and these inhomogeneous volume changes, together with geometric confinement, can lead to residual stresses that deform the bilayer structure. The deformation induced by this non-homogeneous swelling is more dramatic if the bilayer structure is slender. Indeed, in thin bilayer structures, the swelling layer is compressed, whereas the shrinking layer is stretched by each other, thereby inducing natural curvature. Pezzulla et al. (2016,

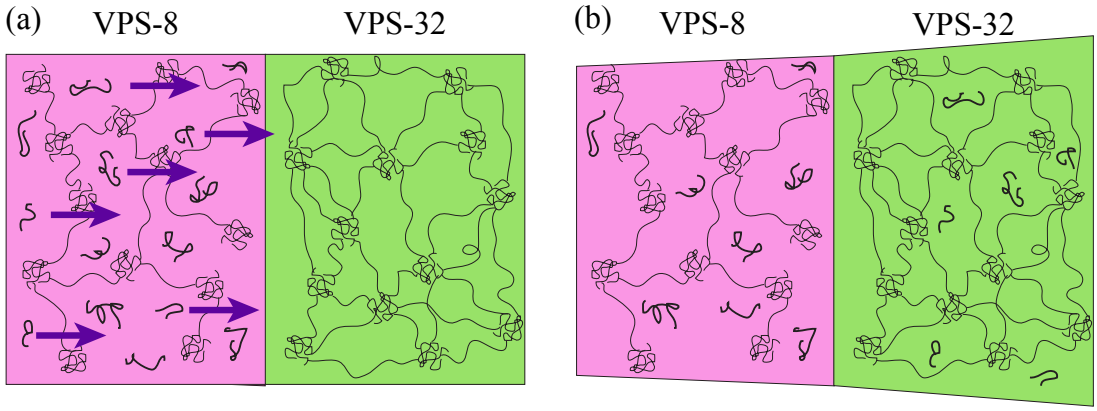

Figure 4-2: **A schematic of residual swelling in a polymer bilayer.** (a) Free chains flow from VPS-8 (pink) to VPS-32 (green) driven by the concentration gradient. (b) The volume of VPS-8 decreases while the volume of VPS-32 increases as a result of residual swelling.

2017) developed a theoretical model that describes the morphing of bilayer thin disks and shells subjected to residual swelling/shrinking, and hence natural curvatures. In their analytical model, the natural curvature was reduced to an effective mechanical load and combined with Koiter's classical shell theory. In this study, the deformation and instabilities in open spherical bilayer shells were investigated through both an analytical model and experiments. Furthermore, their theoretical results suggested that a closed shell can buckle at a critical value for the natural curvature, even in the absence of external pressure.

Deformation of VPS bilayer structures, mentioned above, due to residual swelling is analogous to the thermoelastic mechanism that underlies bimetallic thermostats under temperature changes. When the thicknesses of both metals are equal, the curvature of bimetallic strip is described as (Timoshenko, 1925),

$$k = \frac{24(\alpha_2 - \alpha_1)\Delta T}{h(14 + E_1/E_2 + E_2/E_1)}, \tag{4.1}$$

where α_1 and α_2 are the thermal expansion coefficients of the two metals, E_1 and E_2 are the respective Young's moduli, and ΔT is the temperature change.

Moreover, the thermoelastic stability of *shallow* bimetallic shells is a classic and well-known problem and was studied to determine the buckling temperature at which snap-buckling occurs (Panov, 1947; Wittrick et al., 1953; Timoshenko & Gere, 1961; Aggarwala & Saibel, 1970; Ren-Huai, 1983). Later, Batista & Kosel (2006) studied the thermoelastic stability of the non-shallow bimetallic spherical shell. Furthermore, Rutgerson & Bottega (2002) investigated the buckling behavior of bilayer shells subjected to combinations of uniform temperature change, applied external pressure, and circumferential edge loads. In their model, the thermal moment was such that its direction always assisted the shells to snap-buckle. As a result, the critical temperature of these bilayer shells at which buckling was initiated was lowered by increasing the applied pressure. Similarly, the critical buckling pressure levels were lowered with an increasing temperature change. Hence, the knockdown factor was decreased with the existence of thermally induced stresses. Inspired by this past research on the role of

thermoelastic effects on the buckling of shells, our vision is that altering the direction of the thermal moment or an analog mechanical system could be advantageous for shells to withstand a higher external pressure loading, consequently, increasing the corresponding knockdown factors.

In addition to the role of residual swelling in altering the internal moments, we hypothesized that it could also change the shape of any geometric imperfection in the shell. If the shell is perfectly spherical, the evolution of natural curvature will change its radius, without distorting the overall spherical geometry, before buckling occurs (Pezzulla et al., 2017). However, in practical setting, the shell will not be perfect, and geometric imperfections are inevitable, which will be deformed due to the residual swelling. As such, we envisioned that geometric imperfection could potentially be either repaired or aggravated, depending on the original shape of the imperfection, as well as the sign of the natural curvature that evolves due to residual swelling. Because the buckling of spherical shells is highly sensitive to imperfections, even a small deformation of an existing defect will have a significant effect on the knockdown factor.

The concept mentioned above of repairing a defect is analogous to *self-healing* in synthetic polymeric materials. Self-healing polymers have been developed (White et al., 2001; Brown et al., 2002, 2005), which contain micro-encapsulated healing agents within their bulk. Such polymers exhibit a regenerative ability, but are limited to the repair of a single damage event, at a given location. As an alternative, re-mendable polymers that repair multiple times have also been developed (Chen et al., 2002, 2003), but these require heat treatment and applied pressure. Cordier et al. (2008) synthesized self-healing rubber consisting of molecules that associate together to form both chains and cross-links, via hydrogen bonds. In these materials, when a sample is broken or cut, and the broken surfaces are subsequently brought into contact for some time at room temperature, they self-heal without any heat or pressure treatment. The healing mechanism works because the strength of supramolecular associations are lower than that of covalent bonds; when broken, many non-associated free groups are present near the fracture surface to form bridges across the interface.

Most self-healing studies to date have focused on repairing the damage in the form of cracks that reduce the tensile strength and fatigue life of the structure. For the remainder of this chapter, we shall apply a similar concept of self-healing to geometric imperfection in the shell that significantly reduce the knockdown factor, which, to the best of our knowledge, has not yet been done.

For this chapter, we have fabricated bilayer shells with two different polymers, VPS-8 and 32, where free chains diffuse across the interface from the softer (VPS-8) to the stiffer (VPS-32) polymer and induce residual swelling. The time-varying natural curvature of our bilayer shells can have a positive or a negative value, depending on the order of the coating of the polymeric solutions. The objective of this study is to investigate the buckling pressure of bilayer shells with a geometric imperfection while their natural curvature varies due to residual swelling and seek to find the mechanism that underlies the increase or decrease in buckling pressure.

4.2 Characterization of VPS bilayer structures

Before manufacturing spherical bilayer shells, we first investigated the evolution of the natural curvature of rectangular bilayer beams. We will investigate the relation between the evolution of the natural curvature and the thickness of the bilayer. Then, we will employ the knowledge on the time scale of the evolution of the natural curvature to select the appropriate length-scale for bilayer shells, as well as the time-scale for the measurement of the buckling pressure.

For this purpose, we fabricated a thin bilayer plate using a spin-coater. The thickness of the spin-coated film can be predicted from Eq. (1.8), which can be reduced when $4\rho\Omega^2 h_{\mathrm{i}}^2 t/3\mu \gg 1$ as

$$h \approx \left(\frac{2}{3}\frac{\mu_0}{\rho\Omega^2 t}\right)^{1/2}, \tag{4.2}$$

where Ω is the rotating speed, and t is the rotating time. In Fig. 4-3, we plot experimental data of film thickness as a function of the rotation speed. The initial viscosities, $\mu_0 = 0.05$ Pa.s for VPS-8 and $\mu_0 = 0.1$ Pa.s for VPS-32, which are un-

known at high shear rates, were estimated by fitting Eq. (4.2) to experimental results. The parameters used in our experiments with estimated μ satisfy $4\rho\Omega^2 h_i^2 t/3\mu \gg 1$.

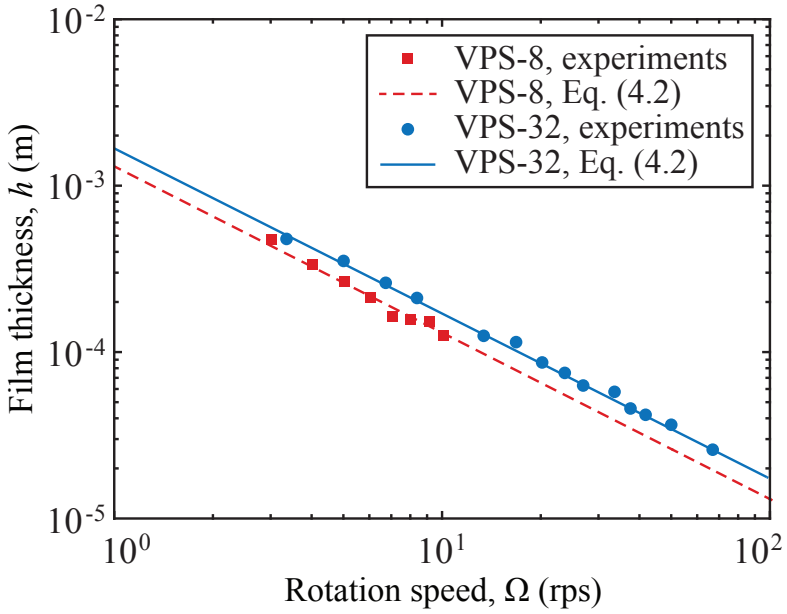

Figure 4-3: **Relation between rotation speed of spin coating and film thickness.** Experimental data of the final film thickness, h, versus rotation speed, Ω of VPSs, spin-coated with constant acceleration (1000 rpm/s) for rotating time $\tau_{\text{rot}} = 20$ s. VPS-8 (red squares) has $\rho = 993$ kg/m^3, and $\mu_0 = 0.05$ Pa.s was estimated by fitting Eq. (4.2) (dashed line). VPS-32 (blue circles) has $\rho = 1160$ kg/m^3 and estimated $\mu_0 = 0.1$ Pa.s that was obtained from Eq. (4.2) (solid line).

As the first step towards fabricating the bilayer plate, VPS-32 was first mixed with a base/cure ratio of 1:1 in weight, for 10 s at 2000 rpm (clockwise), and then 10 s at 2200 rpm (counterclockwise). Then, liquid VPS-32 was immediately spin-coated at 260 rpm for 20 s with constant acceleration (1000 rpm/s) onto an acrylic plate of radius $R = 38$ mm and cured to produce a thin plate of thickness $h_1 = 0.3$ mm. Secondly, we mixed VPS-8 with the same protocol for VPS-32 and spin-coated onto the fully cured VPS-32 film at 340 rpm for 20 s with constant acceleration (1000 rpm/s). After the curing time, $\tau_c = 479$ s, of VPS-8 from the moment of end of the mixing, we set a timer and then cut off a rectangular strip from the bilayer film with the thickness $h = 0.6$ mm, width $w = 3$ mm, and length $l = 10$ mm. We clamped the thin bilayer beam and took photographs as shown in Fig. 4-4(a). The direction

of the gravity force is perpendicular to the deformation plane.

From digital photographs, we fitted a circle to the mid-surface of a bilayer beam. The curvature of bilayer beam is defined as $k = 1/R$ with the radius of the fitted circle R. In Fig. 4-4(b) we plot the curvature, k, of the bilayer beam as a function of time, t. Solid circles are experimental data. The curvature evolution can be expressed as

$$k = k_{\mathrm{f}}(1 - e^{t/T}), \tag{4.3}$$

where k_{f} is the final curvature once steady state has been reached, and T is the characteristic time constant due to the diffusion process across the interface. The final curvature $k_{\mathrm{f}} = 0.2300 \pm 0.0022$ mm^{-1} was measured a day after the beam was fabricated. The diffusion time constant was measured to be $T = 47 \pm 1$ min (with 95% confidence bounds) by fitting a straight line to a semilogarithmic plot of $1 - k/k_{\mathrm{f}}$ versus t, as shown in Fig. 4-4(c).

Our collaborators, Matteo Pezzulla and Douglas P. Holmes (Boston University) collected the data on the dynamics of these beams at room temperature ($\approx 22^{\circ}C$). In Fig. 4-5, we plot these experimental data (circles) of the diffusion time constant, T, versus the film thickness, h. A straight line was fitted to the data, $\log T = 2.2 \log h + 4.7848$ (solid line). These results are consistent with time lag in diffusion through a plate, which has been shown to scale as (Frisch, 1957),

$$T \approx h^2/D, \tag{4.4}$$

where D is the diffusivity. Our experimental data is in reasonable agreement with this equation (dashed line), with $D = 0.0070 \pm 0.0002$ mm^2/min (with 95% confidence bounds). From Eq. (4.4), with $h = 0.6$ mm, the time constant is therefore predicted to be $T = 51$ min, which is close to the experimentally measured value of $T = 47$ min (red square), mentioned above. These results indicate that the diffusion time scale is much larger than the curing time scale of the VPS polymers: $\tau_{\mathrm{c}} = 469 \pm 7$ s for VPS-8 and 574 ± 11 s for VPS-32. Moreover, measuring characteristic quantities of the shells (*e.g.*, shape and buckling pressure) at intervals of approximately 5 min,

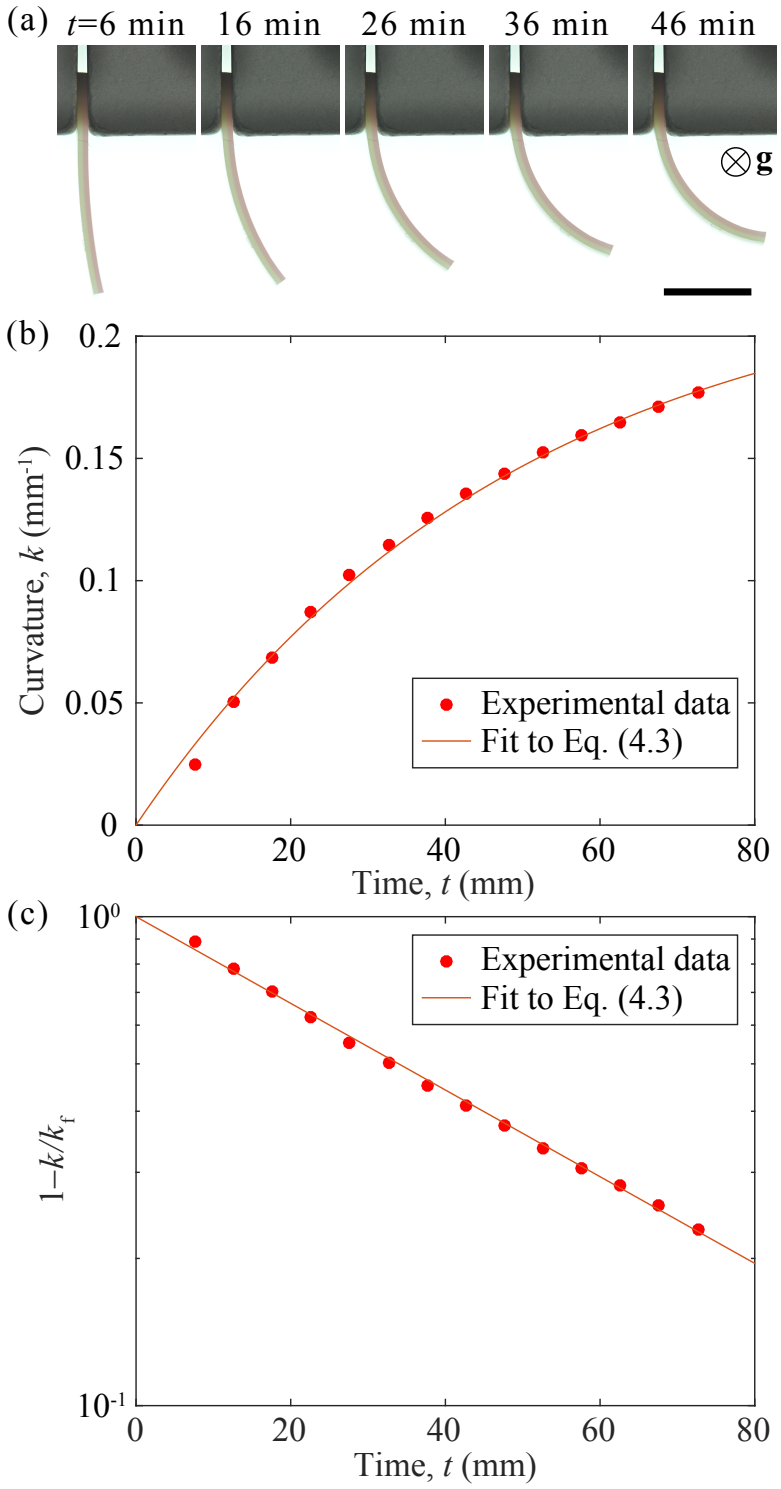

Figure 4-4: **Deformation of a bilayer beam due to residual swelling.** (a) Photographs of a bilayer beam with the thickness, $h = 0.6$ mm. The time interval between each frame is 10 min. Scale bar, 5 mm. (b) Time evolution of the curvature of the bilayer beam, $k(t)$. (c) Plot of $1 - k/k_\mathrm{f}$ as a function of time, t. The solid lines correspond to fits of the Eq. (4.3) with $k_\mathrm{f} = 0.2300 \pm 0.0022$ mm^{-1} and $T = 47 \pm 1$ min.

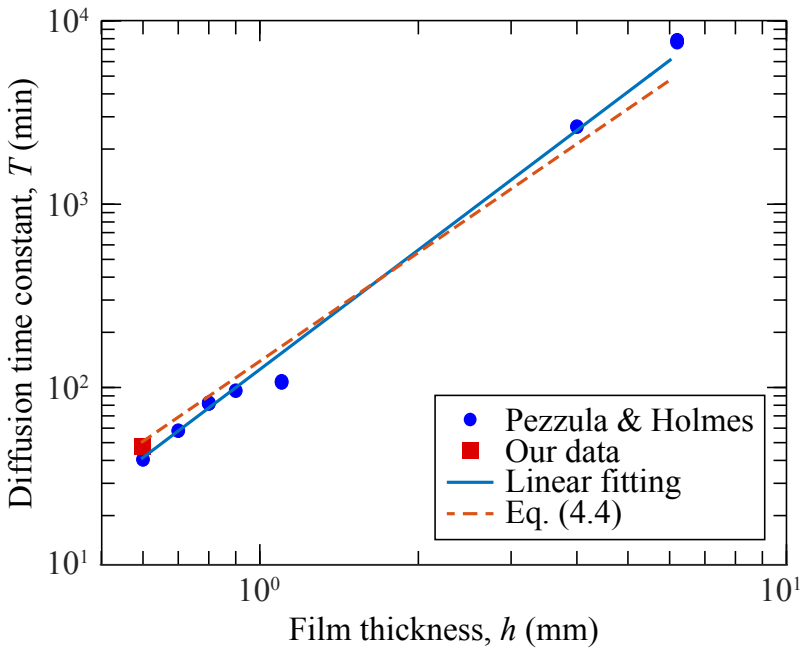

Figure 4-5: **Relation between the diffusion time constant and the bilayer film thickness.** Experimental data obtained by Matteo Pezzulla and Douglas P. Holmes (blue circles) were plotted and fitted with straight (solid) line and Eq. (4.4) (dashed line). Our data point (red square) is on both fitting lines.

would provide sufficiently dense data to represent the time evolution of the process.

In collaboration with Matteo Pezzulla and Douglas P. Holmes, we also characterized the time evolution of the mechanical properties of the bilayer beams. The Young's modulus, E, of the bilayer beam was measured by tensile test. The Instron 5943 mechanical testing system was used with a 500 N load cell. The specimen had a dog-bone shape with a length $l = 100$ mm, width $w = 10$ mm, and thickness $h = 2$ mm. The measurements were repeated every 30 min. The test results are plotted as a function of time in Fig. 4-6(a). We also measured the bending stiffness, K, of the bilayer beam. To do so, we positioned the bilayer beams in two different orientations to include or exclude the gravity effect on the deformation as in Figs. 4-6(b1) and (b2), respectively. From the digitized images of the beam deforming without gravity effect, we measured natural curvature. The elastica equation with gravity and natural curvature was solved numerically, and the value of K was determined that provided the best fit between the numerical solution and the experimental profile of the beam

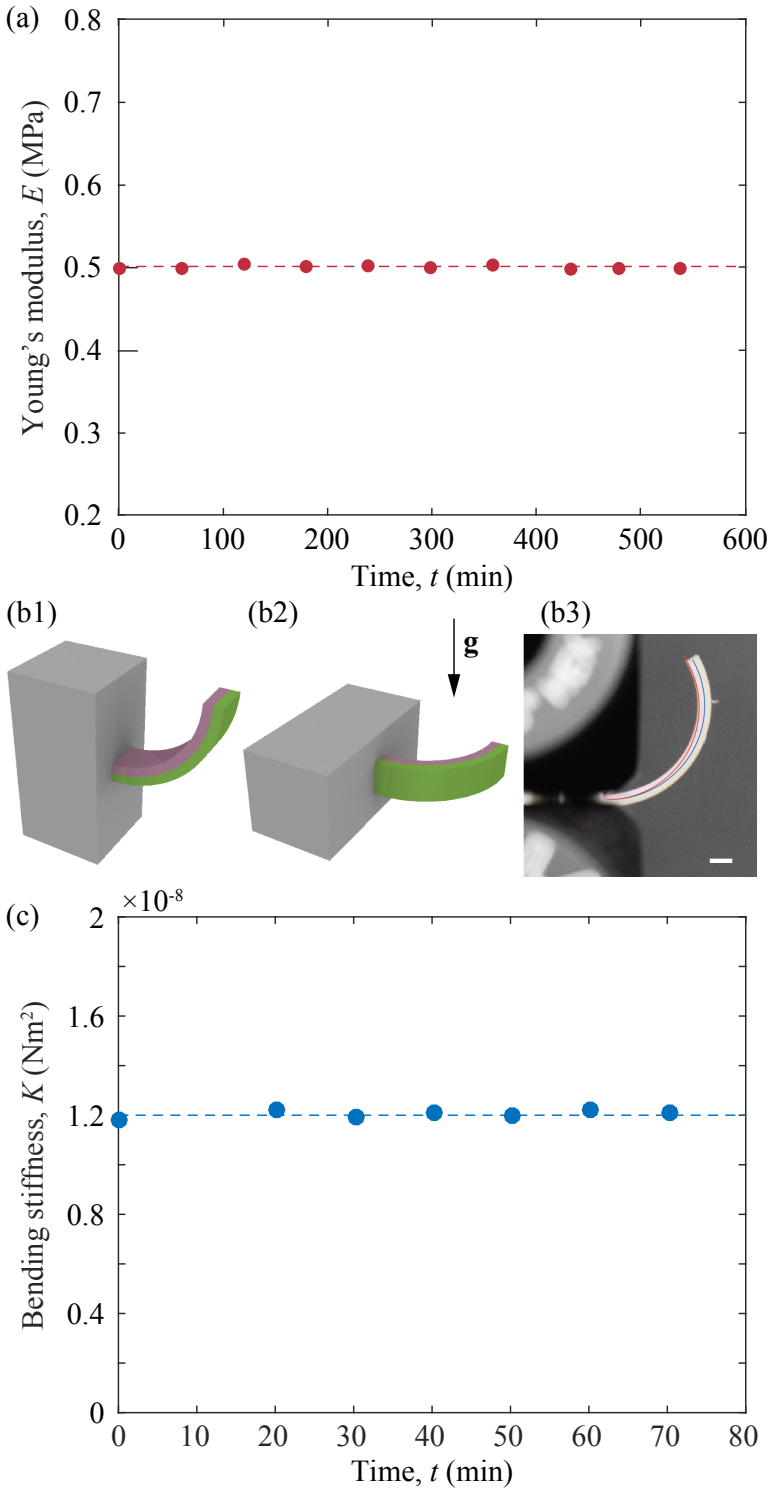

Figure 4-6: **Mechanical properties of a bilayer beam.** (a) Young's modulus, E, versus time, t. (b) Schematics of a bilayer beam whose middle surface deforms (b1) with and (b2) without gravity. (b3) Fitting curves of a beam without gravity (red) and with (blue) gravity were stacked on top of a photograph of a beam deforming with gravity effect. Scale bar, 1 mm (c) Bending stiffness, K, of a bilayer beam as a function of time.

deforming with gravity effect. The equation in terms of dimensionless quantities is given by

$$\theta(s)'' - \frac{1-s}{\beta}\cos\theta(s) = 0, \tag{4.5}$$

where θ is the angle of the tangent vector with respect to the horizontal axis, s is the dimensionless arc-length, and β is a dimensionless parameter defined as $\beta = K/(\rho g S L^3)$, where ρ is the density, S is the cross sectional area, and L is the length of the elastica. Without gravity, β goes to infinity, and the solution of the equation is a segment of a circle. Under gravity, the value of β that best fits the experimental profile was found, which gives the value of K. The natural curvature defines the boundary condition on the free end: $\theta'(1) = \alpha$, where $\alpha = Lk$. In Fig. 4-6(b3), the natural curvature (red curve) obtained from the profile of the beam that deformed without gravity effect and the profile of the beam that deformed under gravity (blue curve) were presented. In Fig. 4-6(c), the bending stiffness, K, is plotted as a function of time. We found that over time both $E = 0.50 \pm 0.03$ MPa and $K = 1.20 \pm 0.02 \times 10^{-8}$ Nm^2 are constant to within 1.7% (MAD) over time.

4.3 Experimental methods

In this section, we describe the fabrication method of hemispherical bilayer shells and detail how we measure their critical buckling pressure. We shall first connect the coating technique developed in Chapter 2 to how we fabricated our bilayer shells. To seed a defect in the shell, we first manufactured flexible molds with a flat defect at their pole. Then, we coated two different VPS polymers on these flexible molds, one by one, to build the bilayer. The obtained bilayer shells had a designed defect at their pole and were closed at their base and along the equator to enforce clamped boundary condition. Finally, we will describe the procedure that we followed to measure the buckling pressure as a function of time.

4.3.1 Fabrication of hemispherical bilayer shells

We first fabricated *thick* elastic shells using PDMS, and then used these PDMS shells as molds to finally obtain our desired thin bilayer shells made with VPS-8 and VPS-32. We shall first describe how these PDMS molds were produced.

In Fig. 4-7, a series of schematic diagrams illustrates the various steps involved in the fabrication process of the PDMS molds containing a geometric defect. We have decided to include a defect in the shells in order to be able to quantify the effect of residual swelling on the shape of the defect and, consequently the knockdown factor. In Chapter 3, we found that our shells without a defect buckled at $\kappa_{\mathrm{d}} = 0.69 \pm 0.06$ due to uncontrollable imperfections. Note that without a seeded defect, the experimentally measured knockdown factor cannot be predicted by FEM. Moreover, uncontrollable imperfections could be either repaired or aggravated and have significant effects on the knockdown factor in an unpredictable manner. By including an engineered defect, we will be able to quantitatively investigate how residual swelling affects this geometrical defect, thereby dictating the knockdown factor.

We recall that in Chapter 2, we developed fabrication method of thin spherical shells by coating polymeric liquid on spherical molds. Then, in Chapter 3, we first fabricated flexible hemispherical molds and then indented the mold while polymeric liquid cured inside of that mold, to obtain thin shells with a defect. By varying the indentation amplitude we were able to make shells containing various defects. For

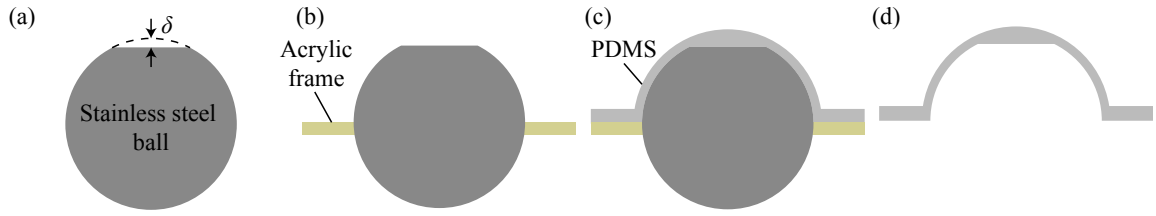

Figure 4-7: **Fabrication process of a PDMS mold.** (a) A stainless steel ball was machined to have a flat defect with the amplitude δ and (b) put on a hole in an acrylic plate with the radius slightly smaller then the radius of the sphere. (c) Liquid PDMS was poured onto the sphere, and (d) cured PDMS shell was peeled from the ball.

the experiments reported in the current chapter, we manufactured flexible molds that contained themselves the initial defect because following the process used in Chapter 3 and coating the VPS liquid twice would not have allowed us to set and fix the indentation amplitude of the mold. Instead, to fabricate the mold, we first machined stainless steel bearing balls (304 stainless steel sphere, McMASTER-CARR) of radius of 25.4 mm to flatten their pole with the following amplitudes, $\delta = \{0, 0.1, 0.2, 0.3, 0.4\}$ mm (Fig. 4-7(a)); one value of δ (*i.e.*, defect) per sphere. Secondly, we poured a PDMS mixture onto the machined stainless balls with a waiting time $\tau_w \approx 30$ min (Fig. 4-7(c)). The PDMS base, curing agent, and cure accelerator were previously mixed in a 10:1:2 weight ratio using a centrifugal mixer for 30 s at 2000 rpm (clockwise), and then for 30 s at 2200 rpm (counterclockwise). Curing of the PDMS was performed in a convection oven at 40°C. We repeated pouring and curing of PDMS six times to obtain hemispherical molds with a thickness of $h_{\text{mold}} \approx 2.4$ mm. These molds were thick and stiff enough as not to deform under self-weight. Finally, the thick PDMS shells were peeled from the stainless spheres (Fig. 4-7(d)). The resulting PDMS molds had an inner radius of 25.4 mm and a single flat defect at their pole with the amplitude, $\delta = \{0, 0.1, 0.2, 0.3, 0.4\}$ mm.

Then, we used these thick PDMS shells as molds to fabricate bilayer shells with two different polymers, VPS-8 and VPS-32. In Fig. 4-8, we illustrate the fabrication protocol of bilayer hemispherical shells with clamped boundary conditions. First, one of the VPS solutions was poured onto the concave underside of the PDMS mold and turned upside down to drain the excess polymer and produce a thin lubrication film

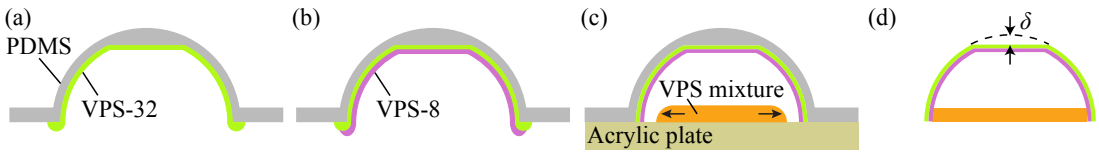

Figure 4-8: **Fabrication process of a bilayer shell** (a) Liquid VPS-32 was coated onto the underside of the PDMS shell. (b) Liquid VPS-8 was coated onto the cured VPS-32 layer. (c) Mixture of VPS-32 and VPS-8 was poured on an acrylic plate, was covered with the shell, and spread. (d) The VPS bilayer shell was peeled from the PDMS shell and has a flat defect at the pole.

(Fig. 4-8(a)). After the first layer of VPS cured, the other VPS solution was poured and drained to produce the second inner layer (Fig. 4-8(b)). During the coating of both VPSs, small droplets formed on the bottom surface of the PDMS mold as illustrated in Fig. 4-8(a-b). After the second layer of VPS solution cured, the excess polymer on the bottom surface of the mold was cut out using a scalpel. We enforce that each layer has the same thickness, $h_1 = h_2 = 0.3$ mm, using the technique to tune the thickness developed in Sec. 2.9. By delaying the pouring time from the moment of preparation of VPS liquid, the shell thickness can be tuned. Then, we added a circular plate at the equator to close the shell and fix the boundary along the equator, otherwise the shell would deform due to swelling and break the symmetry (Pezzulla et al., 2017). To do so, we poured a mixture of VPS-8 and VPS-32 with a ratio 1:1 onto the acrylic plate and covered the puddle of this mixture with the shell (Fig. 4-8(c)). The puddle of VPS mixture gradually spread until the leading edge met the shell at its equator, which, upon curing, formed a thicker band (≈ 2 mm thickness) at the equator that ensured the clamped boundary condition. For this base plate of the shell, we used a VPS-8 and VPS-32 mixture to minimize the effect that the base plate has on the residual swelling of bilayer shell. Had we used pure VPS-8 or VPS-32 as a material of base plate, we would have observed significant diffusion between the shell and base plate. We measured and compared the natural curvature of an open bilayer shell (without base plate) and closed (with base plate) one and found no difference between them, which reveals that the base plate did not affect the residual swelling of the shell. Finally, the bilayer shell closed with the plate was peeled from the PDMS shell (Fig. 4-8(d)). The produced shell could have the swelling layer (VPS-32) on top or the shrinking layer (VPS-8) on top, depending on the order of coating of each polymeric liquid during the fabrication process.

We fabricated multiple bilayer shells with different values of the amplitude of the defect, $\delta = \{0, 0.1, 0.2, 0.3, 0.4\}$ mm, and VPS-32 versus VPS-8 ordering but fixing the radius, $R = 25.1$ mm, and the total thickness, $h = 0.6$ mm, which yields a radius to thickness ratio of $\eta = R/h = 42$. This value of η does satisfy the condition for a thin shell $\eta \geq 20$ (Ventsel & Krauthammer, 2001), but our shell is still much thicker than

the shells used in other experiments introduced in Chapter 1 ($\eta > 70$); see Fig. 1-2. However, if the thickness of shell was to be decreased, the diffusion time scale would decrease steeply ($T \sim h^2$, see Sec. 4.2) so that it would become difficult to investigate the time-evolution of the knockdown factor. For example, for $\eta = R/h = 100$ with $R = 25.1$ mm and $h = 0.251$ mm, the corresponding diffusion time constant would be $T = 9$ mim.

4.3.2 Measuring the critical buckling pressure of the bilayer shells

We pneumatically loaded the bilayer shells and measured the buckling pressure of each shell following the same procedure as in Chapter 3. First, the shell was mounted onto an acrylic plate with a hole at its center and connected to both a syringe pump and a pressure sensor. The air inside the shell was extracted at the imposed constant flow rate of 0.1 ml/min for 1 min and then injected back into the shell with the constant flow rate of 0.1 ml/min for 1 min. For each shell, we repeated these measurements as a function of time to obtain time evolution of the critical buckling pressure. This air extract-inject process was repeated every five minutes by programming the syringe pump.

The internal pressure was monitored at an acquisition rate of 1 Hz using the pressure sensor. During the air extracting step, the volume of shell decreased, and the shell buckled showing a minimum value of the internal pressure. Then, the shell deformed further decreasing its volume until the end of air extraction. During the next air injecting step, the deflection was reduced, and finally, the shell returned to the original shape at the end of the air injection. After a 3 min pause, the air extract-inject process was repeated.

4.4 Time dependence of the knockdown factor of the bilayer shells

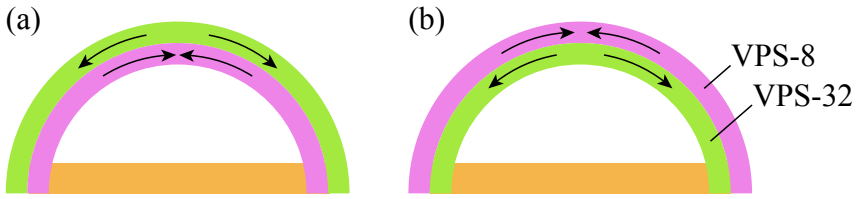

Figure 4-9: **Schematics of two types of bilayer shells.** (a) *Swelling on top* shell consists of VPS-32 (stiffer and swelling) outer and VPS-8 (softer and shrinking) inner layers. (b) *Shrinking on top* shell consists of VPS-8 outer and VPS-32 inner layers.

We proceed by presenting the experimental results of the knockdown factor of our bilayer shells over time. We fabricated two types of bilayer shells as illustrated in Fig. 4-9. One type has VPS-32 outer layer and VPS-8 inner layer (Fig. 4-9(a)), and the other has VPS-8 outer layer and VPS-32 inner layer (Fig. 4-9(b)). The volume of VPS-32 increases and that of VPS-8 decreases because the residual polymer chains in VPS-8 diffuse to VPS-32. At the remainder of this chapter, we will refer to former type as *swelling layer on top* shell and later type as *shrinking layer on top* shell. We shall compare the knockdown factor of each type of shells. Moreover, we will investigate the increase and decrease in the knockdown factor over time due to residual swelling.

In Fig. 4-10, we plot the knockdown factor of our bilayer shells as a function of time. The knockdown factor, κ_{d}, is defined as the maximum pressure, p_{max}, normalized by the classical buckling pressure, p_{c}, for a perfect shell. In Fig. 1-2, we provided historical experimental data of κ_{d} for spherical shells, which showed wide discrepancies in data and investigated the relation between κ_{d} and the amplitude of geometric imperfection in Chapter 3. For a single layer shell, p_{c} was obtained from Eq. (1.1), which is not directly applicable for a bilayer shell. In this Chapter, the critical buckling pressure for a perfect bilayer shell, p_{c}, was obtained by FEM with linear buckling. The FEM simulations in this chapter were conducted through a collaboration with Dong Yan (EPFL). In the FEM simulations, bilayer shells had the same parameters

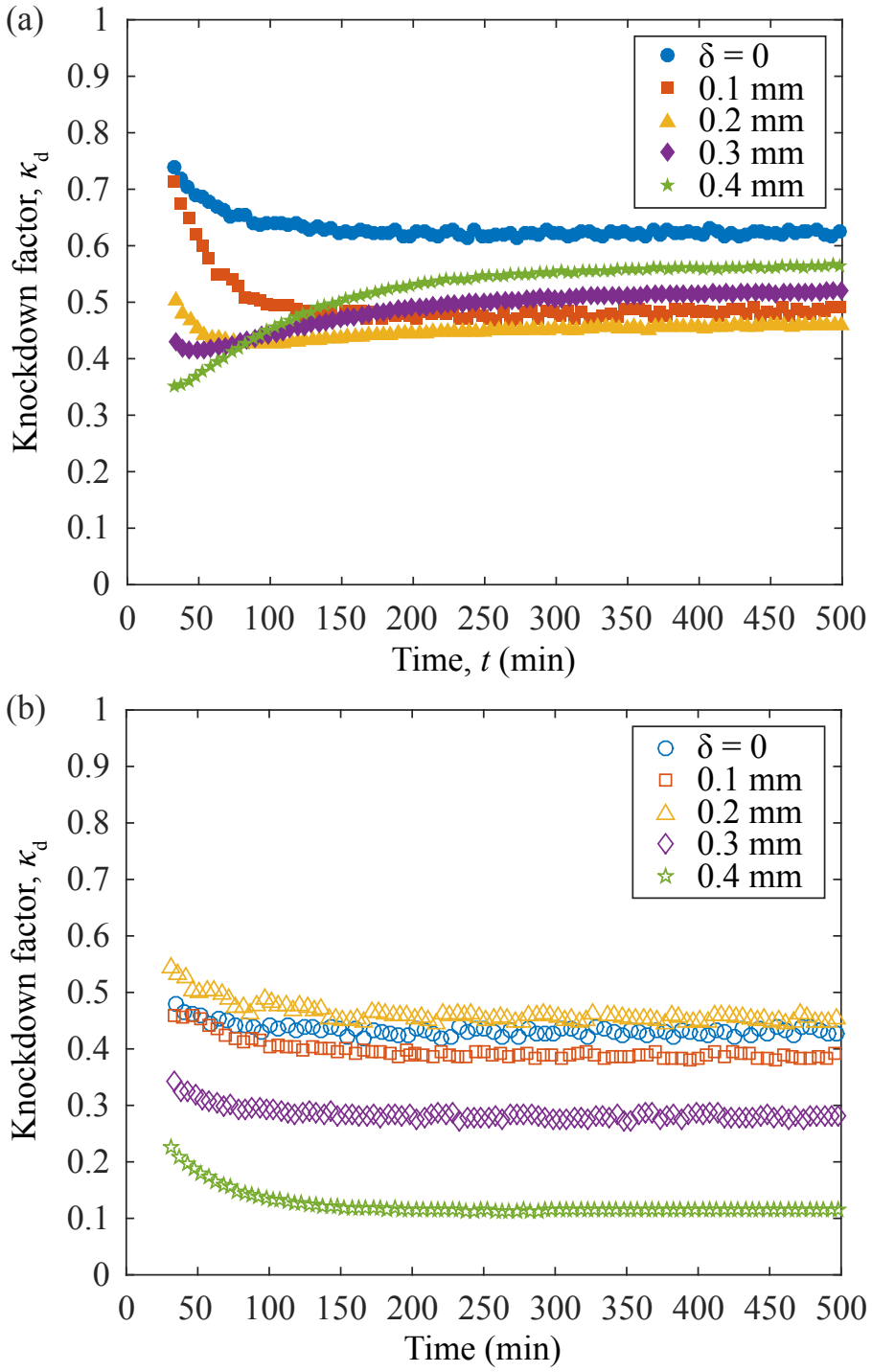

Figure 4-10: **Knockdown factor versus time.** Experimental results of the knockdown factor with (a) *Swelling on top* shells and (b) *Shrinking on top* shells with $R = 25.1$ mm and $h = 0.6$ mm. The amplitude of a flat defect was varied $\delta = \{0, 0.1, 0.2, 0.3, 0.4\}$ mm.

as the shells used in our experiments, but the mass diffusion of free chains was not considered. The shell has the radius, $R = 25.1$ mm, and the thicknesses of each layer were assumed to be constant $h_1 = h_2 = 0.3$ mm. The Young's moduli of each layer were also assumed to be constant over time.

In Fig. 4-10(a) we present the knockdown factor of *swelling layer on top* shells versus time. In the fabrication process, we set a timer after the curing time, τ_c, from the preparation of the VPS liquid that formed the second layer. Immediately after the fabrication, we made a hole at the center of the bottom plate of a closed hemispherical shell and measured the buckling pressure following the method described in Sec. 4.3.2. The data started being obtained at $t \approx 30$ min because the polymerization of the shell and the thicker band at the equator and the preparation to measure the buckling pressure required $t \approx 30$ min. From the experimental data, we found that κ_d can increase or decrease with time, depending on the amplitude of the defect. When the defect was small ($\delta = \{0, 0.1\}$ mm), the knockdown factor first decreased with time from an initial value of $\kappa_d = \{0.74, 0.71\}$ and then reached a steady state $\kappa_d = \{0.62, 0.49\}$. This deterioration of the knockdown factor due to residual swelling was mitigated as δ increased. When the defect size was moderate ($\delta = 0.2$ mm), the knockdown factor decreased at first from $\kappa_d = 0.5$ to the minimum value $\kappa_d = 0.43$ at $t = 80$ min, and then slowly increased reaching a steady state $\kappa_d = 0.46$. When the defect was larger, $\delta = 0.3$ mm, the knockdown factor showed the minimum value $\kappa_d = 0.46$ earlier (at $t = 50$ min) and then increased to the higher steady state $\kappa_d = 0.52$. With the largest defect, $\delta = 0.4$ mm, κ_d continuously increased from 0.35 to 0.56. Note that when the defect is small ($\delta = \{0, 0.1\}$ mm), the other uncontrollable imperfections can have more significant effects on shell buckling.

For *shrinking on top* shells in Fig. 4-10(b), the knockdown factor always decreased with time. When the defect amplitude was small ($\delta = \{0, 0.1, 0.2\}$ mm), the knockdown factor decreased from $\kappa_d = 0.5 \pm 0.04$ to $\kappa_d = 0.42 \pm 0.03$. With the larger defects, both the initial and steady state knockdown factor were lowered. The knockdown factor decreased from $\kappa_d = 0.34$ to $\kappa_d = 0.28$ with $\delta = 0.3$ mm and from $\kappa_d = 0.22$ to $\kappa_d = 0.12$ with $\delta = 0.4$ mm.

In Fig. 4-11(a), we plot the initial (empty symbols) and the final (solid symbols) knockdown factors, κ_{d}, as a function of the normalized defect amplitude, $\bar{\delta}$, for both *swelling layer on top* shells (circles) and *shrinking layer on top* shells (triangles). With the same initial amplitude of the defect, the *swelling layer on top* shells are stronger than the *shrinking layer on top* shells.

For *swelling on top* shells in the initial state (empty circles), the knockdown factor continuously decreases as the defect size increases, which is analogous to the relation between κ_{d} and $\bar{\delta}$ found in Chapter 3. When the steady state is reached (solid circles), the *swelling on top* shells heal the large defect. The knockdown factor first decreases as the defect size increases, and then has the minimum knockdown factor $\kappa_{\mathrm{d}} = 0.46$ at $\bar{\delta} = 0.33$. After the minimum, the knockdown factor increases as the imperfection further increases. The minimum value of $\kappa_{\mathrm{d}} = 0.46$ is much higher than the value of plateau $\kappa_{\mathrm{d}} = 0.2$ found in Chapter 3. On the other hand, the knockdown factor of *shrinking on top* shells generally decreases as the defect amplitude increases both in initial and steady state.

Figure 4-11(b) shows how much the knockdown factor changes from the initial to the final measurement. Specifically, we plot the amount of the knockdown factor change, $\Delta\kappa_{\mathrm{d}} = \kappa_{\mathrm{d,f}} - \kappa_{\mathrm{d,i}}$, versus the normalized defect amplitude, $\bar{\delta}$. *Swelling layer on top* shells (circles) have increasing $\Delta\kappa_{\mathrm{d}}$ (from -0.22 to $+0.21$) with $\bar{\delta}$, while *shrinking layer on top* shells (crosses) have the nearly constant negative $\Delta\kappa_{\mathrm{d}} = -0.08 \pm 0.03$.

In summary of this section, the residual swelling can increase or decrease the knockdown factor of bilayer shells. Small defects in *swelling on top* shells were aggravated by residual swelling. However, large defects ($\bar{\delta} \geq 0.5$) were repaired as the knockdown factor increased, at most, by $\Delta\kappa_{\mathrm{d}} = 0.21$. The minimum knockdown factor of the *swelling on top* shell was $\kappa_{\mathrm{d}} = 0.46$. On the other hand, the knockdown factor of *shrinking on top* shells decreased overtime due to residual swelling by $\Delta\kappa_{\mathrm{d}} = -0.08 \pm 0.03$.

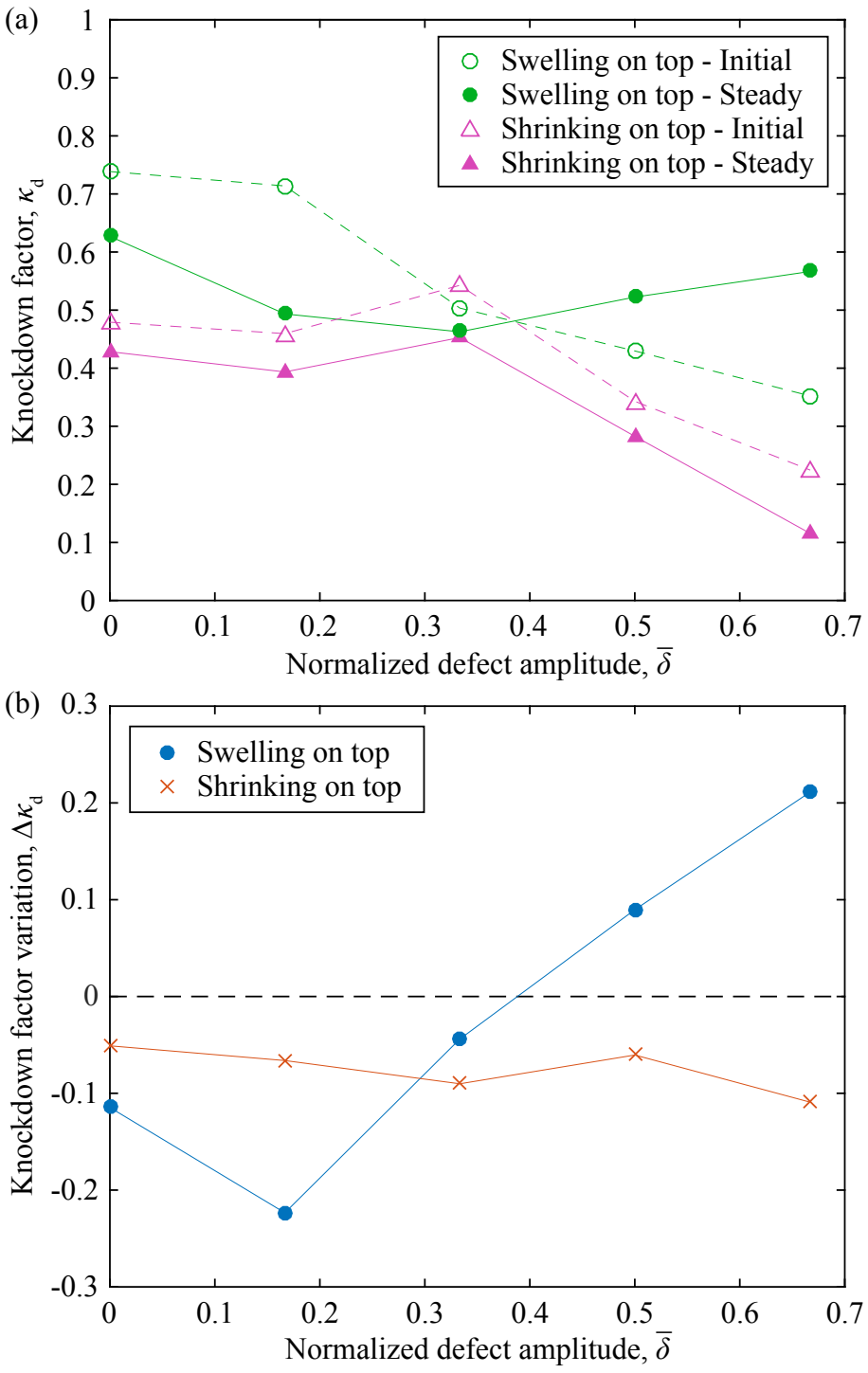

Figure 4-11: **Knockdown factor variation from the initial to the final measurement.** (a) Knockdown factor of *swelling on top* shells (circles) and *shrinking on top* shells (triangles) in initial (empty symbols) and final stage (solid symbols). (b) The amount of the knockdown factor change, $\Delta\kappa_d = \kappa_{d,f} - \kappa_{d,i}$ of *swelling layer on top* shells (circles) and *shrinking layer on top* shells (crosses).

4.5 Characterization of the geometry of bilayer shells due to residual swelling

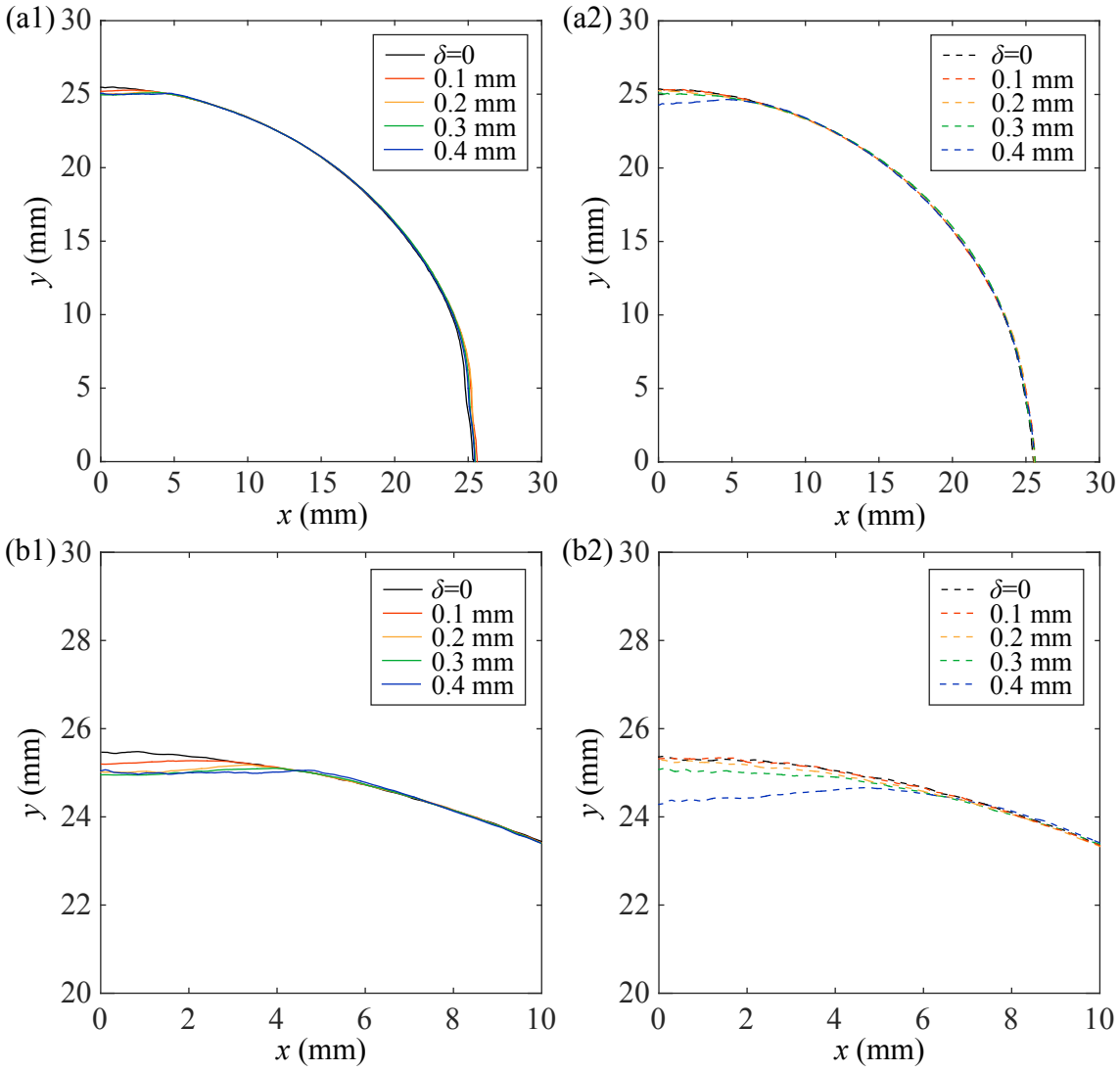

Figure 4-12: **Shape profile of bilayer shells in steady state.** (a) Entire and (b) magnified shape profiles of (1) *swelling on top* shells and (2) *shrinking on top* shells. As the initial amplitude of defect increased from 0 to 0.4 mm, the height of the center of *swelling on top* shells at steady state was varied from 25.37 to 25.04 (by 0.33 mm), and that of *shrinking on top* shells was varied from 25.36 to 24.29 (by 1.07 mm).

Residual swelling changes the natural curvature of bilayer structures. Therefore, this swelling can also change the shape of an existing geometric imperfection. Small

change in the geometry of a defect has a large effect on the knockdown factor. Thus, we investigate the shape of our bilayer shells at the final steady state to verify that the deformation of a defect is indeed the reason of self-healing (increase of the knockdown factor). The shape profiles obtained in this section were used in FEM simulations, which will be discussed in Sec. 4.7.2.

We obtained 3D profiles of the shape of shells at steady state using a desktop 3D scanner (Model 2020i, NextEngine Inc.). We extracted 12 curves at different azimuth angle and averaged these curves, which are plotted in Fig. 4-12.

In Fig. 4-12(a), we plot the full shapes of bilayer shells at steady state. The geometry obtained for different defect amplitude varies near the defect and are almost the same in the remainder of shells. In Fig. 4-12(b), we zoom into the plot to focus on the defect. For the *swelling on top* shells, Fig. 4-12(b1), the large defects of different initial amplitudes $\delta = \{0.2, 0.3, 0.4\}$ mm have the same final amplitudes. Three curves for $\delta = \{0.2, 0.3, 0.4\}$ mm collapse at the pole $(x, y) = (0, 25.5 \pm 0.04)$ mm. As the initial defect amplitude increased from 0.2 mm to 0.4 mm, the defect amplitude in steady state did not increase, showing the same position of center of shells. This is the reason why κ_{d} did not decrease as δ increased from 0.2 mm to 0.4 mm. By contrast, in *shrinking on top* shells, the larger defect grows more showing very low position of center $(x, y) = (0, 24.29)$ mm with initial $\delta = 0.4$ mm, as shown in Fig. 4-12(b2).

4.6 Spatial variation of the shell thickness

The spatial variation of the shell thickness is another type of imperfections, and the thickness of our imperfect shell can be nonuniform in the vicinity of the defect. It is well known that the thickness of a liquid film, flowing over a complex surface, increases at a concave corner (Pozrikidis, 1988; Vlachogiannis & Bontozoglou, 2002). For example, Pozrikidis (1988) numerically analyzed the flow of a liquid film along a periodic wall. A representative case, shown in Fig. 4-13(a), exhibited the minimum thickness at convex corners and the maximum at concave corners. In the same manner, the VPS film may have the maximum thickness at the edge of the defect. In

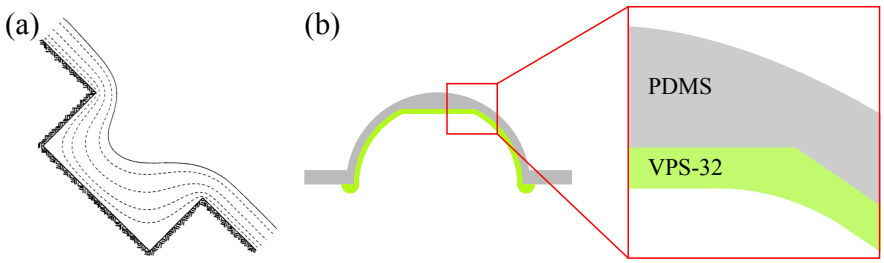

Figure 4-13: **Film thickness increase at a concave corner.** (a) A profile of free-surface (solid line) and streamlines (dashed lines) of a liquid film flowing over a mound, which were obtained by numerical analyses (Pozrikidis, 1988). (b) A schematic of a polymer solution film near the defect.

Fig. 4-13(b), we present a schematic of a VPS film that drains over the inner surface of a PDMS shell containing a flat defect.

To prove this hypothesis, we experimentally measured the thickness profile of bilayer shells with a flat defect. We cut a long strip from the bilayer shell with a defect along a meridian using a scalpel and scanned the cut surface. Figure 4-14(a) is an example of scanned image of a long strip cut from a *shrinking layer on top* shell containing a flat defect with $\delta = 0.3$ mm. We extracted the shell thickness by an edge detection algorithm (image processing toolbox, Matlab).

In Fig. 4-14(b), we plot the shell thickness profiles as a function of the arc length, s, from the pole. The thickness profiles of the left ($s = 0$ to -35) and right side ($s = 0$ to 35) of a long strip were averaged. As representative cases, Fig. 4-14(b) shows the initial and final thickness of *swelling layer on top* and *shrinking layer on top* shells with the defect amplitude, $\delta = 0.3$ mm. *Swelling layer on top* shell and *shrinking layer on top* shell have almost the same thickness profiles, as well as the initial and final thickness profile have no significant difference. The thickness is $h = 0.59 \pm 0.01$ mm at the center ($s = 0$), increases with s, and reaches the maximum $h = 0.67 \pm 0.02$ near the edge of the defect (dashed line). Then, the thickness decreases to 0.6 mm at the remainder of the shell. A steep increase in the shell thickness near the edge of the defect can have a significant effect on the critical buckling pressure.

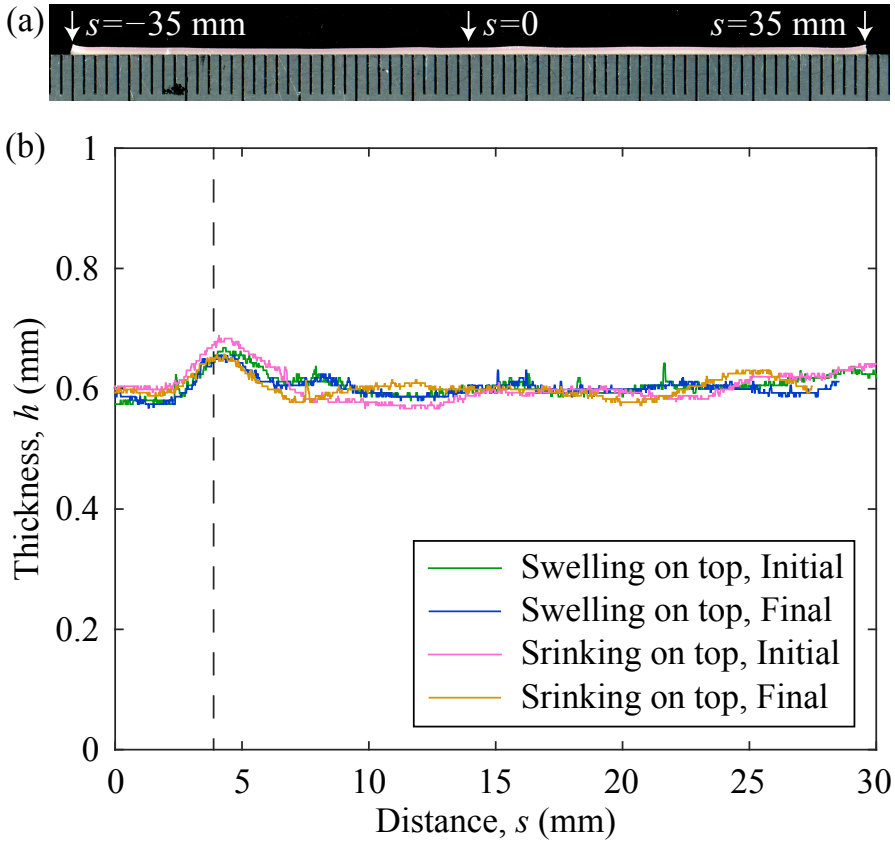

Figure 4-14: **Thickness profiles of bilayer shells.** (a) Scanned image of cut surface of a *shrinking layer on top* shell containing a flat defect with $\delta = 0.3$ mm. (b) Shell thickness profile, h, versus the arc length, s, from the pole. The thickness of both lefthand side and righthand side were averaged. Dashed line is the location of sharp edge of the defect in the mold.

4.7 FEM results for buckling of bilayer shells

Buckling of bilayer shells is also analyzed through FEM. First, bilayer shells with a wide range of the ratio between Young's moduli of two layers are investigated. Moreover, we find that, by appropriate normalization, a bilayer shell can be represented as a single layer shell with effective thickness and modulus. Then, we present results of FEM for knockdown factors of bilayer shells, which was performed with parameters used in experiments. In FEM, we used shapes of shells that were measured by experiments and described in Sec. 4.5. Through all FEM simulations, we do not consider residual swelling.

4.7.1 Normalization with effective thickness and modulus

In this section, a bilayer shell is represented as a single layer shell with effective thickness and modulus. Using these effective properties, buckling parameters of bilayer shells (including the knockdown factor, the amplitude of defect, the geometric parameter) can be normalized. Analyses in this section were conducted in collaboration with Francisco López Jiménez (University of Colorado Boulder).

First, we introduce the effective Young's modulus, $\tilde{E}$, and the effective thickness, $\tilde{h}$, of bilayer structures. In Fig. 4-15(a), a schematic of a bilayer beam is presented. This bilayer beam and the corresponding single layer beam should be identically stretched under the same tensile load. Therefore, the combination of $\tilde{E}$ and $\tilde{h}$ is expressed as

$$\tilde{E}\tilde{h} = E_1 h_1 + E_2 h_2, \tag{4.6}$$

where E_1 and E_2 are Young's moduli of each layer and h_1 and h_2 are the thicknesses of each layer. In the same manner, the bilayer beam and the corresponding single layer beam should identically respond to a moment. Thus, the bending stiffness is derived as

$$K = \frac{E_1}{3}\{(h_1 - d)^3 + d^3\} + \frac{E_2}{3}\{(h_2 + d)^3 - d^3\} = \frac{\tilde{E}\tilde{h}^3}{12}, \tag{4.7}$$

where d is the distance between the neutral axis, which is unknown, and the interface

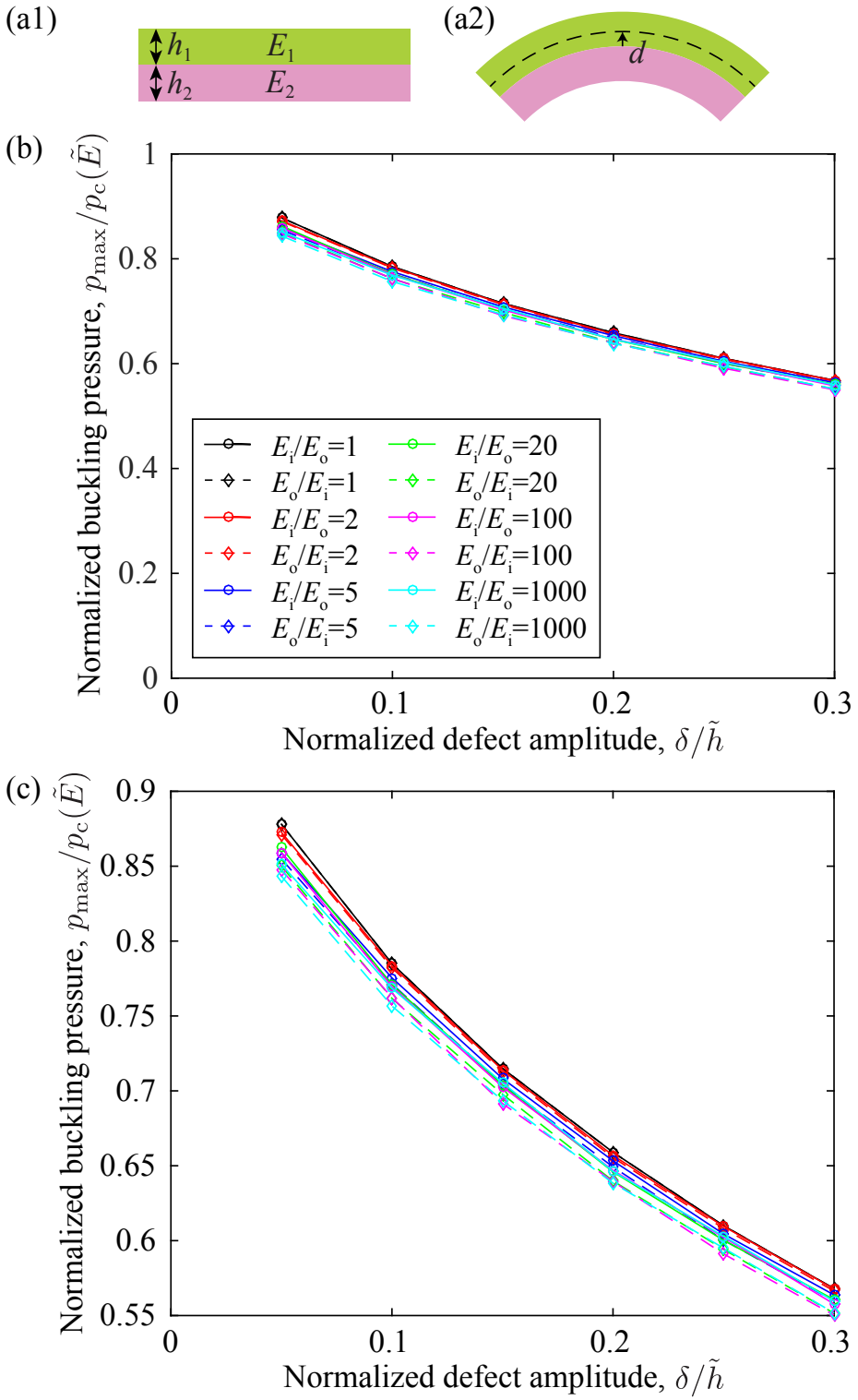

Figure 4-15: **Normalization with the effective thickness and modulus.** (a) Schematics of a bilayer structure (a1) without and (a2) with applied moment. (b) Normalized buckling pressure, $p_{max}/p_c(\tilde{E})$, where $p_c(\tilde{E})$ is the classical buckling pressure calculated with the effective Young's modulus, $\tilde{E}$, as a function of the normalized amplitude of the defect, $\delta/\tilde{h}$. (c) Magnified plot to clearly show the difference between each of curves.

of two layers. When d is the location of the neutral surface, K will have a minimum. Thus, letting $\partial K/\partial d = 0$ gives $d = (E_1 h_1^2 - E_2 h_2^2)/\{2(E_1 h_1 + E_2 h_2)\}$. The effective thickness, therefore, is obtained by substituting d into Eq. (4.7):

$$\tilde{h} = \left[\frac{4E_1\{(h_1 - d)^3 + d^3\} + 4E_2\{(h_2 + d)^3 - d^3\}}{E_1 h_1 + E_2 h_2}\right]^{1/2}. \tag{4.8}$$

Finally, substituting Eq. (4.8) into Eq. (4.6) gives the effective Young's modulus.

To validate that a single layer shell with effective thickness and modulus can represent a bilayer shell, we normalize the buckling pressure of bilayer shells by the classical buckling pressure of the corresponding single layer shell. In Fig. 4-15(b), we plot the normalized buckling pressure, $p_{\max}/p_{\mathrm{c}}(\tilde{E})$, where $p_{\mathrm{c}}(\tilde{E})$ is calculated with the effective thickness and Young's modulus, as a function of the normalized amplitude of the defect, $\delta/\tilde{h}$. The geometric parameter of the defect, λ, that combines the radius to thickness ratio and the angular width of a defect, was fixed at 3. The ratio of Young's moduli of the inner layer to the outer layer was varied in the range $0.001 < E_{\mathrm{i}}/E_{\mathrm{o}} < 1000$. All curves with a wide range of Young's moduli ratio collapse, which means a bilayer shell can be represented as a single layer shell with effective Young's modulus, $\tilde{E}$, and the effective thickness, $\tilde{h}$.

In Fig. 4-15(c), we zoom into the plot to present the effect of Young's moduli ratio on the normalized buckling pressure. As the difference between Young's moduli of inner and outer layer increases, *stiffer layer on top* shell (dashed line) has the lower buckling pressure than *softer layer on top* shell has (solid lines). This might be because the neutral surface of *stiffer layer on top* shell has the larger R that gives the lower buckling pressure ($p_{\mathrm{c}} \sim R^{-2}$).

4.7.2 FEM results with experimentally measured shape of shells

FEM simulations were conducted to predict the experimental results of initial and final knockdown factors. To do that, we used the same geometry and the mechanical

parameters of bilayer shells measured through experiments. We focus on the case of *swelling on top* shells, which have exhibited increasing knockdown factors due to residual swelling. FEM simulations, in this section, were conducted in collaboration with Dong Yan (EPFL).

First, in Fig. 4-16(a), we plot the initial (empty symbols) and the final (solid symbols) knockdown factors, κ_{d}, as a function of the normalized defect amplitude, $\bar{\delta}$, which were obtained from FEM simulations (squares). For direct comparison, we plot again the experimental data presented in Fig. 4-11. FEM results follow the trend found in the experiments. In the initial state, the knockdown factor (empty square) continuously decreases as the defect size increases, and the values show an excellent agreement with experimental data (empty circles). In the steady state, FEM was performed using the shape profiles measured in Sec. 4.5. The knockdown factor first decreases as the defect size increases, exhibits the minimum value of $\kappa_{\mathrm{d}} = 0.40$ at $\bar{\delta} = 0.5$, and then increases as the imperfection further increases. With the shape in the steady state, FEM simulations result in decreased knockdown factor for small defect and increased knockdown factor for large defect, which is the same trend found in the experiments.

Then, in Fig. 4-16(b), we plot the amount of change in the knockdown factor from the initial to the final state. The knockdown factor variation, $\Delta\kappa_{\mathrm{d}}$, obtained from FEM, continuously increases as the defect amplitude increases. However, the value of $\Delta\kappa_{\mathrm{d}}$ was underestimated in FEM simulations. One possibility is that this could be due to the residual stresses that develop during swelling, which were not accounted for in the FEM simulations. We performed supplementary FEM simulations where the thermal expansion was modeled analogous to residual swelling. Then, it was found that the residual stress has insignificant effect on the knockdown factor. For both *swelling on top* and *shrinking on top* shells, the knockdown factor slightly decreases with thermal loads. Another possibility is that the thickness variation of the shells could influence on the knockdown factor.

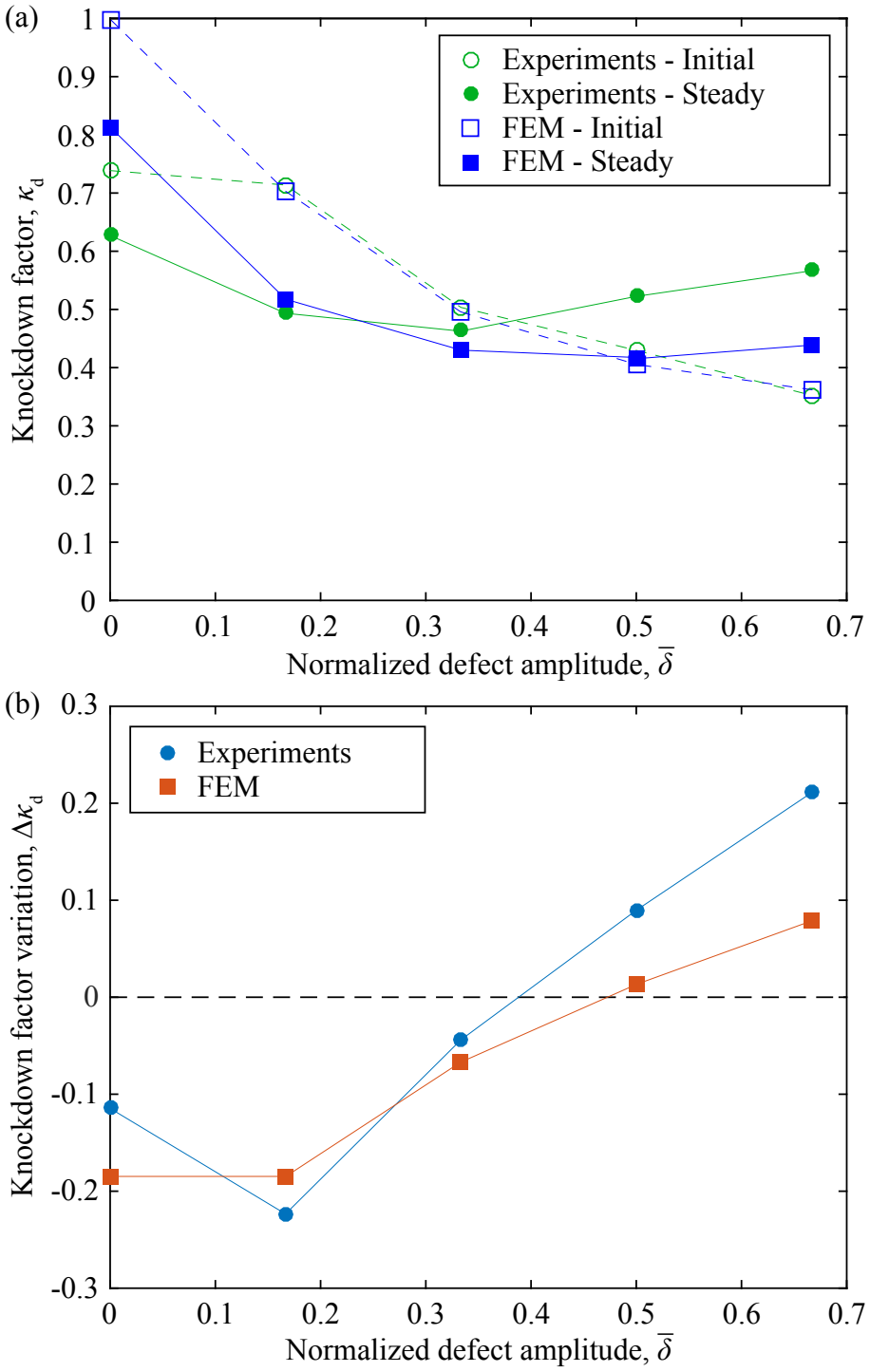

Figure 4-16: **Comparison between experimental and FEM results on the knockdown factor variation from the initial to the final measurement.** (a) Knockdown factor of *swelling on top* shells in initial (empty symbols) and final stage (solid symbols) obtained through experiments (circles) and FEM (squares). (b) The amount of the knockdown factor change, $\Delta\kappa_d = \kappa_{d,f} - \kappa_{d,i}$ of *swelling layer on top* shells: experimental (circles) and FEM (squares) results.

4.8 Summary and outlook

We have reported results from experiments on the buckling pressure of hemispherical bilayer shells, with an emphasis on how their knockdown factors changed due to residual swelling. First, motivated by the thermoelastic buckling of bimetallic shells, we expected the buckling pressure could increase or decrease depending on the direction of residual stresses. Secondly, because residual swelling can change the shape of a defect, we predicted that the knockdown factor would be improved or reduced as the natural curvature evolves, which can be positive or negative depending on the order of polymer coatings.

In the experiments, a fabrication method was developed to produce closed hemispherical bilayer shells that contained a single flat defect. The critical pressure for the onset of buckling for these shells was measured while residual swelling proceeded due to diffusion of free polymer chains. The experimental results showed that *swelling layer on top* shells have the higher knockdown factor than *shrinking layer on top* shells. Moreover, the knockdown factor of *swelling layer on top* shells was found to be able to increase over time due to residual swelling. This 'healing' of imperfections was more effective as the initial amplitude of the defect is larger. In parallel to the experiments, FEM simulations were conducted by collaborators, showing that the change of shape had a role in increase and decrease of the knockdown factor during residual swelling. However, FEM underestimated the amount of 'healing'. A possible reason is that the spatial (steep) variation of the shell thickness significantly affected the knockdown factor. Therefore, we suggest explorations on the effect of thickness variations on the buckling behavior of shells as a potential direction for future research.

Chapter 5

Conclusions

In this final chapter, in Sec. 5.1, we first summarize the main findings of our research. Then, in Sec. 5.2, we suggest possible directions for future research that are motivated by the experimental techniques and results of this thesis.

5.1 Summary of findings

We have presented an investigation into the buckling of thin elastic spherical shells under a uniform pressure load, emphasizing the role of the geometric imperfections. For this purpose, we first developed a novel fabrication technique to manufacture thin elastic spherical shells. Secondly, this coating mechanism was adapted for introducing a designed geometric imperfection in thin spherical shells. Then, we investigated the effect of the geometry of a single defect on the critical buckling pressure of spherical shells. Furthermore, we fabricated bilayer shells that change its shape as a function of time due to the residual swelling and explored the time evolution of the critical buckling pressure of these bilayer shells.

In **Chapter 1**, we introduced the motivation of the thesis and reviewed the literature on the buckling of spherical shells and imperfection sensitivity. We also presented an overview of existing fabrication techniques to produce thin structures via coating . First, we provided a variety of examples of thin spherical shells with length-scales that range from micron to several hundred meter scale found in nature, as well as

engineering applications. Then, we explained the importance of their response to applied loads and provided a collection of historical experimental data on the buckling strength. We focused on the fact that the experimental results of the critical buckling pressure tend to exhibit much lower values than the classical theoretical predictions. We reviewed theoretical studies on the buckling of thin shells, which attempted to rationalize imperfection sensitivity of shells to buckling. For cylindrical shells, since the 1960s, several experimental investigations have been conducted to corroborate the theoretical and computational studies on the imperfection sensitivity . Moreover, recent studies have used designed imperfections to improve the buckling strength and to control the post-buckling behavior of cylindrical shells. However, there has been a striking lack of experimental studies on spherical shells containing systematically varied geometric imperfections. In classic experiments, spherical shells were produced by metal spinning, plastic vacuum drawing, aluminum machining, and electro-forming, most of which resulted in low-quality shells and required empirical improvement to obtain high-quality shells. On the other hand, flat plate and cylindrical shells have been fabricated in laboratory settings through the coating of liquid films that eventually solidify, but these techniques had not yet been ported to spherical geometries. As such, we identified the timely niche for our work to provide much needed experimental data on the imperfection sensitivity of buckling in spherical shells.

In **Chapter 2**, we introduced a simple and robust mechanism to fabricate hemispherical thin elastic shells by the coating, viscous drainage and subsequent curing of polymer solutions on spherical molds. Our process is analogous to spin-coating, which is used to fabricate flat thin films, albeit with a gravity-driven flow instead of centrifugal forces. Through a systematic series of experiments using elastomers, we showed that the dynamics of viscous drainage on a spherical surface could lead to coatings that solidify in time as the polymer cures, thereby leading to a thin elastic shell of nearly constant thickness. A theoretical analysis of the underlying lubrication flow during drainage, which includes the evolution of the rheological properties of the polymer as it cures, was able to accurately predict the final thickness of the shell as a function of the material properties of the polymer and the radius of the spherical

mold substrate. Importantly, the final shell thickness was found to be independent of the initial conditions such as the height of pouring and the volume of poured fluid, as well as the initial thickness profile. Moreover, we found that the shell thickness can be tuned over one order of magnitude by changing the waiting time between the preparation of the polymer solution and the moment of pouring the solution onto the mold. Our analysis demonstrated that the robustness and the flexibility of this mechanism are inherent consequences of the loss of memory in the flow field. Our approach provides a fast, robust and predictable mechanism to fabricate thin shells with flexibility in their material and geometric properties by tuning the control parameters.

In **Chapter 3**, empowered by the experimental technique presented in Chapter 2, we designed experiments to explore the buckling of thin spherical shells, in which we systematically varied the geometry of the imperfection. Specifically, we studied the effect of a single dimple-like defect on the critical buckling load of spherical elastic shells subjected to pressure loading. We recall that imperfection sensitivity to shell buckling is a canonical problem in structural mechanics that has been longstanding for more than 50 years. Our investigation combined precision experiments, finite element modeling, and numerical solutions of a reduced shell theory, all of which were found to be in excellent quantitative agreement, something that, to the best of our knowledge, had not yet been found in the literature. In our experiments, the geometry and magnitude of the defect could be designed and precisely fabricated through a customizable rapid prototyping technique. Our primary focus was on predictively describing the imperfection sensitivity of the thin spherical shell to provide a quantitative relation between its knockdown factor (the ratio between the experimental critical buckling pressure and the corresponding classical theoretical prediction) and the amplitude of the defect. In addition, we found that the buckling pressure becomes independent of the amplitude of the defect beyond a critical value. The level and onset of this plateau were quantified systematically and found to be affected by a single geometric parameter that depends on both the radius-to-thickness ratio of the shell and the angular width of the defect. Overall, our results demonstrated that small deviations from the spherical geometry result in large reductions in the

buckling pressure, in a way that can be accurately predicted by FEM and numerical simulations of a reduced shell theory, as long as the shape of the defect is known.

In **Chapter 4**, we fabricated hemispherical bilayer shells that could exhibit either an increase or a decrease of the critical buckling pressure as a function of time. These bilayer shells were fabricated by coating two different polymer solutions, layer by layer, onto hemispherical molds that contained an engineered defect. Within the bilayer polymer structure, uncross-linked residual chains in one of the layers diffused into the other fully cross-linked layer. This mass diffusion results in a variation of the volume of each layer, *i.e.* it leads to residual swelling. We first experimentally characterized the natural curvature of thin bilayer structure that evolves due to this inhomogeneous swelling. Then, we fabricated bilayer shells and measured their critical buckling pressure over time, finding that it could increase or decrease, depending on the order of coating of the polymer solutions. By investigating the dynamics of deformation of the bilayer shells, we found that the geometric imperfections can be repaired or aggravated due to residual swelling. The experimental results were corroborated by FEM simulations, onto which we imported the experimentally measured shapes of shells.

Shell buckling, in addition to its canonical status in structural mechanics, continues to be an industrially relevant problem. Furthermore, it is also of interest for the life sciences, such as in the contexts of viruses Lidmar et al. (2003), capsules Dinsmore et al. (2002) and pollen grains Katifori et al. (2010). Therefore, buckling of shells is an area of mechanics research that is as relevant as ever, and deserves further attention.

5.2 Outlook and possible directions for future work

We explored the buckling of thin spherical shells with a dimple-like defect and bilayer shells with a flat defect, focusing on the critical buckling pressure. However, many other types of imperfections and loading conditions exist. Beyond localized buckling, a thin shell can respond to mechanical load in other way, such as wrinkling and frac-

ture. For the remainder of this section, we mention a few such examples as potential directions for future work. We hope that our research will instigate a resurgence of interest on the mechanics of thin spherical shells.

Other types of geometric imperfections

Our results will hopefully motivate future explorations on the effect of other types of imperfections on their buckling behavior. Beyond dimple defects, many other geometric imperfections of practical relevance are possible. Some of these variations have already been investigated theoretically and numerically, but much work still needs to be done to contrast these results against experiments. For example, Hutchinson (1967) studied defects in the shape of the critical buckling mode. In addition, Koga & Hoff (1969) numerically analyzed defects that were a spherical region with a different radius of curvature from the remainder of the shell. Moreover, as we presented in Chapter 4, the thickness variation is another type of imperfections that significantly affects the critical buckling pressure, and should certainly be studied in more detail.

Post-buckling behavior

In this thesis, we have focused on the threshold value for the pressure at which a spherical shell buckles. However, post-buckling behavior and the large reconfigurations that it ensues has attained much recent interest for smart applications, as we described in Chapter 1. For example, it has been recently shown that the post-buckling response of cylindrical shells can be controlled by varying its geometry (Hu & Burgueño, 2017). Similarly, spherical shells could also be designed to exhibit tailored post-buckling behavior.

Buckling under dynamic pressure

Buckling of thin shells under dynamics pressure (*e.g.*, impulsive and step pressure) is another classic problem in the mechanics community (Budiansky & Hutchinson, 1966). In this thesis, we have conducted experiments with quasi-static pressure loading. However, many shell structures in nature and engineering applications experience

dynamic loading, for example, the high wind load on radomes (Belles, 2017) and blast waves on the human eye (Bhardwaj et al., 2014). The effect of geometric imperfections on the dynamic buckling of shells could be investigated through model experiments similar to the ones presented in this thesis and, consequently, corroborate existing theoretical and numerical results.

Other types of mechanical problem

Our fabrication technique to produce thin elastic shells could be utilized to study other mechanical problem beyond the buckling under a pressure load. In Chapter 1, we introduced the studies on wrinkling of spherical shells for aerodynamic drag reduction (Terwagne et al., 2014), where the shells were fabricated by coating polymeric liquid onto spherical substrates empirically. Our analytical model and the technique to tune the thickness could serve a useful tool for other future experimental studies using shells. For example, our coating technique was directly used in recent study on surface buckling instabilities (Al-Rashed et al., 2017). In this study, an elastic plate was inflated to form hemispherical surface and then a thin film was coated on top of that hemispherical surface by pouring a polymer solution that eventually cures to form thin elastic structure. Releasing the pre-stretch in the substrate through deflation induced biaxial compression in the outer thin film and yielded various surface buckling patterns.

Furthermore, we suggest research on the fracture of thin spherical shells. There were studies on tearing of thin sheets adhering to a flat surface (Hamm et al., 2008) and curved cylindrical surface (Kruglova et al., 2011). When a flap was detached by tearing and peeling from the cylindrical surface, the two crack tips converged or diverged depending on the sign of the curvature of the cylinder, while the crack tips always collapsed on the flat surface. When the thin sheet was brittle, the fracture path was found to be remarkably reproducible and was able to be predicted by theory (Roman, 2013). The coating process developed in this thesis can be conducted with any viscous liquid that eventually solidifies. Thus, by coating a brittle film on a spherical substrate, the effect of double-curvature on the fracture path could be

investigated.

Bibliography

Adam, H. P., & King, P. A. (1965). Experimental investigation of the stability of monocoque domes subjected to external pressure. *Experimental Mechanics*, *5*(10), 313–320.

Aggarwala, B. D., & Saibel, E. (1970). Thermal stability of bimetallic shallow spherical shells. *International Journal of Non-Linear Mechanics*, *5*(1), 49–62.

Al-Rashed, R., Jiménez, F. L., Marthelot, J., & Reis, P. M. (2017). Buckling patterns in biaxially pre-stretched bilayer shells: wrinkles, creases, folds and fracture-like ridges. *Soft Matter*, *13*, 7969–7978.

Almroth, B. O. (1965). Influence of edge conditions on the stability of axially compressed cylindrical shells. Tech. Rep. NASA-CR-161, Lockheed Missiles and Space Company, Sunnyvale, CA.

Audoly, B., & Pomeau, Y. (2010). *Elasticity and Geometry: From Hair Curls to the Non-Linear Response of Shells*. Oxford University Press.

Augustin, M. A., & Hemar, Y. (2009). Nano-and micro-structured assemblies for encapsulation of food ingredients. *Chemical Society Reviews*, *38*(4), 902–912.

Babcock, C. D. (1983). Shell stability. *Journal of Applied Mechanics*, *50*(4b), 935–940.

Babcock, C. D., & Sechler, E. E. (1963). The effect of initial imperfections on the buckling stress of cylindrical shells. Tech. Rep. NASA-TN-D-2005, California Institute of Technology, Pasadena, CA.

Batista, M., & Kosel, F. (2006). Thermoelastic stability of a double-layered spherical shell. *International Journal of Non-Linear Mechanics*, *41*(9), 1016–1027.

Beall, G. (1998). *Rotational Molding: Design, Materials, Tooling, and Processing*. Hanser Verlag.

Belles, J. (2017). Puerto rico radar obliterated after it takes a direct hit from hurricane maria.
URL `weather.com/news/weather/news/puerto-rico-radar-demolished-hurricane-maria`

Bende, N. P., Evans, A. A., Innes-Gold, S., Marin, L. A., Cohen, I., Hayward, R. C., & Santangelo, C. D. (2015). Geometrically controlled snapping transitions in shells with curved creases. *Proceedings of the National Academy of Sciences*, *112*(36), 11175–11180.

Bhardwaj, R., Ziegler, K., Seo, J. H., Ramesh, K., & Nguyen, T. D. (2014). A computational model of blast loading on the human eye. *Biomechanics and Modeling in Mechanobiology*, *13*(1), 123–140.

Bijlaard, P. P., & Gallagher, R. H. (1959). Elastic instability of a cylindrical shell under arbitrary circumferential variation of axial stresses. *Journal of the Aerospace Sciences*, *27*(11), 854–858.

Bilstein, R. E. (1999). *Stages to Saturn: A Technological History of the Apollo/Saturn Launch Vehicle*. DIANE Publishing.

Błachut, J. (2009). Buckling of multilayered metal domes. *Thin-Walled Structures*, *47*(12), 1429–1438.

Bretherton, F. P. (1961). The motion of long bubbles in tubes. *Journal of Fluid Mechanics*, *10*(2), 166–188.

Brown, E. N., Friehe, C. A., & Lenschow, D. H. (1983). The use of pressure fluctuations on the nose of an aircraft for measuring air motion. *Journal of Climate and Applied Meteorology*, *22*(1), 171–180.

Brown, E. N., Sottos, N. R., & White, S. R. (2002). Fracture testing of a self-healing polymer composite. *Experimental Mechanics*, *42*(4), 372–379.

Brown, E. N., White, S. R., & Sottos, N. R. (2004). Microcapsule induced toughening in a self-healing polymer composite. *Journal of Materials Science*, *39*(5), 1703–1710.

Brown, E. N., White, S. R., & Sottos, N. R. (2005). Retardation and repair of fatigue cracks in a microcapsule toughened epoxy composite—part ii: In situ self-healing. *Composites Science and Technology*, *65*(15), 2474–2480.

Budiansky, B. (1968). Notes on nonlinear shell theory. *Journal of Applied Mechanics*, *35*(2), 393–401.

Budiansky, B., & Hutchinson, J. W. (1966). Dynamic buckling of imperfection-sensitive structures. *Applied Mechanics*, (pp. 636–651).

Budiansky, B., & Hutchinson, J. W. (1972). Buckling of circular cylindrical shells under axial compression. Tech. rep.

Burgoyne, C. F., Downs, J. C., Bellezza, A. J., Suh, J.-K. F., & Hart, R. T. (2005). The optic nerve head as a biomechanical structure: a new paradigm for understanding the role of iop-related stress and strain in the pathophysiology of glaucomatous optic nerve head damage. *Progress in Retinal and Eye Research*, *24*(1), 39–73.

Carlson, R. L., Sendelbeck, R. L., & Hoff, N. J. (1967). Experimental studies of the buckling of complete spherical shells. *Experimental Mechanics*, *7*(7), 281–288.

Chen, W. L. (1959). *Effect of Geometrical Imperfection on the Elastic Buckling of Thin Shallow Spherical Shells*. Ph.D. thesis, Massachusetts Institute of Technology.

Chen, X., Dam, M. A., Ono, K., Mal, A., Shen, H., Nutt, S. R., Sheran, K., & Wudl, F. (2002). A thermally re-mendable cross-linked polymeric material. *Science*, *295*(5560), 1698–1702.

Chen, X., Wudl, F., Mal, A. K., Shen, H., & Nutt, S. R. (2003). New thermally remendable highly cross-linked polymeric materials. *Macromolecules*, *36*(6), 1802–1807.

Cordier, P., Tournilhac, F., Soulié-Ziakovic, C., & Leibler, L. (2008). Self-healing and thermoreversible rubber from supramolecular assembly. *Nature*, *451*(7181), 977–980.

Couder, Y., Fort, E., Gautier, C.-H., & Boudaoud, A. (2005). From bouncing to floating: noncoalescence of drops on a fluid bath. *Physical Review Letters*, *94*(17), 177801.

Crawford, R. J. (2012). *Practical Guide to Rotational Moulding*. Smithers Rapra.

Datta, S. S., Abbaspourrad, A., Amstad, E., Fan, J., Kim, S.-H., Romanowsky, M., Shum, H. C., Sun, B., Utada, A. S., Windbergs, M., et al. (2014). 25th anniversary article: double emulsion templated solid microcapsules: mechanics and controlled release. *Advanced Materials*, *26*(14), 2205–2218.

Datta, S. S., Kim, S.-H., Paulose, J., Abbaspourrad, A., Nelson, D. R., & Weitz, D. A. (2012). Delayed buckling and guided folding of inhomogeneous capsules. *Physical Review Letters*, *109*(13), 134302.

Dinsmore, A. D., Hsu, M. F., Nikolaides, M. G., Marquez, M., Bausch, A. R., & Weitz, D. A. (2002). Colloidosomes: selectively permeable capsules composed of colloidal particles. *Science*, *298*(5595), 1006–1009.

Dong, X. L., Gao, Z. Y., & Yu, T. X. (2008). Dynamic crushing of thin-walled spheres: An experimental study. *International Journal of Impact Engineering*, *35*(8), 717–726.

Elishakoff, I. (2014). *Resolution of the Twentieth Century Conundrum in Elastic Stability*. World Scientific.

Emslie, A. G., Bonner, F. T., & Peck, L. G. (1958). Flow of a viscous liquid on a rotating disk. *Journal of Applied Physics*, *29*(5), 858–862.

Fitch, J. M., & Branch, D. P. (1960). Primitive architecture and climate. *Scientific American*, *203*(6), 134–144.

Frisch, H. L. (1957). The time lag in diffusion. *The Journal of Physical Chemistry*, *61*(1), 93–95.

Godoy, L. A. (2016). Buckling of vertical oil storage steel tanks: Review of static buckling studies. *Thin-Walled Structures*, *103*, 1–21.

Hamm, E., Reis, P., LeBlanc, M., Roman, B., & Cerda, E. (2008). Tearing as a test for mechanical characterization of thin adhesive films. *Nature Materials*, *7*(5), 386–390.

Hilburger, M. W. (2012). Developing the next generation shell buckling design factors and technologies. In *53rd AIAA/ASME/ASCE/AHS/ASC Structures, Structural Dynamics and Materials Conference*, AIAA 2012-1686.

Hilburger, M. W., Nemeth, M. P., & Starnes, J. H. (2006). Shell buckling design criteria based on manufacturing imperfection signatures. *AIAA Journal*, *44*(3), 654–663.

Homewood, R. H., Brine, A. C., & Johnson, A. E. (1961). Experimental investigation of the buckling instability of monocoque shells. *Experimental Mechanics*, *1*(3), 88–96.

Hu, D. L., Sielert, K., & Gordon, M. (2012). Turtle shell and mammal skull resistance to fracture due to predator bites and ground impact. *Journal of Mechanics of Materials and Structures*, *6*(9), 1197–1211.

Hu, N., & Burgueño, R. (2017). Harnessing seeded geometric imperfection to design cylindrical shells with tunable elastic postbuckling behavior. *Journal of Applied Mechanics*, *84*(1), 011003.

Hutchinson, J. W. (1967). Imperfection sensitivity of externally pressurized spherical shells. *Journal of Applied Mechanics*, *34*(1), 49–55.

Hutchinson, J. W. (2016). Buckling of spherical shells revisited. *Proceedings of the Royal Society A*, *472*(2195), 20160577.

Hutchinson, J. W., & Koiter, W. T. (1970). Postbuckling theory. *Applied Mechanics Reviews*, *23*(12), 1353–1366.

Ibarz, G., Dähne, L., Donath, E., & Moehwald, H. (2001). Smart micro-and nanocontainers for storage, transport, and release. *Advanced Materials*, *13*(17), 1324–1327.

IMSL (1994). Math/library: Fortran subroutines for mathematical applications. *Visual Numerics*.

Kalpakjian, S., & Schmid, S. R. (2014). *Manufacturing Engineering and Technology*. NJ, USA: Pearson Upper Saddle River.

Kaplan, A., & Fung, Y. C. (1954). A nonlinear theory of bending and buckling of thin elastic shallow spherical shells. Tech. Rep. NACA-TN-3212, California Institute of Technology, Pasadena, CA.

Karnik, R., Gu, F., Basto, P., Cannizzaro, C., Dean, L., Kyei-Manu, W., Langer, R., & Farokhzad, O. C. (2008). Microfluidic platform for controlled synthesis of polymeric nanoparticles. *Nano Letters*, *8*(9), 2906–2912.

Katifori, E., Alben, S., Cerda, E., Nelson, D. R., & Dumais, J. (2010). Foldable structures and the natural design of pollen grains. *Proceedings of the National Academy of Sciences*, *107*(17), 7635–7639.

Kobayashi, S. (1968). The influence of the boundary conditions on the buckling load of cylindrical shells under axial compression (boundary condition influence on buckling load of cylindrical shell under axial compression). *Journal of the Japan Society for Aeronautical and Space Sciences*, *16*, 74–82.

Koga, T., & Hoff, N. J. (1969). The axisymmetric buckling of initially imperfect complete spherical shells. *International Journal of Solids and Structures*, *5*(7), 679–697.

Koiter, W. T. (1945). *Over de Stabiliteit van het Elastisch Evenwicht*. Ph.D. thesis, De Technische Hogeschool te Delft.

Koiter, W. T. (1966). On the nonlinear theory of thin elastic shells. i- introductory sections. ii- basic shell equations. iii- simplified shell equations (nonlinear theory of thin elastic shells, discussing surface geometry and deformation, equations of equilibrium and boundary conditions and stress functions). *Koninklijke Nederlandse Akademie van Wetenschappen, Proceedings, Series B*, *69*(1), 1–54.

Koiter, W. T. (1967). General equations of elastic stability for thin shells. In *Proceedings of the Symposium on the Theory of Shells to Honor Lloyd Hamilton Donnell*, (pp. 187–228).

Krenzke, M. A., & Kiernan, T. J. (1963). Elastic stability of near-perfect shallow spherical shells. *AIAA Journal*, *1*(12), 2855–2857.

Kruglova, O., Brau, F., Villers, D., & Damman, P. (2011). How geometry controls the tearing of adhesive thin films on curved surfaces. *Physical Review Letters*, *107*(16), 164303.

Landau, L. D., & Levich, B. G. (1942). Dragging of a liquid by a moving plate. *Acta Physicochimica URSS*, *17*, 42–54.

Lazarus, A., Florijn, H. C. B., & Reis, P. M. (2012). Geometry-induced rigidity in nonspherical pressurized elastic shells. *Physical Review Letters*, *109*(14), 144301.

Leal, L. G. (2007). *Advanced Transport Phenomena: Fluid Mechanics and Convective Transport Processes*. Cambridge University Press.

Lee, A., Brun, P.-T., Marthelot, J., Balestra, G., Gallaire, F., & Reis, P. (2016a). Fabrication of slender elastic shells by the coating of curved surfaces. *Nature Communications*, *7*, 11155.

Lee, A., López Jiménez, F., Marthelot, J., Hutchinson, J. W., & Reis, P. M. (2016b). The geometric role of precisely engineered imperfections on the critical buckling load of spherical elastic shells. *Journal of Applied Mechanics*, *83*(11), 111005.

Lee, N. C. (2006). *Practical Guide to Blow Moulding*. iSmithers Rapra Publishing.

Lhuissier, H., & Villermaux, E. (2012). Bursting bubble aerosols. *Journal of Fluid Mechanics*, *696*, 5–44.

Lidmar, J., Mirny, L., & Nelson, D. R. (2003). Virus shapes and buckling transitions in spherical shells. *Physical Review E*, *68*(5), 051910.

López Jiménez, F., Marthelot, J., Lee, A., Hutchinson, J. W., & Reis, P. M. (2017). Technical brief: Knockdown factor for the buckling of spherical shells containing large-amplitude geometric defects. *Journal of Applied Mechanics*, *84*(3), 034501.

Maistone, R. J. (1988). *Hagia Sophia: Architecture Structure and Liturgy of Justinian's Great Church*. London: Thames and Hudson.

Mallick, P. K. (2007). *Fiber-Reinforced Composites: Materials, Manufacturing, and Design*. CRC Press.

Meyer, R. R., & Bellingante, R. J. (1964). Fabrication and experimental evaluation of common domes having waffle-like stiffening. Tech. Rep. Douglas Report SM-47742, Missile & Space Systems Division Douglas Aircraft Company, Inc., Santa Monica, CA.

Meyerhofer, D. (1978). Characteristics of resist films produced by spinning. *Journal of Applied Physics*, *49*(7), 3993–3997.

Myers, K. M., Cone, F. E., Quigley, H. A., Gelman, S., Pease, M. E., & Nguyen, T. D. (2010). The in vitro inflation response of mouse sclera. *Experimental Eye Research*, *91*(6), 866–875.

Nash, W. A. (1995). *Hydrostatically Loaded Structures: The Structural Mechanics, Analysis and Design of Powered Submersibles*. Elsevier.

Nasto, A., Ajdari, A., Lazarus, A., Vaziri, A., & Reis, P. M. (2013). Localization of deformation in thin shells under indentation. *Soft Matter*, *9*(29), 6796–6803.

Nasto, A., & Reis, P. M. (2014). Localized structures in indented shells: A numerical investigation. *Journal of Applied Mechanics*, *81*(12), 121008.

Ning, X., & Pellegrino, S. (2017). Experiments on imperfection insensitive axially loaded cylindrical shells. *International Journal of Solids and Structures*, *115*, 73–86.

Noor, A. K., Burton, W. S., & Bert, C. W. (1996). Computational models for sandwich panels and shells. *Applied Mechanics Reviews*, *49*, 155–155.

Panov, D. V. (1947). On the stability of a bimetallic membrane on heating. *Prikladnaja Matematika i Mehanika (Jounal of Applied Mathematics and Mechanics)*, *11*(6), 603–610.

Pedersen, P. T., & Jensen, J. J. (1995). Buckling behaviour of imperfect spherical shells subjected to different load conditions. *Thin-Walled Structures*, *23*(1-4), 41–55.

Pezzulla, M., Shillig, S. A., Nardinocchi, P., & Holmes, D. P. (2015). Morphing of geometric composites via residual swelling. *Soft Matter*, *11*(29), 5812–5820.

Pezzulla, M., Smith, G. P., Nardinocchi, P., & Holmes, D. P. (2016). Geometry and mechanics of thin growing bilayers. *Soft Matter*, *12*(19), 4435–4442.

Pezzulla, M., Stoop, N., Steranka, M. P., Bade, A. J., & Holmes, D. P. (2017). Curvature-induced instabilities of shells. *arXiv preprint arXiv:1706.03888*.

Pozrikidis, C. (1988). The flow of a liquid film along a periodic wall. *Journal of Fluid Mechanics*, *188*, 275–300.

Qatu, M. S. (2004). *Vibration of laminated shells and plates*. Elsevier.

Rai-Choudhury, P. (1997). *Handbook of Microlithography, Micromachining, and Microfabrication: Microlithography*. IET.

Rees, H., & Catoen, B. (2006). *Selecting Injection Molds*. Hanser Gardner Publications.

Reis, P. M. (2015). A perspective on the revival of structural (in)stability with novel opportunities for function: From buckliphobia to buckliphilia. *Journal of Applied Mechanics*, *82*(11), 111001.

Reis, P. M., Jaeger, H. M., & van Hecke, M. (2015). Designer matter: A perspective. *Extreme Mechanics Letters*, *5*, 25–29.

Ren-Huai, L. (1983). Non-linear thermal stability of bimetallic shallow shells of revolution. *International Journal of Non-Linear Mechanics*, *18*(5), 409–429.

Riks, E. (1979). An incremental approach to the solution of snapping and buckling problems. *International Journal of Solids and Structures*, *15*(7), 529–551.

Roman, B. (2013). Fracture path in brittle thin sheets: A unifying review on tearing. *International Journal of Fracture*, *182*(2), 209–237.

Rutgerson, S. E., & Bottega, W. J. (2002). Thermo-elastic buckling of layered shell segments. *International Journal of Solids and Structures*, *39*(19), 4867–4887.

Sagis, L. M. C., de Ruiter, R., Miranda, F. J. R., de Ruiter, J., Schroën, K., van Aelst, A. C., Kieft, H., Boom, R., & van der Linden, E. (2008). Polymer microcapsules with a fiber-reinforced nanocomposite shell. *Langmuir*, *24*(5), 1608–1612.

Samuelson, L. A., & Eggwertz, S. F. (2003). *Shell Stability Handbook*. CRC Press.

Sanders Jr., J. L. (1963). Nonlinear theories for thin shells. *Quarterly of Applied Mathematics*, *21*(1), 21–36.

Scriven, L. E. (1988). Physics and applications of dip coating and spin coating. *MRS Online Proceedings Library Archive*, *121*.

Seaman, L. (1962). *The Nature of Buckling in Thin Spherical Shells*. Ph.D. thesis, Massachusetts Institute of Technology.

Song, P. S., & Hwang, S. (2004). Mechanical properties of high-strength steel fiber-reinforced concrete. *Construction and Building Materials*, *18*(9), 669–673.

Spiers, R. P., Subbaraman, C. V., & Wilkinson, W. L. (1974). Free coating of a newtonian liquid onto a vertical surface. *Chemical Engineering Science*, *29*(2), 389–396.

Stoddard, M. C., Yong, E. H., Akkaynak, D., Sheard, C., Tobias, J. A., & Mahadevan, L. (2017). Avian egg shape: Form, function, and evolution. *Science*, *356*(6344), 1249–1254.

Stoop, N., Lagrange, R., Terwagne, D., Reis, P. M., & Dunkel, J. (2015). Curvature-induced symmetry breaking determines elastic surface patterns. *Nature Materials*, *14*(3), 337–342.

Takagi, D., & Huppert, H. E. (2010). Flow and instability of thin films on a cylinder and sphere. *Journal of Fluid Mechanics*, *647*, 221–238.

Tennyson, R. C. (1963). A note on the classical buckling load of circular cylindrical shells under axial compression. *AIAA Journal*, *1*(2), 475–476.

Tennyson, R. C. (1964). An experimental investigation of the buckling of circular cylindrical shells in axial compression using the photoelastic technique. Tech. rep., University of Toronto.

Tennyson, R. C. (1968). The effects of unreinforced circular cutouts on the buckling of circular cylindrical shells under axial compression. *Journal of Engineering for Industry*, *90*(4), 541–546.

Tennyson, R. C., & Welles, S. W. (1968). Analysis of the buckling process of circular cylindrical shells under axial compression. Tech. rep., University of Toronto.

Terwagne, D., Brojan, M., & Reis, P. M. (2014). Smart morphable surfaces for aerodynamic drag control. *Advanced Materials*, *26*(38), 6608–6611.

Thielicke, W., & Stamhuis, E. (2014). Pivlab–towards user-friendly, affordable and accurate digital particle image velocimetry in matlab. *Journal of Open Research Software*, *2*(e30), 1–10.

Thompson, J. M. T. (1960). Making of thin metal shells for model stress analysis. *Journal of Mechanical Engineering Science*, *2*(2), 105–108.

Thompson, J. M. T. (1962). The elastic instability of a complete spherical shell. *The Aeronautical Quarterly*, *13*(2), 189–201.

Timoshenko, S. P. (1925). Analysis of bi-metal thermostats. *Journal of the Optical Society of America*, *11*(3), 233–255.

Timoshenko, S. P., & Gere, J. M. (1961). *Theory of Elastic Stability*. McGraw-Hill.

Trinh, P. H., Kim, H., Hammoud, N., Howell, P. D., Chapman, S. J., & Stone, H. A. (2014). Curvature suppresses the rayleigh-taylor instability. *Physics of Fluids*, *26*(5), 051704.

Tsien, H.-S. (1942). A theory for the buckling of thin shells. *Journal of the Aeronautical Sciences*, *9*(10), 373–384.

Tsuji, K. (2001). Microencapsulation of pesticides and their improved handling safety. *Journal of Microencapsulation*, *18*(2), 137–147.

Vaziri, A., & Mahadevan, L. (2008). Localized and extended deformations of elastic shells. *Proceedings of the National Academy of Sciences*, *105*(23), 7913–7918.

Vella, D., Huang, J., Menon, N., Russell, T. P., & Davidovitch, B. (2015). Indentation of ultrathin elastic films and the emergence of asymptotic isometry. *Physical Review Letters*, *114*(1), 014301.

Ventsel, E., & Krauthammer, T. (2001). *Thin Plates and Shells: Theory, Analysis, and Applications*. CRC Press.

Virot, E., Kreilos, T., Schneider, T. M., & Rubinstein, S. M. (2017). Stability landscape of shell buckling. *Physical Review Letters*, *119*, 224101.

Vlachogiannis, M., & Bontozoglou, V. (2002). Experiments on laminar film flow along a periodic wall. *Journal of Fluid Mechanics*, *457*, 133–156.

von Kármán, T. (1939). The buckling of spherical shells by external pressure. *Journal of the Aeronautical Sciences*, *7*(2), 43–50.

von Kármán, T., Dunn, L. G., & Tsien, H.-S. (1940). The influence of curvature on the buckling characteristics of structures. *Journal of the Aeronautical Sciences*, *7*(7), 276–289.

von Kármán, T., & Tsien, H.-S. (1941). The buckling of thin cylindrical shells under axial compression. *Journal of Aeronautical Sciences*, *8*(8), 303–312.

Weinstein, S. J., & Ruschak, K. J. (2004). Coating flows. *Annual Review of Fluid Mechanics*, *36*, 29–53.

White, S. R., Sottos, N. R., Geubelle, P. H., Moore, J. S., Kessler, M. R., Sriram, S. R., Brown, E. N., & Viswanathan, S. (2001). Autonomic healing of polymer composites. *Nature*, *409*, 794–797.

Wittrick, W. H., Myers, D. M., & Blunden, W. R. (1953). Stability of a bimetallic disk. *The Quarterly Journal of Mechanics and Applied Mathematics*, *6*(1), 15–31.

Wu, H., Huang, B., & Zare, R. N. (2005). Construction of microfluidic chips using polydimethylsiloxane for adhesive bonding. *Lab on a Chip*, *5*(12), 1393–1398.

Zoelly, R. (1915). *Ueber ein Knickungsproblem an der Kugelschale*. Ph.D. thesis, ETH Zürich.